Quantum Remote Sensing and Non-Equilibrium Phase Transitions in the Microwave Regime

by

Riya Sett

April, 2025

A thesis submitted to the
Graduate School
of the
Institute of Science and Technology Austria
in partial fulfillment of the requirements
for the degree of
Doctor of Philosophy

Committee in charge:
Julian Fischer, Chair
Johannes Fink
Georgios Katsaros
Peter Rabl



	Sett, titled <i>Quantum Remote Sensing and Non-Equilibrium Phase Transitions</i> e <i>Regime</i> , is approved by:
Supervisor : Joh	annes Fink, ISTA, Klosterneuburg, Austria
	Signature:
Committee Me	mber: Georgios Katsaros, ISTA, Klosterneuburg, Austria
	Signature:
Committee Me	mber: Peter Rabl, TU Munich, Munich, Germany
	Signature:
Defense Chair:	Julian Fischer, ISTA, Klosterneuburg, Austria
	Signature:

© by Riya Sett, April, 2025

CC BY 4.0 The copyright of this thesis rests with the author. Unless otherwise indicated, its contents are licensed under a Creative Commons Attribution 4.0 International License. Under this license, you may copy and redistribute the material in any medium or format. You may also create and distribute modified versions of the work. This is on the condition that: you credit the author.

ISTA Thesis, ISSN: 2663-337X

I hereby declare that this thesis is my own work and that it does not contain other people's work without this being so stated; this thesis does not contain my previous work without this being stated, and the bibliography contains all the literature that I used in writing the dissertation.

I accept full responsibility for the content and factual accuracy of this work, including the data and their analysis and presentation, and the text and citation of other work.

I declare that this is a true copy of my thesis, including any final revisions, as approved by my thesis committee, and that this thesis has not been submitted for a higher degree to any other university or institution.

I certify that any republication of materials presented in this thesis has been approved by the relevant publishers and co-authors.

Signature: _____

Riya Sett April, 2025

Abstract

This thesis explores advancements in quantum remote sensing and non-equilibrium phase transitions in the microwave regime, with a focus on dissipative phase transitions and quantum-enhanced sensing.

In the first project, I experimentally studied photon blockade breakdown as a dissipative phase transition in a zero-dimensional cavity-qubit system. By defining an appropriate thermodynamic limit, we demonstrated that the observed bistability is a genuine signature of a first-order phase transition in this system. This work provides insight into non-equilibrium quantum dynamics and phase transitions in driven-dissipative open quantum systems.

The second project focuses on the experimental realization of a phase-conjugate receiver for quantum illumination (QI), a quantum sensing protocol that enhances target detection in noisy environments using entangled light. While an ideal spontaneous parametric down-conversion (SPDC) source and receiver could, in theory, provide up to a 6 dB advantage over classical illumination, no such ideal receiver exists. Instead, we explore an experimental realization of a phase-conjugate receiver for QI in the microwave regime at millikelvin temperatures using a Josephson parametric converter (JPC) as a source of continuous-variable Gaussian entangled signal-idler pairs, where a maximum 3 dB advantage is theoretically achievable. We investigate key experimental limitations that constrain practical QI performance, contributing to the development of quantum-enhanced sensing.

Additionally, this thesis presents efficient digital signal processing (DSP) techniques implemented in C++ and Python in collaboration with Przemysław Zieliński and Luka Drmić. These methods, optimized using the Intel Integrated Performance Primitives (IPP) library, have been essential in data acquisition, noise filtering, and correlation analysis across multiple research projects. Although not real-time, these DSP techniques significantly enhance the accuracy of quantum measurements.

Overall, this thesis advances quantum-enhanced sensing by establishing the thermodynamic limit in a single transmon-cavity system and experimentally exploring a phase-conjugate receiver for QI. These findings contribute to quantum metrology, particularly for weak signal detection and remote sensing in noisy environments.

Acknowledgements

First and foremost, I dedicate this thesis to my beloved parents as well as Monu, Babli Masi, Mesho and Mamu, whose unwavering love, sacrifices, and encouragement have been the foundation of my journey. Their belief in me, even during the most challenging times, has been my greatest source of strength. Without their support, I would not have reached this milestone.

I extend my deepest gratitude to my supervisor, Johannes, for his trust in me and invaluable guidance. One of the most important lessons I learned from him is that progress becomes easier when tasks are broken down into small, manageable steps. While this principle helped me in conducting experiments, it has also shaped my approach to problem-solving in all aspects of life. His wisdom and mentorship have been instrumental in both my academic and personal growth.

I am profoundly grateful to Georgios for his mentorship and constant encouragement. His belief that failure is not an endpoint but a learning opportunity has always been a guiding principle throughout my journey.

A heartfelt thank you to my colleagues, who have also become dear friends, for their camaraderie, collaboration, and support. The stimulating discussions and shared experiences have made this journey truly enriching and memorable. A special thanks to Andrea, the first to welcome me into the Fink group. Over the past 6.5 years, we have shared countless moments—laughing, supporting each other, and learning resilience together. He remains one of my most trusted friends. I also cherish the deep conversations over coffee and pub gatherings with Liu, where we discussed science, life, and future aspirations—moments that made this journey even more meaningful. I am deeply grateful to Shabir, my first mentor, whose guidance during my rotation laid the foundation for my scientific growth and continues to inspire me. Beyond academics, I have shared unforgettable moments with William, Farid, Shiva, Luka, Janos and Alfredo, especially through our endless ping-pong matches, which brought energy, laughter, and lasting memories. A special mention to Lena and Matilda, two of the strongest women I have ever met. Their resilience, wisdom, and determination have been truly inspiring, and I am grateful for the invaluable lessons I have learned from them.

Apart from my colleagues, I am deeply grateful to my little family in Vienna—Divya, Amrita di, Rev, Raunak, Abhishek, Shraddha, Rishik, Sumanta da, Prajakta, KJ, Dravid, Roshan, Keerthi, Gayathri, Mukund, Kuldeep, Priya, Suresh, Suma, Kalyan, and Melanie—for their unwavering support and for always being there for me. To my friends in India—Ujan, Madhu, Diptam, Gargi, Sayan, Shourja, and Arijit—thank you for never failing to make me laugh, no matter the circumstances. I am especially grateful to my Paris family—Saheli, Rajesh da, Sonima boudi, Pabitra da, Debasmita boudi, and Chitram da—whose love, encouragement, and constant presence have been a true source of strength throughout my PhD journey.

I acknowledge the generous financial support of the Austrian Science Fund (FWF) via BeyondC (F7105) and the European Union's Horizon 2020 research and innovation program (FETopen QUARTET, Grant Agreement No. 862644), which made this research possible. I also extend my sincere appreciation to the MIBA workshop and the Institute of Science and Technology Austria nanofabrication facility for their technical assistance, which was instrumental in realizing this work.

About the Author

Riya holds a Bachelor of Technology (B.Tech) degree in Electronics and Communications Engineering from the Institute of Engineering and Management, affiliated with West Bengal University of Technology (2016). During this time, she worked on a portable navigation device designed to assist visually impaired individuals in both indoor and outdoor environments. In 2018, she earned an MSc in Physics with a specialization in Photonics and Quantum Optics from Aix-Marseille University, France, and Universitat Politècnica de Catalunya, Spain. As a Scientific Assistant at the Karlsruhe Institute of Technology, she contributed to a project on the 'Flip-chip' approach for stacking superconducting circuits in three dimensions. For her Master's thesis, she fabricated and characterized a quantum-limited Josephson parametric amplifier (JPA) incorporating an array of SQUIDs as the nonlinear element. Riya joined ISTA as a PhD student in October 2018. Her research focuses on microwave quantum optics using superconducting circuits.

List of Collaborators and Publications

Elena S. Redchenko, Alexander V. Poshakinskiy, Riya Sett, Martin Žemlička, Alexander N. Poddubny, and Johannes M. Fink. Tunable directional photon scattering from a pair of superconducting qubits. *Nature Communications*, 14(1):2998, May 2023

The following publication is in parts used in **Chapter 3 of the thesis**-

Riya Sett, Farid Hassani, Duc Phan, Shabir Barzanjeh, Andras Vukics, and Johannes M. Fink. Emergent macroscopic bistability induced by a single superconducting qubit. *PRX Quantum*, 5:010327, Feb 2024

E. S. Redchenko, M. Zens, M. Žemlička, M. Peruzzo, F. Hassani, R. Sett, P. Zieliński, H. S. Dhar, D. O. Krimer, S. Rotter, and J. M. Fink. Observation of collapse and revival in a superconducting atomic frequency comb. *Phys. Rev. Lett.*, 134:063601, Feb 2025

Table of Contents

AŁ	strac	t :	vii
Ac	know	ledgements	viii
ΑŁ	out 1	the Author	x
Lis	st of	Collaborators and Publications	хi
Ta	ble o	f Contents	xiii
Lis	st of	Figures	xiv
1	1.1 1.2	Description Background and Motivation	1 1 2
2	Qua 2.1 2.2 2.3 2.4	Introduction	5 6 9 23
3	Pho 3.1 3.2 3.3 3.4 3.5 3.6 3.7	Introduction	27 28 29 32 35 38 40
4	-	ntum Illumination Background State of the art of QI experiments Numerical model of QI with ideal PC receiver Numerical model of experimental PC receiver The QI Experiment Conclusions and outlook	43 44 46 50 56
Bi	bliog	raphy	69

	A.1 The Digitizer Hardware A.2 Data Acquisition with Digitizer A.3 Programming in C++ for data acquisition A.4 The necessary C++ files A.5 Create new signal processing technique using the functions defined in CATS-driver.cpp.	81 81 82 83 89
	A.6 Linking $C++$ and python	91
В	Numerical model of Jaynes-cummings model B.1 The full quantum model	93 93 95
C	QI numerical derivations	99
	C.1 hypothesis H_1 with anihiliation operator	99 104
	List of Figur	es
2.1		es
2.1	Field quadrature extraction with (a) homodyne and (b) heterodyne detection methods. [Rad84] (c) Schematics of importance of IF selection in the frequency domain. In the left schematic, if the IF is too small compared to the signal bandwidth B, part of the signal overlaps with its image frequency after down-conversion, causing interference. However, with a properly chosen IF (right schematic), this image interference can be effectively avoided, ensuring a cleaner signal. Frequency response of (a) 4-point boxcar window filter of cut-off frequency 25 MHz and (b) 7-point Dolph-Chebyshev window filter of cut-off frequency 26 MHz (blue solid line). The effective filter after combining both the filters is shown in	8
	Field quadrature extraction with (a) homodyne and (b) heterodyne detection methods. [Rad84] (c) Schematics of importance of IF selection in the frequency domain. In the left schematic, if the IF is too small compared to the signal bandwidth B, part of the signal overlaps with its image frequency after down-conversion, causing interference. However, with a properly chosen IF (right schematic), this image interference can be effectively avoided, ensuring a cleaner signal. Frequency response of (a) 4-point boxcar window filter of cut-off frequency 25 MHz and (b) 7-point Dolph-Chebyshev window filter of cut-off frequency 26 MHz (blue solid line). The effective filter after combining both the filters is shown in dashed orange line.	

21

2.6	(a) and (b) show the noise spectral density in the unit of quanta as function of temperature. From fitting them with Eq.(4.57) we obtain the effective gains and total noise added referenced at the temperature calibration tool respectively in two output detection chains	21
2.7	The difference between quadrature histograms with the JPC pump on and off for various quadrature pairs	22
3.1	Measurement setup. Schematic of the wiring of the sample inside a Bluefors dilution refrigerator used for the experiment	30
3.2	Experimental realization. (a) Schematics of the experimental device consisting of a superconducting transmon qubit fabricated on a silicon substrate that is placed at the antinode of the fundamental mode of a 3D copper cavity. The cavity has a fixed-length port (red) and an <i>in situ</i> variable-length pin coupler port (blue). (b) Measured cavity transmission spectra with the qubit far detuned for different coupler positions (color coded) together with a fit to Eq. (3.5) (dashed lines) and the extracted $\kappa/2\pi$	31
3.3	Photon blockade breakdown measurements at $g/\kappa \approx 39.1$. (a) The Jaynes-Cummings ladder for a three-level atom illustrating the PBB effect in the frequency domain: single-photon (blue) and multi-photon transitions (red) are indicated according to the measured spectrum at the Rabi-splitting frequencies and near resonance, respectively. As indicated, the third atomic state causes a third subladder in the spectrum starting from the second rung, whose spacing is close to the bare-system frequency. This is a possible explanation for the PBB bistability persisting in the case of resonant driving. (b) Measured cavity transmission spectra for $\omega_{\rm A}=\omega_{\rm R}$ for two applied external drive strengths: $1.05{\rm MHz}$, revealing a typical vacuum Rabi spectrum, and $167.01{\rm MHz}$, where a sharp peak at $\omega_{\rm R}$ is observed. (c) Measured cavity output bistability at $\omega=\omega_{\rm R}$ in the time domain indicating the dwell times of the bright state $(t_{\rm on})$ and the dim state $(t_{\rm off})$. (d)-(f) Measured quadrature histograms (proportional to cavity Q functions convolved with amplifier noise) for the dim phase at $\eta/2\pi=105{\rm MHz}$, for the bistable region with equal probability at $167{\rm MHz}$, and for the bright phase at $210{\rm MHz}$, respectively. (g) Measured histograms of the output power (arranged vertically and with probability color coded) as a function of input power. The maxima indicated by circles trace out a typical bistability curve, see Fig. 3.5(b). (h) Extracted average dwell times in the dim and bright states (Eq. (3.6)) as a function of η . The error bars represent the standard error that is extracted from five sections of the full dataset. The dwell time and drive strength corresponding to half-filling where $t_{\rm dwell}^{\rm dim}=t_{\rm dwell}^{\rm dwell}$ are indicated with an asterisk. The inset shows the measured slow-switching eigenvalue $1/\tau$, from Eq. (3.7), in the unit of κ as a function of drive amplitude η close to half-filling [SC88]	33

3.4	Finite size scaling towards the thermodynamic limit. (a) Measured dwell times in the dim state (blue) and the bright state (red) are shown as a function of η/g for different values of κ . Black stars denote half-filling values, where the probabilities of being in the dim state or bright state are equal. The dashed line is a power law fit. The error bars represent the standard error that is extracted from at least three sections of the full dataset. (b)-(d) Measured scaling laws as a function of control parameter g/κ at half filling (asterisks). Fitting the experimental data (dashed lines) yields the exponents $t_{\rm dwell}^* \propto (g/\kappa)^{5.4\pm0.2}$ for the dwell time, $\langle n \rangle^* \propto (g/\kappa)^{0.96\pm0.05}$ for the average resonator photon number, and $\eta^*/g \propto (g/\kappa)^{-0.52\pm0.03}$ for the input drive strength. We compare the experimental values (stars) with those obtained from QJMC simulations (polygons with color code) for computationally manageable $\kappa=11.5,\ 14.3,\ $ and 18.1 MHz. The simulations include three, five, or seven transmon levels both without transmon dephasing (light blue) and with dephasing increasing linearly with the level number (light red) with $\gamma_{\phi,1}/(2\pi)=50{\rm kHz}$ and $\gamma_1=0$. Details of the simulation are	
	given in the main text and in Appendix B.1	36
3.5	The photon blockade breakdown phase diagram. (a) Phase diagram on the $\Delta-\eta$ plane obtained from the neoclassical theory for two transmon levels. (b) Typical multistability curves for the transmitted intensity as a function of the drive amplitude obtained from the approximate three-level neoclassical theory detailed in Appendix B.2. The curves are different for $\Delta=5\mathrm{MHz}$ and $\Delta=-5\mathrm{MHz}$ proving the asymmetry of the phase boundaries. For $\Delta=0$, the curve obtained from the two-level theory is plotted as a dotted line for comparison, revealing the role of the third level in the appearance of a bistability on resonance. The solution of the three-level theory contains very high order polynomials that lead to numerical problems when the experimental parameters are used. Therefore, here and in (a), model parameters were used: $g_1/\kappa=30$, $g_2/\kappa=2.5$, $\Delta_{\mathrm{an}}/\kappa=-40$ (see Appendix B.1 for the definition of all the parameters of the full model). (c) Experimental PBB phase diagram at $g/\kappa\approx 132$ with boundaries (points) and the half-filling drive strength (dotted line) obtained from the experimental trajectories that exhibit the temporal bistable signal [(e)-(h)]. The color scale of the density plot depicts the ratio $r=(h_1-h_2)/(h_1+h_2)$, where h_1 and h_2 are the amplitudes of the peaks of the measured quadrature histograms corresponding to the dim and bright states, respectively, see Fig. 3.3(d-f). (d) Measured dwell times at half-filling as a function of drive detuning. Error bars are extracted from the mean and standard error of the measured dim and bright dwell times. (e)-(h) Experimentally observed telegraph signals that define the phase boundaries at different η values at $\Delta=0$ in the range of $\eta/2\pi$ from 85.6 to 115.5 MHz as indicated by a double arrow in (c).	39
4.1 4.2 4.3	Lloyd's idea [Llo08] of detecting a weakly reflecting target in presence of background noise with (a) coherent state light and (b) entangled lights	44 46
1 1	reflectivity of the target	50 51

4.5	of signal photon number for $N_B=100$, $\eta=0.1$, $G_X=90$ dB, $G_Y=100$ dB, $n_{\rm add}^X=10$, $n_{\rm add}^Y=14$. (b) same as function of background noise at $N_S=0.3$. (c)-(d) same as (a)-(b) with calibrated gain and added noise in the output detection chain.	54
4.6	SNR comparisons between QI, CS Homodyne and CS Heterodyne (a) as function of gain $G_X=G_Y=G_S$ of the detection chain; (b) beam-splitter amplitude splitting ratio t ; (c) the phase-conjugator gain G_{PC} and (d) loss in idler path κ . In all these four cases, $N_S=0.1$, $N_B=24$, and $\eta=-5$ dB	55
4.7	Schematic of the experimental setup of QI inside dilution refrigerator with base temperature at around 15mK. The JPCs were donated by IBM. \dots	57
4.8	(a) The top section shows the measured covariance matrix elements as function of LO frequency detuning at pump power -1 dBm. The middle section shows how minimum Duan value Δ^- and the bottom section shows maximum Duan value Δ^+ as function of LO detuning. At detuning 0 MHz, the entanglement is the maximum observed from both squeezing (Δ^-) and anti-squeezing (Δ^+) as expected. The black dashed lines show the fits. (b) The measured Duan values both minimum (squeezing) and maximum (anti-squeezing) at detuning 0 MHz as function of pump power from entangler JPC is shown alongwith the theory-fit including losses (orange curve) as well as ideal case (black dashed line) with zero loss	58
4.9	(a) Schematics of difference between reflection and phase-conjugation. (b) A schematic of Josephson Parametric Converter in non-degenerate mode where signal and idler photons emerge through two spatially separated resonators with pump interacting with the nonlinear element, that is Josephson ring modulator. (c) Observation of phase conjugation in JPC and differentiating it from the reflection.	61
4.10	(a) 20 MHz noise from AWG is fed to phase-conjugator at Idler port and the noise is phase-conjugated and frequency converted to signal frequency range. (b) Output phase-conjugated noise power as function of input noise power for different noise bandwidth is shown.	62
4.11	We mimic the target by combining a cryo 2:1 switch and a directional coupler to combine the noise in the path	63
4.12	(a) and (b) show the noise spectral density in the unit of quanta as function of temperature. From fitting them with Eq. (4.57) we obtain the effective gains and total noise added referenced at the temperature calibration tool respectively in two output detection chains	64
4.13	(a) The power difference between the beam-splitter outputs as function of pump phase of the phase-conjugator with respect to that of the entangler. (b) The calculated QI SNR as function of pump-phase of the phase-conjugator. Comparison between SNRs with QI and CS heterodyne receivers as (c) function of probing signal photon number N_S and (d) thermal noise present at the detection region N_B . In last two cases, the QI SNR value is taken at pump phase equivalent to zero from (b)	65
Α 1	Data acquisition with external trigger using dual-port memory [Alah] [Alaa]	82

B.1 Simulated example trajectories for the three possibilities of modeling dephasing of higher transmon levels for otherwise identical parameters (five transmon levels, $\gamma_1=0,\ \gamma_{\phi,1}/2\pi=50\ \text{kHz},\ \eta/2\pi=100\ \text{MHz},\ \kappa/2\pi=14.3\ \text{MHz})$: no dephasing (top), flux noise model (top, red), and charge dispersion model (bottom, blue). The last case leads to qualitatively incompatible results with very large noise levels and only partially stabilised attractors.

٠.

CHAPTER 1

Introduction

1.1 Background and Motivation

Quantum optics and quantum information science have revolutionized our understanding of light-matter interactions, enabling novel applications in computation, communication, and sensing. A central theme in these fields is the exploration of quantum-enhanced technologies, which leverage fundamental quantum properties such as superposition and entanglement to outperform classical counterparts. In this thesis, we investigate various aspects of quantum optics, with a focus on dissipative phase transitions in quantum systems and quantum-enhanced sensing, alongside the development of real-time digital signal processing techniques essential for experimental implementations.

One of the key phenomena explored in this thesis is the breakdown of photon blockade, which can be understood as a dissipative phase transition in a driven-dissipative zero-dimensional cavity-qubit system. Studying such non-equilibrium quantum phase transitions provides valuable insights into the behavior of open quantum systems and their potential applications in quantum metrology and sensing. The transition between non-classical and classical states is thought to be governed by quantum fluctuations. Based on this, we believe that this system could potentially serve as a weak signal detector, where the injection of a weak signal may allow us to observe the transition, offering a promising application in quantum sensing.

In parallel with this investigation into dissipative phase transitions, we explore another quantum-enhanced sensing technique — Quantum Illumination (QI). QI utilizes entanglement to improve target detection, particularly in environments with high background noise. In the ideal theoretical framework, quantum illumination offers a significant advantage, providing up to a 3 dB quantum advantage in detection probability over the best classical schemes. However, experimentally realizing the QI protocol with a phase-conjugate receiver presents significant technical challenges, including idler-loss, noise added by amplifiers in the detection chain, and imperfections in beam splitters that limit performance. Overcoming these challenges is crucial to advancing quantum sensing technologies, and both the exploration of photon blockade breakdown and quantum illumination aim to push the boundaries of what is achievable in quantum sensing [FLP17a, YJ19].

1.2 Research Objectives

The overarching objective of this thesis is to experimentally investigate quantum phenomena in cavity-based quantum optics and quantum sensing, while also developing highly efficient digital signal processing (DSP) techniques to enhance data analysis and interpretation. Specifically, we focus on dissipative quantum phase transitions (QPTs) and their potential applications in quantum sensing, which naturally lead to our investigation of quantum illumination (QI) as an advanced detection protocol. Additionally, we develop and optimize DSP methods to extract meaningful information from quantum signals, improving data acquisition and analysis in these experiments.

A Quantum Phase Transition (QPT) is a fundamental phenomenon in many-body physics where a system undergoes a qualitative change in its ground state by varying an external parameter at zero temperature. QPTs can be broadly classified into first-order and second-order transitions. In a first-order transition, two macroscopically distinct states coexist over a finite range of the control parameter, while in a second-order transition, the phase change occurs abruptly at a well-defined critical point.

An experimentally relevant example of a first-order QPT is the breakdown of photon blockade, first proposed in Ref. [Car15] and later observed in driven-dissipative quantum systems [FDV $^+$ 17]. The photon blockade mechanism, analogous to Coulomb blockade [AL86], prevents multiple photons from occupying a cavity simultaneously due to strong light-matter coupling. In this regime, the system remains in a "dark" state, blocking the transmission of photons. However, when the photon flux increases beyond a critical threshold, the blockade breaks down due to competition between coherent external driving and dissipation, allowing the system to transition suddenly to a "bright" state with high photon occupation. This transition exhibits hysteresis and bistability, characteristic of first-order phase transitions.

While such transitions have been observed, a key challenge remains: how do we rigorously define "phases" and justify photon blockade breakdown as a first-order QPT? A defining feature of phase transitions is the existence of stable states that persist under continuous measurements. This behavior becomes clearly observable in the thermodynamic limit, where the system is large enough that fluctuations are minimized, and the states remain distinguishable even under constant observation. Although the Jaynes-Cummings model provides a neoclassical scaling argument [VDFD19], the predicted macroscopic behavior and associated critical exponents have not been experimentally confirmed.

To address this challenge, Chapter 3 presents a detailed experimental study of photon blockade breakdown, where we couple a single transmon qubit to a superconducting cavity with an in situ tunable bandwidth κ . By systematically increasing the ratio g/κ (coupling strength to dissipation rate), we approach the thermodynamic limit and observe progressively macroscopic behavior. At the highest realized $g/\kappa \approx 287$, the system switches between a bright coherent state (around 8×10^3 intracavity photons) and the vacuum state over a characteristic timescale as long as 6 seconds—approaching the ideal hysteresis limit expected for a true first-order transition. These findings, supported by neoclassical theory and quantum-jump Monte Carlo simulations (thanks to our collaborator Andras), not only deepen our understanding of driven-dissipative quantum physics, but also reveal potential applications in quantum sensing and metrology.

The system's sensitivity to weak perturbations highlights its potential as a high-precision sensor, where even a small input signal—such as a single photon—might induce transitions between metastable states, enabling nonlinear amplification of weak signals. This makes

photon blockade breakdown (PBB) an attractive candidate for quantum-enhanced sensing [DCMP⁺23], particularly in scenarios requiring detection of faint signals under noisy conditions [PWP⁺24, YJ19]. Exploring the use of PBB for weak signal detection in experiments is a promising future direction.

Several fundamental questions remain open. For instance, can the system detect signals that are on resonance with the system frequency, or is it more responsive in the dispersive regime—and how do its dynamical properties differ in each case? Is it possible to achieve sensitivity at the single-photon level, or does the onset of the phase transition require strong external driving? Additionally, how do key system parameters—such as light-matter coupling strength, detuning, or cavity decay—affect the detection threshold and switching dynamics? Another intriguing possibility is whether the system could be particularly sensitive to signals oscillating at the vacuum Rabi frequency, or whether it responds selectively to the occupation of specific transmon levels. Understanding these aspects will be essential to assess the viability and optimize the performance of PBB-based sensors.

A key challenge in these studies is accurately processing and interpreting quantum signals obtained from the experiments. The intricate nature of microwave quantum optics requires robust DSP techniques for tasks such as quadrature extraction, filtering noise, and enhancing the signal-to-noise ratio (SNR). These techniques are critical for observing bistability in single-shot measurements even in the presence of background noise and ensuring reliable data analysis.

While the photon blockade breakdown system has potential to provide a sensitive nonlinear response for weak-signal detection, another powerful quantum-enhanced sensing technique is Quantum Illumination (QI) [Sha20], which utilizes entangled photon pairs for target detection in the presence of strong background noise. Unlike classical detection methods, QI offers a theoretical 3 dB advantage in the error-probability exponent [GE09], making it particularly useful for scenarios where the return signal is weak and noise levels are high.

The key challenge in realizing QI lies in practical receiver implementations. In theory, QI offers its advantage when the average signal photon number N_S in the unit of ${\rm s}^{-1}\,{\rm Hz}^{-1}$ per mode is much smaller than the background noise N_B . While the optical regime does not face challenges due to competing background noise, the microwave regime presents more naturally higher background noise, making QI more interesting in this context. However, practical microwave QI receivers face significant challenges, especially when relying on Josephson junction (JJ) circuits at cryogenic temperatures such as their typical dynamic range being limited to <-100 dBm. The other challenges include idler loss, amplifier-added noise, and imperfections in beam splitters, all of which limit performance and make it difficult to realize microwave QI receivers for practical applications.

To experimentally investigate QI, Chapter 4 presents our progress (with collaboration from Shabir, Alejandro, Isabel, Joan, and Peter) in building a phase-conjugate receiver in the microwave regime at millikelvin temperatures. We use a Josephson Parametric Converter (JPC) as a source of entangled signal-idler pairs. The signal, after reflecting from a target, is sent into another JPC operated in phase-conjugation mode, where it undergoes phase conjugation before being mixed with the idler in a beam splitter. By analyzing the residual correlations between the signal and idler, we benchmark the system's performance and assess the expected error probability enhancement. We also investigate the noise power handling of the phase-conjugate receiver, which approaches room-temperature values after suitable filtering.

1. Introduction

Just as DSP is crucial for interpreting quantum phase transition data, it is equally essential in quantum illumination experiments, where we analyze two-mode squeezed vacuum states, signal-idler correlations in the presence as well as in the absence of target. The high-efficiency DSP techniques developed in this work play a key role in extracting weak quantum signals buried in thermal noise, ensuring accurate benchmarking of the phase-conjugate receiver for QI.

To address this, I, with Przemislaw and Luka, have optimized all DSP routines in C++ using the Intel IPP library [Cor21], which is highly tuned for the Intel architectures used in our data processing servers. These routines are designed to handle signals captured from both AlazarTech ATS9870 (8-bit, 1 GS/s) and ATS9371 (12-bit, 1 GS/s) digitizers. These boards support sustained streaming over PCle at rates up to 1.6 GB/s, which we fully leverage by implementing a multithreaded buffering and analysis architecture capable of handling data in real time with a duty cycle exceeding 95%. This capability is crucial for obtaining high-quality statistics in experiments involving low SNR sensing and tomography.

Both research directions—photon blockade breakdown and quantum illumination—contribute to the broader goal of developing quantum-enhanced sensing techniques. Alongside these experimental studies, this thesis also emphasizes the importance of digital signal processing in quantum microwave engineering. Together, these advances in quantum sensing, phase transitions, and DSP techniques push the boundaries of quantum metrology, offering new pathways for ultra-sensitive detection in both classical and quantum-limited regimes.

Quantum Signal Analyzer

Contributions and collaborations

This work is based on the signal analysis techniques described in [Lan14]. Unlike their FPGA-based implementation, we have implemented these techniques in C++ on an Intel processor [GBA $^+$ 19], utilizing the Intel IPP library [Cor21]. We are especially grateful to Max Hofheinz from Université de Sherbrooke for introducing us to digital signal processing development in C++ using Intel IPP.

We also thank Stefano Elefante and Alois Schloegl from the Scientific Computing team at ISTA for their support in establishing the C++ platform, enabling us to control AlazarTech digitizers in C++. This platform served as the foundation for further in-depth development of digital signal processing.

I would like to sincerely express my gratitude to Przemysław Zieliński for his invaluable assistance in developing the C++ programs and integrating them with the VIP GUI using Python. Additionally, I appreciate the contributions of Georg Arnold and Elena Redchenko in refining certain techniques and assisting with debugging. Finally, I would like to thank Luka Drmic for his efforts in understanding and developing acquisition programs for the Alazar digitizers.

2.1 Introduction

Digital Signal Processing (DSP) plays a crucial role in the advancement of quantum technologies, where high precision and real-time signal manipulation are essential for extracting meaningful data from quantum systems. In experiments with superconducting quantum circuits, microwave signals are often used for controlling qubits and measuring their states and observing quantum optical phenomena, requiring sophisticated signal processing techniques to ensure accurate detection and interpretation. As quantum technologies evolve, the demand for efficient and flexible digital signal processing (DSP) methods becomes increasingly important to handle the complexities of quantum measurements and the large volumes of data generated in such systems.

A common approach to implementing DSP in such experiments is to use field-programmable gate arrays (FPGAs) for real-time processing. However, FPGAs require specialized hardware development and often lack flexibility for rapid modifications. In our implementation, instead

of using FPGA-based processing, we utilize AlazarTech digitizers with 8-bit [Alab] and 12-bit [Alaa] resolution to acquire raw data, stream them to CPU memory with high bandwidth and implement DSP techniques in C++ using the Intel Integrated Performance Primitives (IPP) library [Cor21] [GBA $^+$ 19]. By leveraging multithreading and optimized DSP routines, we achieve efficient processing of quantum signals while maintaining the flexibility of software-based development.

In this chapter, we begin with an overview of microwave signal detection in Section 2, where we discuss the principles of homodyne and heterodyne detection and the importance of selecting an appropriate intermediate frequency (IF) to ensure alias-free data acquisition with the digitizer. This sets the foundation for Section 3, where we explore the digital signal processing (DSP) techniques applied to the acquired signals, including averaging, digital downconversion, power spectral density estimation, and correlation calculations. We also detail how the Intel IPP library was leveraged to optimize these operations, enhancing the efficiency of processing data acquired by the Alazar digitizer. Finally, in Section 4, we summarize our key findings and we compare the efficiency of our C++ implementation with FPGA-based processing, discussing the trade-offs between computational flexibility, real-time performance, and hardware constraints.

2.2 Microwave Signal Detection and Quantum Fields

In quantum systems, information is typically transmitted using a carrier signal, which facilitates efficient propagation through various mediums, such as free space, cables, and optical fibers. The most widely used method of transmission is amplitude modulation, wherein the quantum information is encoded onto the carrier signal. A key technique for extracting the encoded information is field quadrature extraction [Rad84] [Mit89] [WA92], which isolates the quantum field's quadratures—specifically, its amplitude and phase components. These quadratures essentially represent the encoded information. Let us explore this concept in more detail.

A propagating quantum field, such as an electromagnetic field E(t), is typically described by the following expression:

$$E(t) = S(t)e^{i\omega_c t}$$

$$= [I(t) + iQ(t)]e^{i\omega_c t}$$
(2.1)

Here S(t) represents the information of interest, being modulated by the carrier frequency ω_c . I(t) and Q(t) are the time-dependent amplitudes of the in-phase and out-of-phase quadratures, respectively. By isolating and measuring these quadratures, we can recover the field's amplitude and phase information.

In quantum mechanics, the electromagnetic field is described by field operators, specifically the annihilation a(t) and creation $a^\dagger(t)$ operators. These operators correspond to the quantum equivalent of the classical signal components. The annihilation operator a(t) reduces the photon number by one and contains information about the phase and amplitude of the quantum field. To relate the classical quadratures to quantum field operators, we use the position and momentum operators, which are analogous to the classical in-phase I(t) and quadrature Q(t) components, respectively. In the quantum description, these are given by:

$$I(t) \propto \frac{1}{\sqrt{2}}[a(t) + a^{\dagger}(t)]$$
 and $Q(t) \propto \frac{-i}{\sqrt{2}}[a(t) - a^{\dagger}(t)]$ (2.2)

Hence, the information of interest, which is a complex amplitude becomes:

$$S(t) = I(t) + Q(t) \propto a(t) \tag{2.3}$$

Field quadrature extraction is commonly achieved through downconverting the original signal E(t) to an intermediate frequency (IF) signal with frequency $\omega_{\rm IF}/2\pi$ either at $\omega_{\rm IF}=0$ (homodyne detection) or at $\omega_{\rm IF}\neq 0$ (heterodyne detection) and finally followed by acquisition with an analog-to-digital converter (ADC) and proper digital postprocessing.

2.2.1 Homodyne detection.

As shown in Figure 2.4 (a) an IQ mixer is generally used for this method. An IQ mixer has two inputs where one is used for the RF signal E(t) and the other one is used for Local Oscillator (LO) signal LO = $\cos(\omega_c t)$. Inside the IQ mixer the LO is split into two parts, of which, one part is phase shifted by $\pi/2$. The signal is also split and then multiplied with each part of the LO. The resulting signals are then filtered by low-pass filters (LPF). After filtering each output of the IQ mixer is digitized with a two-channel digitizer.

Although the homodyne signal is centered at DC (0 Hz), making it convenient to process, it is highly vulnerable to 1/f noise and signal drifts [SHS+07]. Additionally, homodyne detection requires careful calibration to mitigate imperfections that often arise in IQ-mixing. These imperfections include finite DC offsets in each quadrature, amplitude imbalances between them, and phase deviations that prevent the quadratures from achieving an exact $\pi/2$ phase separation. In contrast, heterodyne detection avoids these issue, eliminating the need for such calibrations. Furthermore, as illustrated in Fig. 2.4(b), heterodyne detection requires fewer hardware resources.

2.2.2 Heterodyne detection.

This method involves mixing the original signal E(t) with the LO using an RF mixer, to produce an IF signal with frequency $\omega_{\rm IF}/2\pi < f_S$ (f_S being the maximum sampling frequency of the ADC) followed by filtering with a band-pass filter (BPF) centered around the IF frequency and finally acquired with an ADC, as shown in Fig. 2.4 (b).

What happens if the IF is chosen lower than the signal bandwidth?

Choosing an intermediate frequency (IF) lower than the signal bandwidth in a heterodyne system can cause severe signal distortion, aliasing, and loss of information. The main reasons are as follows:

- **Self-interference.** A signal modulated at RF contains both upper and lower sidebands around the carrier frequency. The IF must be large enough to separate these sidebands after mixing to the downconverted IF. If the IF is too low compared to the signal bandwidth, the sidebands overlap, as can be seen in Fig. 2.4 (c). It causes distortion and loss of the original spectral information. This phenomenon is called aliasing in frequency conversion.
- Difficulty in filtering. Heterodyne detection depends on proper bandpass filters centered at the IF to reject any unwanted signal and noise. If IF is too low, the filter

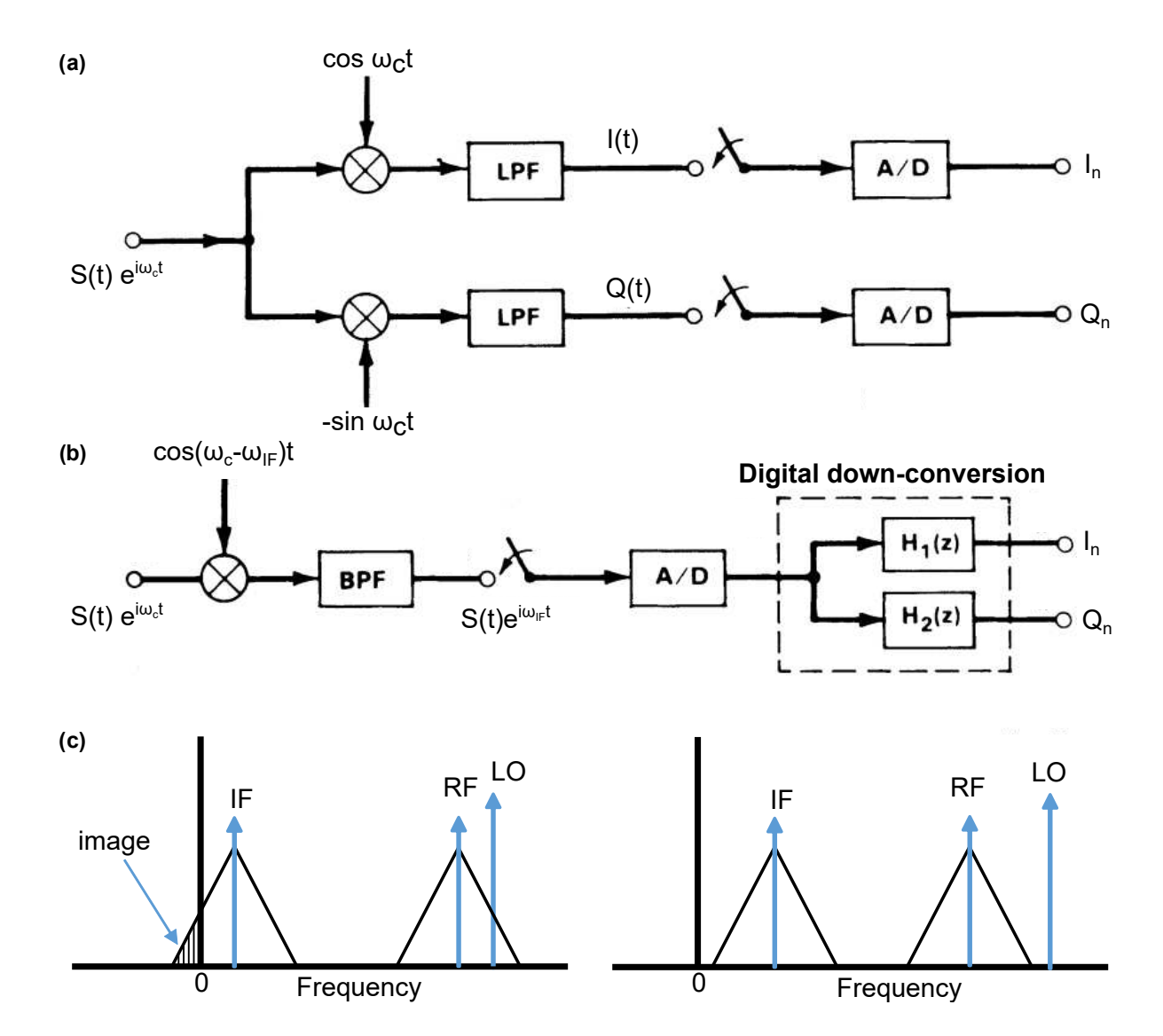


Figure 2.1: Field quadrature extraction with **(a)** homodyne and **(b)** heterodyne detection methods. [Rad84] **(c)** Schematics of importance of IF selection in the frequency domain. In the left schematic, if the IF is too small compared to the signal bandwidth B, part of the signal overlaps with its image frequency after down-conversion, causing interference. However, with a properly chosen IF (right schematic), this image interference can be effectively avoided, ensuring a cleaner signal.

cannot differentiate between the desired signal and interference, reducing the ability to reject noise and adjacent channel signals.

- Image frequency interference. The image frequency is given by $f_{\text{image}} = f_{\text{RF}} \pm 2f_{\text{IF}}$. For lower IF, the image frequency becomes closer to the desired signal, making it difficult to filter out which finally leads to image noise interference.
- Digitization problem. ADCs often have limited dynamic range and might not efficiently handle signals with very low IFs. The lower the IF, the harder it is to utilize the full range of the ADC, because low-frequency signals could be easily swamped by quantization noise or DC offset, leading to inaccurate sampling.

In conclusion, if the IF is chosen too low compared to the signal BW, the receiver will experience sideband overlap, poor filtering, increased image interference, and potential aliasing in the ADCs. This severely degrades signal quality and dynamic range. A properly chosen IF must be wide enough (at least 1.5 or 2 times the signal bandwidth) to preserve all spectral components while balancing filtering and image rejection challenges.

Importance of analog filter bandwidth.

After down-converting the signal to the IF, it is important to choose analog filter before digitizing the signal with some sampling rate. According to Nyquist-Shanon sampling criterion, the sampling frequency f_S must be at least twice the bandwidth of the signal B,i.e., $f_S \geq 2$ B. Generally, when we digitize a signal, it also comes with broadband noise (usually amplifier noise) existing at room-temperature. Hence, not only the signal bandwidth but also the noise bandwidth has to be considered while selecting analog low pass filter bandwidth. For example, we want to sample a signal with 1GS/s sampling rate, we should choose the bandwidth of the LPF to be at most 500 MHz in order to avoid aliasing of the broadband noise which leads to high noise detection and results in poor signal-to-noise-ratio (SNR).

2.3 Digital Signal Processing Implementation

By leveraging advanced algorithms, DSP facilitates tasks such as filtering, demodulation, and spectral analysis, which are critical for characterizing quantum states and enhancing experimental fidelity. This section outlines the Digital Signal Processing (DSP) methods implemented to process the signals from the quantum system after amplification, downconversion and analog to digital conversion. The key DSP operations include digital downconversion, spectral analysis, and cross-correlation, which are essential for extracting and analyzing the information encoded in the quantum field.

The processing was carried out using C++ in conjunction with the Intel IPP library, ensuring efficient and high-performance computation. These techniques enable precise extraction of the quantum field's quadrature components, which are crucial for accurate measurement and analysis.

2.3.1 Overview of DSP Methods Used

Here, the developed DSP techniques are described briefly. Through out this subsection, we assume that the signal acquired by the ADC is denoted as x(t).

1. Ensemble Average

Ensemble averaging involves collecting multiple measurements of a signal and averaging them to improve signal clarity. Specifically, if we perform r repetitions of a measurement, each lasting t seconds, we compute the average of these r measurements to obtain a single signal that still has a duration of t seconds. Mathematically, the averaged signal, $\langle x(t) \rangle$, is given by:

$$\langle x(t)\rangle = \frac{1}{r} \sum_{i=0}^{r-1} x_i(t) \tag{2.4}$$

where $x_i(t)$ represents the i^{th} measurement, and $\langle x(t) \rangle$ is the average signal over all r repetitions. This process reduces noise and enhances the signal's clarity by effectively smoothing out fluctuations. The resulting averaged signal will still be t-seconds long but represents a more reliable estimate of the true signal by combining information from all r repetitions.

2. Power spectral density (PSD)

PSD measurement involves Fast Fourier Transform (FFT) of the recorded signal x(t). FFT is nothing but an efficient algorithm used to compute the Discrete Fourier Transform (DFT) of a signal given by:

$$X_k = \sum_{n=0}^{N-1} x_n e^{-i2\pi kn/N}, \quad k = 0, 1, 2, ..., N - 1$$
 (2.5)

where x_n is the sampled/digitized time-domain signal x(t), N is the number of sample points, and X_k represents the frequency-domain representation at frequency bin k. The corresponding frequency for each bin k is:

$$f_k = \frac{kf_s}{N}, \quad k = 0, 1, 2, ..., N - 1$$
 (2.6)

It transforms a time-domain signal (with indices n) into its frequency components(with indices k), allowing us to analyze how signal power is distributed across different frequencies. Next, we calculate the power spectrum as function of frequency by taking the absolute squared value of the FFT:

$$P_k = |X_k|^2 \text{ in } V^2 / \text{RBW}$$

= $10 \log_{10}(|X_k|^2 \times 10^3 / 50\Omega) \text{ in dBm/RBW}$ (2.7)

Since the digitizer converts the digitized signal in Volts, the unit becomes $V^2/{\rm RBW}$, where RBW is Resolution Bandwidth. The RBW in the case of digitized signal is determined by the sampling frequency f_s of the digitizer and the number of sample points N in the DFT:

$$RBW = \frac{f_s}{N} \tag{2.8}$$

To improve the signal quality, we average this power (in linear) over multiple repetitions r, as explained in the ensemble averaging process:

$$\langle P_k \rangle = \frac{1}{r} \sum_{i=0}^{r-1} P_{k,i} \tag{2.9}$$

This mode is used as spectrum analyzer to analyze the signal frequencies present in the incoming signal as well as noise. Some of its applications have been discussed in Section 2.3.3.

3. Digital downconversion (DDC)

Digital downconversion is a process used to convert the IF signals by applying mathematical operations in the digital domain. The down-converted signal with IF frequency is acquired and digitized by an ADC which is then digitally post-processed to extract the quadratures which is discussed below.

Consider the acquired signal x(t), which is at frequency $f_{\rm IF}$ that is captured by a digitizer at a sampling rate f_S :

$$\begin{split} x(t) &= \frac{1}{2} \mathrm{Re}\{(S(t)e^{-i\omega_{\mathrm{IF}}t} + S^*(t)e^{i\omega_{\mathrm{IF}}t})\} \\ &= \frac{1}{2} (\mathrm{Re}\{S(t)\} \mathrm{cos}(\omega_{\mathrm{IF}}t) - \mathrm{Im}\{S(t)\} \mathrm{sin}(\omega_{\mathrm{IF}}t)) \end{split} \tag{2.10}$$

Here, S(t) = I(t) + iQ(t) is the complex envelope of the signal x(t) with in-phase (I) and quadrature (Q) components. The downconversion process involves multiplying the received signal by $\cos(\omega_{\rm IF}t)$ as well as $\sin(\omega_{\rm IF}t)$ which shift the signal frequency down to 0 Hz.

$$x(t) \times \cos(\omega_{\mathsf{IF}}t) = \frac{1}{2} (\mathsf{Re}\{S(t)\} \cos^2(\omega_{\mathsf{IF}}t) - \mathsf{Im}\{S(t)\} \sin(\omega_{\mathsf{IF}}t) \cos(\omega_{\mathsf{IF}}t))$$

$$= \frac{1}{4} (\mathsf{Re}\{S(t)\}(1 + \cos(2\omega_{\mathsf{IF}}t)) - \mathsf{Im}\{S(t)\} \sin(2\omega_{\mathsf{IF}}t))$$

$$= \frac{1}{4} \mathsf{Re}\{S(t)\} + \mathcal{O}(2\omega_{\mathsf{IF}}t)$$

$$(2.11)$$

and

$$\begin{split} x(t) \times \sin(\omega_{\mathsf{IF}}t) &= \frac{1}{2} (\mathsf{Re}\{S(t)\} \mathsf{cos}(\omega_{\mathsf{IF}}t) \mathsf{sin}(\omega_{\mathsf{IF}}t) - \mathsf{Im}\{S(t)\} \mathsf{sin}^2(\omega_{\mathsf{IF}}t)) \\ &= \frac{1}{4} (\mathsf{Re}\{S(t)\} \mathsf{sin}(2\omega_{\mathsf{IF}}t)) - \mathsf{Im}\{S(t)\} (1 - \mathsf{cos}(2\omega_{\mathsf{IF}}t)) \\ &= -\frac{1}{4} \mathsf{Im}\{S(t)\} + \mathcal{O}(2\omega_{\mathsf{IF}}t) \end{split} \tag{2.12}$$

Both operations shift the signal by $\omega_{\rm IF}$, hence the signal we are interested in is now moved to 0 Hz while there are still high-frequency components at $2\omega_{\rm IF}$, which are filtered out using a low-pass filter. The resulting signal consists of the in-phase $I(t)={\rm Re}\{S(t)\}$ and quadrature $Q(t)={\rm Im}\{S(t)\}$ components, ready for further digital processing according to requirements.

After digital downconversion to 0 Hz, a Finite Impulse Response (FIR) filter is applied to preserve both the amplitude and phase information of the signal while eliminating unwanted components. The FIR filter is crucial in the DDC process for the following reasons: (i)

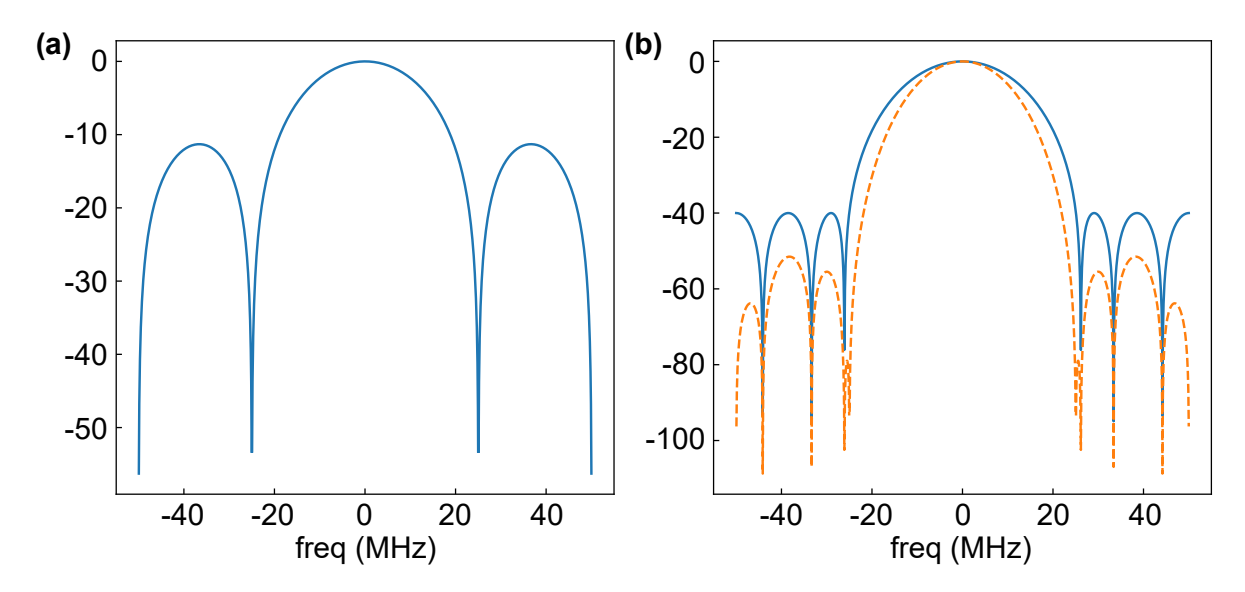


Figure 2.2: Frequency response of **(a)** 4-point boxcar window filter of cut-off frequency 25 MHz and **(b)** 7-point Dolph-Chebyshev window filter of cut-off frequency 26 MHz (blue solid line). The effective filter after combining both the filters is shown in dashed orange line.

Suppressing high-frequency components at $\pm 2\omega_{\text{IF}}$, (ii) suppress the dc offset which is now moved to $-\omega_{\text{IF}}$ and (iii) remove noise outside the signal bandwidth to improve the signal-to-noise ratio. FIR filters are particularly well-suited for this task because they provide linear phase response, preventing signal distortion, and allow for precise control over the filter's frequency response. Additionally, FIR filters maintain stability since they do not rely on feedback, making them a reliable choice for digital signal processing in quantum measurements.

To effectively filter the digitally downconverted signal, we applied two types of FIR filters, following the approach in [Lan14]. Ideally, after digitization, the signal has a bandwidth of $f_{\rm IF}$. To suppress unwanted spectral components, we first apply a simple windowed FIR filter and then refine the filtering using a Chebyshev FIR filter Fig. 2.2.

- Windowed FIR filter: The first filter is a basic N-point square window filter designed with a cutoff frequency matching $f_{\rm IF}$. The filter kernel consists of $N=f_S/f_{\rm IF}$ coefficients, each set to 1/N, ensuring that their sum is normalized to 1 [Lyo96]. This filter is highly effective at suppressing spectral components at integer multiples of $\pm f_{\rm IF}$, achieving at least 50 dB of attenuation, as demonstrated in Fig. 2.2 (a) for $f_{\rm IF}=25$ MHz. The sharp cutoff characteristic of this filter plays a critical role in mitigating the effect of unwanted LO leakage at these integer multiples of $\pm f_{\rm IF}$. However, due to the sinc-shaped frequency response of the filter, residual side-lobe components persist.
- Chebyshev FIR Filter: To further suppress these side-lobe components, we apply a Dolph-Chebyshev windowed FIR filter. This filter is chosen for its steep roll-off and excellent stopband attenuation, providing strong suppression beyond the desired cutoff frequency. As shown in Fig. 2.2 (b) in solid blue line, a Dolph-Chebyshev filter with a suppression of more than 40 dB at $f_{\rm IF}=25$ MHz significantly reduces unwanted spectral components. The suppression level can be adjusted in Python to optimize performance. Given a prescribed side-lobe ripple-magnitude r and main-lobe width $2\omega_{\rm IF}$, the required

window length M is given by [Lyn97]

$$M = 1 + \frac{\cosh^{-1}(1/r)}{\cosh^{-1}[\sec(\omega_{\mathsf{IF}}/2)]}$$
 (2.13)

This filter generally determines the final resolution bandwidth of the signal. Its cutoff frequency is chosen based on the signal's bandwidth and is usually lower than the IF, often on the order of the desired resolution bandwidth.

We can use a combination of both filters depending on the specific requirements (as illustrated by the dashed orange line in Fig. 2.2(b), where both filters have cut-off frequencies centered at the IF of 25 MHz). For example, to extract the quadrature components of a signal with an intermediate frequency (IF) of 25 MHz and a bandwidth of 5 MHz, we can fix the cut-off frequency of the first filter at the IF to isolate the desired frequency band. By setting the second filter to have a narrower bandwidth of 5 MHz—effectively acting as a resolution bandwidth (RBW) filter—we can improve the signal-to-noise ratio (SNR). This is because the narrower second filter limits the noise bandwidth, reducing the amount of noise integrated during detection while preserving the signal, thereby enhancing the overall SNR.

To extract the averaged quadratures of a signal, we first perform the ensemble averaging on the signal x(t), yielding $\langle x(t) \rangle$. Then, we apply the Digital Downconversion (DDC) operations to the averaged signal $\langle x(t) \rangle$, which returns the averaged quadratures: $\langle I(t) \rangle$ and $\langle Q(t) \rangle$. Since DDC is a combination of linear operations, the order of averaging and applying DDC does not affect the result. To optimize computational efficiency, we perform the DDC on the averaged, digitized signal.

4. Time-dependent power

In this mode, we perform DDC on the acquired signal and then we compute the averaged RMS (root mean square) power of the signal in V^2 as:

$$\bar{P}(t) = \langle S^*(t)S(t)\rangle
= \langle I^2(t) + Q^2(t)\rangle$$
(2.14)

Since squaring is a non-linear operation, the order of averaging and squaring matters. If we first average the acquired signal and then compute the power by performing the absolute square, this will only yield the power of the coherent component of the incoming signal. However this method accounts for both coherent (signal) and incoherent (noise) power because each repetition's power is considered individually. The averaging reduces the random noise variations, but it still includes the noise that was present in each individual repetition. In other words, you are computing the power from each repetition first, and then averaging those values, which includes noise at all stages.

5. Time-dependent cross power

The digitizer can acquire signals through its two inputs and after performing DDC on each acquired signal we obtain $S_{\mathsf{x}}(t) = I_{\mathsf{x}}(t) + i\,Q_{\mathsf{x}}(t)$ and $S_{\mathsf{y}}(t) = I_{\mathsf{y}}(t) + i\,Q_{\mathsf{y}}(t)$. The averaged cross power between these two signals will be calculated as:

$$\bar{P}_{xy}(t) = \langle S_x^*(t) S_y(t) \rangle \tag{2.15}$$

The averaged cross-power over repetitive measurements gets rid of uncorrelated noise in two input channels to the digitizer, which helps in improving SNR of the signal detected.

6. First-order correlation

In quantum optics, first-order correlation functions are used to analyze coherence, interference and fluctuations in a quantum system. Generally, the first order autocorrelation is represented as [Gla63]

$$G^{(1)}(\tau) = \langle E^*(t)E(t+\tau)\rangle \tag{2.16}$$

where, E(t) is electric field at time t, $\langle . \rangle$ is the ensemble average and τ is the time delay. Given a time-domain signal after DDC S(t) = I(t) + iQ(t), its first order correlation function is:

$$\Gamma^{(1)}(\tau) = \langle S \star S \rangle(\tau)$$

$$= \sum_{t=0}^{T-t_s} S^*(t)S(t+\tau)$$
(2.17)

where $S^*(t)$ is complex conjugate of S(t), \star represents the correlation function and τ is the time delay in the range between $[-T/2, T/2 - t_s]$ with t_s being the time resolution of the signal and T being the total captured time of the signal.

In other words, time-dependent first order correlation is nothing but Inverse Fourier Transform (IFT) of PSD of a signal,

$$\Gamma^{(1)}(\tau) = F^{-1}(F^*(S) \times F(s))(\tau) = F^{-1}(\mathsf{PSD})(\tau)$$
 (2.18)

with F^{-1} is IFT. At $\tau = 0$, $\Gamma^{(1)}(\tau = 0)$ essentially gives an integrated power measurement over all frequencies, which is equivalent to the total signal intensity.

7. First-order cross-correlation

The first-order cross-correlation function measures the temporal coherence between two signals, typically from two different field components. Consider two downconverted signals $S_{\mathsf{x}}(t)$ and $S_{\mathsf{v}}(t)$, The first-order cross-correlation function is defined as:

$$\Gamma_{xy}^{(1)}(\tau) = \langle S_{x} \star S_{y} \rangle (\tau)$$

$$= \sum_{t=0}^{T-t_{s}} S_{x}^{*}(t) S_{y}(t+\tau)$$
(2.19)

Similar to the autocorrelation, first order cross-correlation is nothing but IFT of cross-PSD:

$$\Gamma_{xy}^{(1)}(\tau) = F^{-1}(F^*(S_x) \times F(s_y))(\tau)$$
(2.20)

This measurement is particularly useful for eliminating uncorrelated noise from two signal inputs to the digitizer. When the desired signal is split into two channels using a beam splitter, cross-correlation helps isolate the correlated components while suppressing independent noise contributions [LBE+11].

8. Second-order autocorrelation

The second-order autocorrelation function quantifies the correlation of a signal's intensity at different time delays. Given the signal after DDC being S(t), the second-order autocorrelation function is,

$$\Gamma^{(2)}(\tau) = \langle |S(t)|^2 \star |S(t)|^2 \rangle = \langle |S(t)|^2 |S(t+\tau)|^2 \rangle$$
 (2.21)

The second-order autocorrelation is primarily used to distinguish different types of light sources.

- Coherent light (e.g., laser): $\Gamma^{(2)}(\tau)/\Gamma^{(2)}(0) = 1$ confirms the poissonian statistics of the photons coming from the source.
- Thermal light (e.g., room temperature noise): $\Gamma^{(2)}(\tau)/\Gamma^{(2)}(0)=2$ shows photon bunching effect.
- Single-photon sources (e.g., two-level system): $\Gamma^{(2)}(\tau)/\Gamma^{(2)}(0) < 1$ shows photon antibunching effect.

Such source characterization using a light source (classical or non-classical) and a single detector using second-order autocorrelation has been shown in $[SSH^+12]$.

9. Second-order cross-correlation

To achieve a good signal-to-noise ratio (SNR) in second-order correlation measurements, a large amount of averaging is typically required to suppress noise, as the signal of interest is often much weaker than the surrounding noise. However, a more efficient approach to improving SNR with fewer averaging cycles is to utilize cross-correlation, as previously discussed in the first-order case. By measuring correlations between two separate signal outputs, the uncorrelated noise in each channel cancels out, enhancing the measurement quality. Given the digitally downconverted signals $S_x(t)$ and $S_y(t)$ from two independent detection channels, the second-order cross-correlation function can be computed as:

$$\Gamma_{\mathsf{x}\mathsf{y}}^{(2)}(\tau) = \langle (S_{\mathsf{x}}^* S_{\mathsf{y}}) \star (S_{\mathsf{x}} S_{\mathsf{y}}^*) \rangle \tag{2.22}$$

This approach offers a more reliable means of extracting correlation information while effectively suppressing uncorrelated noise, resulting in a higher-fidelity measurement. Notably, using the Hanbury Brown and Twiss (HBT) setup, this method has been employed to distinguish between coherent and single-photon sources, as demonstrated in $[BLS^+11]$.

2.3.2 Implementation with Intel IPP Library

To efficiently process the acquired signals, we utilize the Intel Integrated Performance Primitives (IPP) library [Cor21], which provides optimized functions for common digital signal processing (DSP) operations. This ensures efficient execution by leveraging SIMD (Single Instruction, Multiple Data) and multi-threading capabilities of modern Intel processors. Below, we outline how different DSP tasks were implemented using specific IPP functions.

Fast fourier Transform (FFT) for Frequency Analysis

To transform time-domain signals into the frequency domain, we use Intel IPP's FFT functions. The function "ippsDFT_fwd" is used to compute the Discrete Fourier Transform (DFT) efficiently:

```
ippsDFT_fwd_32f(signal_in , fft_out , fft_spec , buffer);
```

Here, "signal_in" is the input signal, "fft_out" stores the transformed data, "and fft_spec" contains precomputed FFT parameters for efficiency. The buffer is allocated separately using "ippsDFTInitAlloc".

Digital Downconversion (DDC)

Downconversion is implemented by multiplying the acquired intermediate frequency (IF) signal with sine and cosine waves to shift it to 0 Hz. This is achieved using the vectorized multiplication function:

```
ippsMul_32f(signal_in , cos_wave , l_out , length);
ippsMul_32f(signal_in , sin_wave , Q_out , length);
```

Here, "signal_in" is the digitized IF signal, "cos_wave" and "sin_wave" are precomputed sine/cosine waveforms, and "l_out" and "Q_out" store the in-phase (I) and quadrature (Q) components, respectively.

To remove unwanted frequency components and improve signal-to-noise ratio (SNR), we apply a Finite Impulse Response (FIR) filter using IPP's convolution function:

```
ippsFIRSR_32f(I_out, filtered_I, num_samples, fir_state);
ippsFIRSR_32f(Q_out, filtered_Q, num_samples, fir_state);
```

Here, "fir_state" is initialized using ippsFIRSRInitAlloc, and "filtered_I" / "filtered_Q" store the filtered I and Q signals.

Power Spectral Density (PSD) Calculation

Power spectral density is computed by squaring the magnitude of the FFT output and normalizing it over the total number of samples:

```
ippsPowerSpectr_32f(fft_out, psd_out, num_samples);
```

This function efficiently computes $|FFT(signal)|^2$, providing frequency-domain power information.

Correlation functions

The autocorrelation and cross-correlation functions are computed efficiently leveraging the FFT. The standard approach, applicable to both first-order and second-order correlation functions, follows these steps as described in the previous section:

(i) Compute the Fourier Transform (FT) of the signal(s),

```
// Assume src1 and src2 are input complex signals (Ipp32fc arrays)
IppStatus status;
status = ippsFFTFwd_CToC_32fc(src1, fft1, pFFTSpec, pFFTBuffer);
status = ippsFFTFwd_CToC_32fc(src2, fft2, pFFTSpec, pFFTBuffer);
```

with "src1", "src2" being input complex signals; "fft1", "fft2" being output arrays storing FFT results; "pFFTSpec" being precomputed FFT specification and "pFFTBuffer" being temporary buffer for FFT computation.

(ii) Multiply the transformed signal by its complex conjugate (for autocorrelation) or by the complex conjugate of another signal (for cross-correlation)

```
// For autocorrelation
ippsConj_32fc(fft1, fft1_conj, fftSize);
ippsMul_32fc(fft1, fft1_conj, fft_mult, fftSize);
//For cross-correlation
ippsConj_32fc(fft2, fft2_conj, fftSize);
ippsMul_32fc(fft1, fft2_conj, fft_mult, fftSize);
```

"ippsConj_32fc()" computes complex conjugate of "fft1" or "fft2" and stores in "fft1_conj" or "fft2_conj" respectively. "ippsMul_32fc()" computes multiplication between either "fft1" and "fft1_conj" or "fft1" and "fft2_conj" depending on auto- or cross-correlation and store them in "fft mult".

and (iii) Perform the Inverse Fourier Transform (IFT) to obtain the correlation function in the time domain.

```
ippsFFTInv_CToC_32fc(fft_mult, correlation, pFFTSpec, pFFTBuffer);
```

It performs inverse-FFT of "fft_mult" and store it in "correlation".

2.3.3 Application of DSP in Our Lab

In this section, I will discuss the experimental projects in our lab where the above-described DSP techniques have been applied for signal processing and analysis.

Observation of collapse and revival in a superconducting atomic frequency comb [RZicvcv⁺25]

This project aimed to experimentally observe the collapse and revival dynamics of a single microwave excitation interacting with a superconducting atomic frequency comb (sAFC). To capture these dynamics, the output signal was downconverted to an intermediate frequency (IF) of 250 MHz and recorded using a 12-bit Alazar digitizer operating at a 1 GHz sampling rate. The recorded data was processed in C++ using the Intel IPP library, where digital

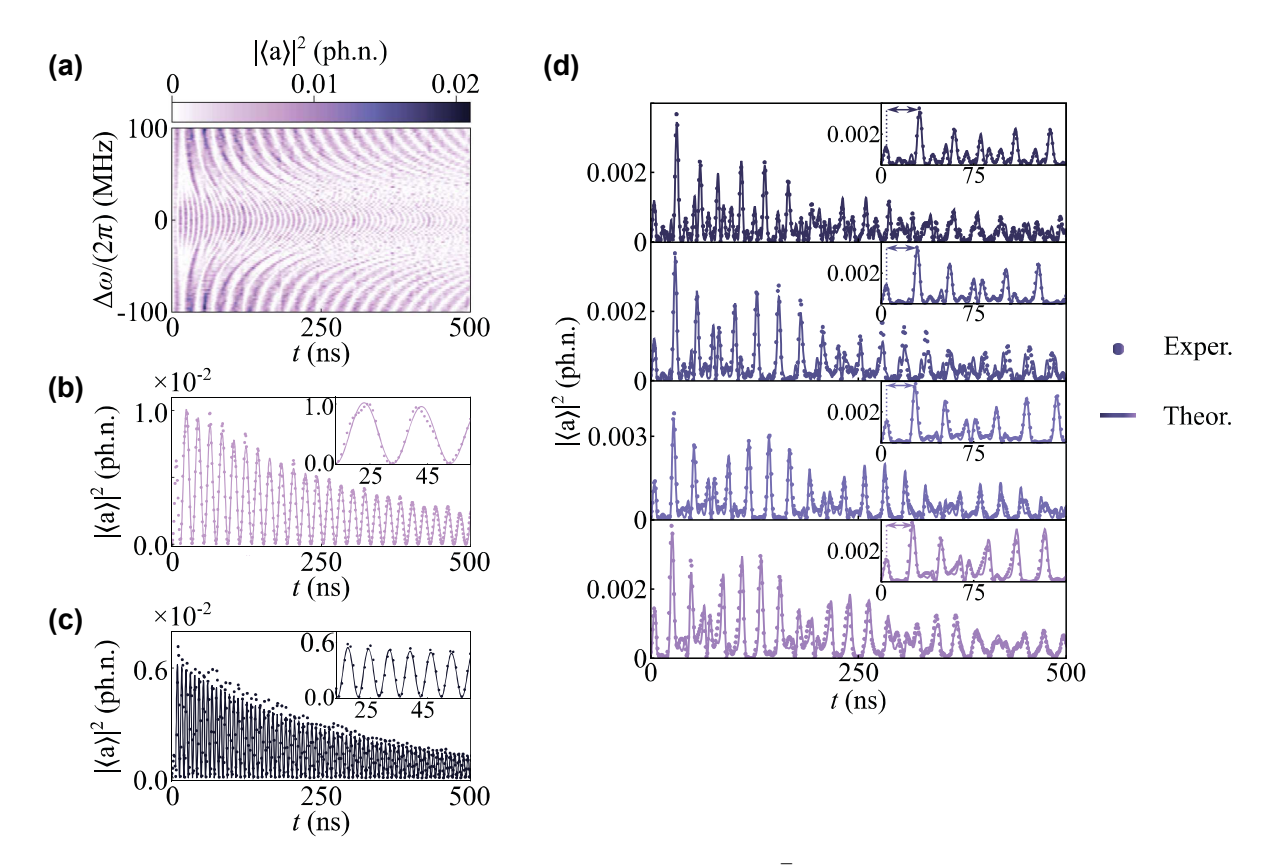


Figure 2.3: (Measured time-dependent averaged power $P(t) \propto |\langle a \rangle|^2$ for (a) different qubit detunings $\Delta \omega/2\pi$; (b) single qubit at $\Delta \omega/2\pi = 100$ MHz; (c) collective at $\Delta \omega/2\pi = 0$ MHz and (d) revival behavior at different $\Delta \omega$. This figure is taken from [RZicvcv⁺25].

downconversion was performed to extract the in-phase (I) and quadrature (Q) components, enabling the calculation of the time-dependent power:

$$\bar{P}(t) = |\langle S(t) \rangle|^2 \propto |\langle a(t) \rangle|^2$$
(2.23)

where S(t) = I + iQ(t) represents the complex field amplitude as already defined in Section 2.2. This time-domain power analysis provided insights into the system's behavior, consisting of five superconducting qubits coupled to a microwave resonator.

Fig. 2.3(a) presents the measured time-dependent power of the output field, scaled to photon number, following an initial microwave excitation. The signal exhibits a rapid decay, followed by periodic revivals, indicating the rephasing dynamics of the multi-qubit system. The x-axis represents the detuning $\Delta\omega$ (also referred to as comb spacing) of four qubits, while the central qubit remains resonant with the cavity mode ($\omega=\omega_c$).

Fig. 2.3(b) shows the vacuum Rabi oscillations of the central qubit when the comb spacing exceeds the coupling strength of the central qubit. These oscillations follow a damped sinusoidal behavior, from which the extracted vacuum Rabi frequency is 49.6 MHz, closely aligning with the expected coupling strength, $2g/2\pi$.

Fig. 2.3(c) depicts the collective Rabi oscillations observed when all five qubits are coupled to the resonator. A fit to the data reveals a collective Rabi frequency of 137.4 MHz, which closely matches the predicted collective vacuum Rabi splitting of $2G/2\pi=137.9$ MHz.

Finally, Fig. 2.3(d) illustrates the revival behavior of the excitation across different values of $\Delta\omega$. These revivals emerge as the excitation dynamically rephases within the five-qubit ensemble, periodically reconstructing the output field. The observations provide experimental validation of coherent energy exchange within an engineered superconducting atomic frequency comb, demonstrating its potential for applications in quantum memory and engineered light-matter interactions.

Observation of Mollow Triplet

In a resonantly coupled cavity—transmon system, driving the lower vacuum-Rabi peak of the resulting vacuum-Rabi split spectrum leads to the emergence of a distinct emission feature known as the Mollow triplet [Mol69]. The power spectral density (PSD) of the downconverted signal—centered at an intermediate frequency (IF) of 20 MHz and averaged using a digitizer—reveals two primary components: a sharp Rayleigh peak, representing coherent (elastic) scattering, and a broader spectral distribution due to incoherent resonance fluorescence.

The Rayleigh peak corresponds to the coherent part of the emitted field and appears as a narrow spike in the PSD. In contrast, the incoherent emission—observable after digitally suppressing the Rayleigh peak using a band-stop or notch filter—exhibits the resonance fluorescence spectrum. As shown in Fig. 2.4(a), this spectrum features a central Lorentzian peak at the IF and two symmetrically shifted sidebands, forming the characteristic Mollow triplet.

To isolate the resonance fluorescence spectrum, we performed two types of measurements: one with the system continuously driven ("on"-measurement) and one with the drive turned off ("off"-measurement). By dividing the PSD of the on-measurement by that of the off-measurement (in linear scale), we effectively cancel out the background noise introduced by the detection chain, revealing the true spectral signature of the quantum system.

The frequency separation between the central peak and the sidebands corresponds directly to the Rabi frequency of the drive, serving as a clear signature of a driven two-level system in the strong driving regime. The observation of the Mollow triplet thus provides a fundamental confirmation of coherent quantum control and light–matter interaction at the level of individual quanta.

Observation of Modulated Mollow resonance fluorescence [RPS+23]

In the work of [RPS $^+23$], based on the PSD of recorded data, the incoherent resonance fluorescence spectrum has been observed in the form of the Mollow triplet when a qubit is coupled to a transmission line and driven on resonance. This Mollow spectra has been shown to be modulated, leading to the formation of nested Mollow triplets with modulating the qubit frequency, as shown in Fig. 2.4(b)

Second-order cross-correlation

We tested the second-order cross-correlation program, implemented with C++ and python, on both coherent and thermal states. To generate a coherent state, we used an arbitrary waveform generator (AWG) to produce a sinusoidal signal with a frequency of 20 MHz and an amplitude of 100 mV_{p-p}, splitting them with a 90 degree hybrid followed by feeding them directly into a digitizer. Running the code of second order cross-correlation, we measure the cross-correlation of the powers from the outputs of the hybrid as $\Gamma_{xy}^{(2)}(\tau)$. To normalize this

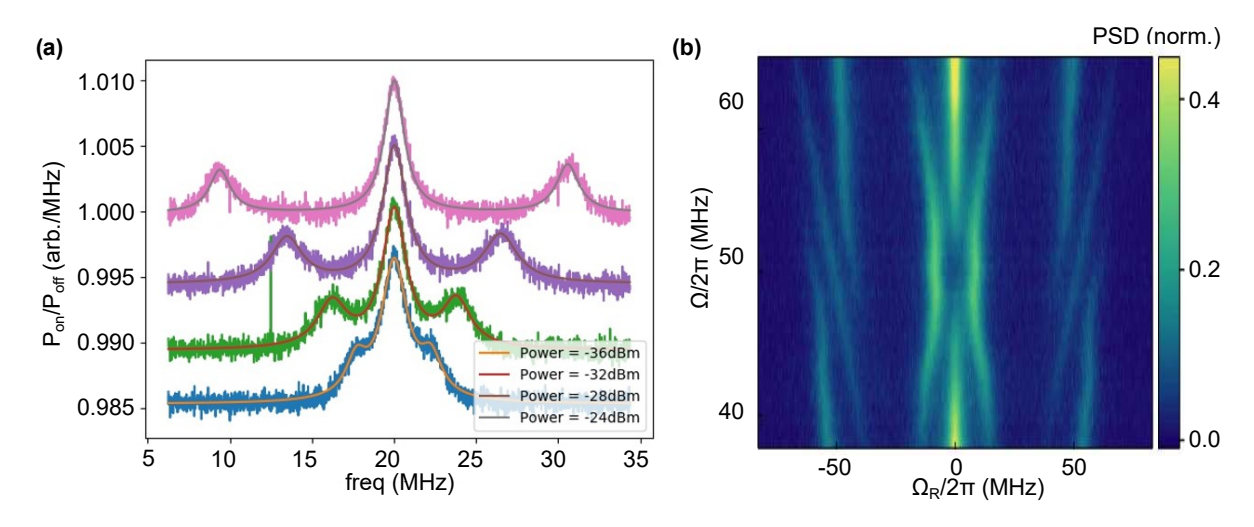


Figure 2.4: Field quadrature extraction with (a) Mollow triplet of a resonantly driven two-level system after omitting Rayleigh peaks is observed using PSD script. (b) Measured resonance fluorescence emission spectrum of qubit as a function of the modulation frequency Ω and detuning of the detected inelastically scattered radiation from the drive applied at ω_0 for a Rabi frequency $\Omega_{\rm R}/2\pi=52$ MHz and modulation amplitude $A_m=0.2\,\Omega_{\rm R}$ [RPS+23].

cross-correlation to unity at time delays $\tau \to \infty$, we divide $\Gamma^{(2)}_{xy}(\tau)$ by by its value at the largest time delay, yielding the normalized second-order correlation function $g^{(2)}(\tau)$, as shown in Fig. 2.5(a). As expected for a coherent state, $g^{(2)}(\tau)$ remained unity for all time delays, confirming the Poissonian photon statistics characteristic of a coherent state.

To examine the thermal state, we configured the same AWG to generate Gaussian noise with a bandwidth of 80 MHz and an amplitude of $100 \mathrm{mV_{p-p}}$, splitting them with a 90 degree hybrid followed by feeding them directly into a digitizer. In this case, the computed $g^{(2)}(\tau)$, shown in Fig. 2.5(b), exhibited the well-known bunching behavior of thermal light, where $g^{(2)}(\tau=0)=2$. The linewidth of this correlation is determined by the digital filter bandwidth which is 20 MHz. By adjusting this bandwidth, the temporal width of the $g^{(2)}(\tau)$ function can be controlled accordingly.

To accurately observe the second-order cross-correlation in the single-photon regime, it is typically necessary to perform measurements both when the source is active and when it is off. The off-source measurements help subtract the constant noise introduced by the detection chain, allowing for the clear observation of the second-order cross-correlation behavior of a very weak signal. However, in the tests described above, we used signals with relatively large amplitudes compared to the existing background noise, so on-off measurements were not required in these particular cases.

Temperature Calibration

In certain experiments, it is crucial to analyze measurements referenced at the output of the sample, rather than at the end of the entire detection chain. This necessitates precise calibration of the noise introduced by the detection chain at the specific frequency of interest, enabling the extraction of key system parameters, such as the gain G and the added noise per mode $(n_{\rm add})$ within the detection chain. We perform such calibrations by measuring DDC of the noise at the frequency of interest at different temperatures of the calibration tool (containing a temperature sensor and a heater attached to the place referenced to where we

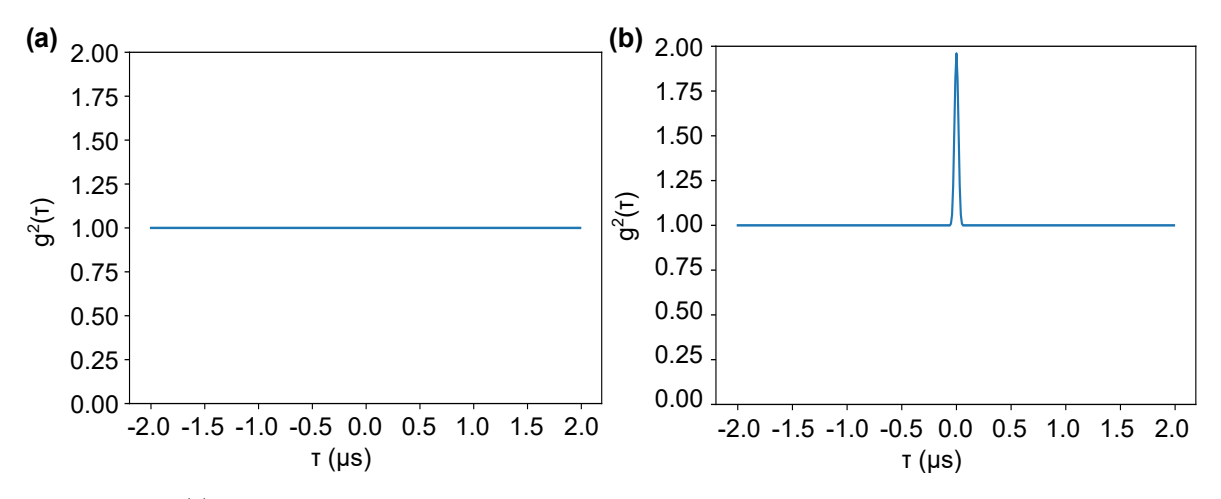


Figure 2.5: $g^{(2)}(\tau)$ is shown for (a) a coherent state and (b) broadband noise, generated from an AWG.

want to know the system parameters of the detection chain inside the dilution refrigerator we use). From the DDC measurements which are around 5-10 minutes long measurements, we average the power calculated from the extracted quadratures. An example of such averaged power as function of temperature is shown in Fig. 2.6, where the IF is at 100 MHz, and the measurement bandwidth is B = $250~\rm kHz$. This noise power spectral density as a function of temperature at a given frequency ω follows:

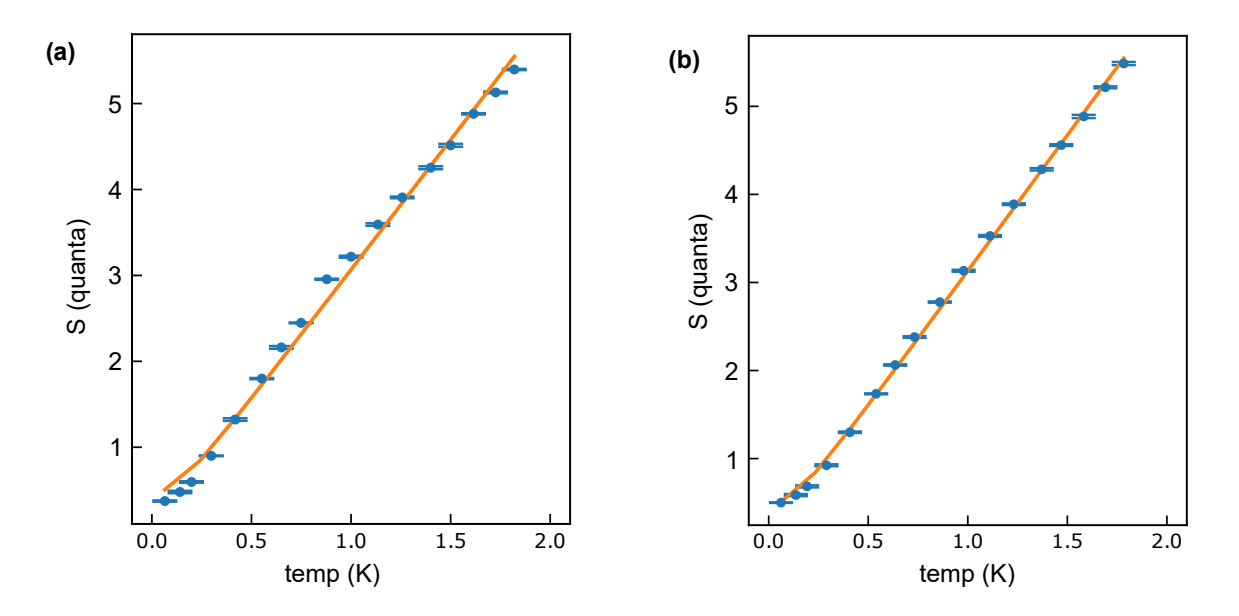


Figure 2.6: (a) and (b) show the noise spectral density in the unit of quanta as function of temperature. From fitting them with Eq.(4.57) we obtain the effective gains and total noise added referenced at the temperature calibration tool respectively in two output detection chains

$$N=\hbar\omega \mathrm{BRG}[\frac{1}{2}\mathrm{coth}[\frac{\hbar\omega}{2k_{\mathrm{B}}\mathrm{T}}]+n_{\mathrm{add}}]$$

Here, N is the measured noise power spectral density, \hbar is the reduced Planck's constant, B is the measurement bandwidth, R = 50Ω , $k_{\rm B}$ is the Boltzmann constant, T is the temperature

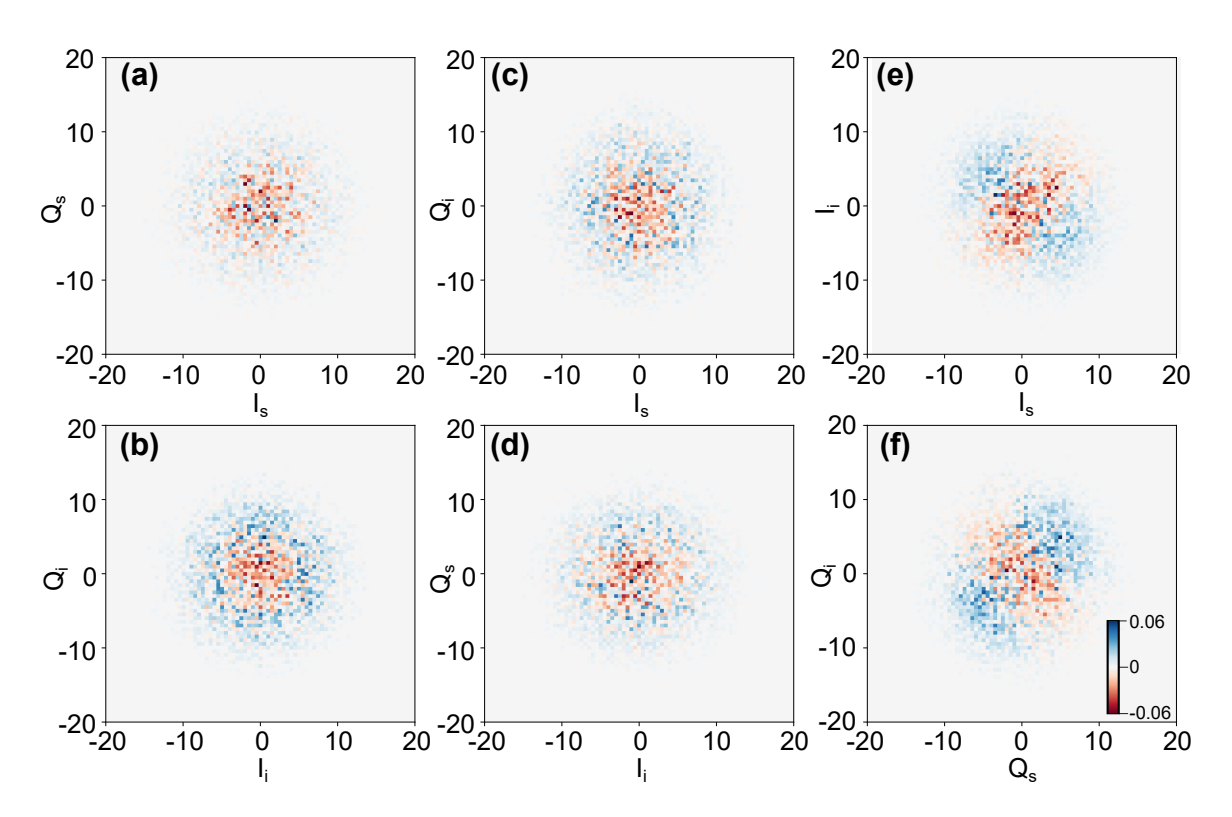


Figure 2.7: The difference between quadrature histograms with the JPC pump on and off for various quadrature pairs.

of the sample output reference. From fitting the experimentally obtained noise power with the formula as shown in orange line in Fig. 2.6 we can extract G and $n_{\rm add}$. For further details please see Section 4.5.5 in Chapter 4.

Observation of Two-Mode Squeezing

Two-mode squeezing (TMS) refers to the quantum phenomenon in which correlations are induced between the quadratures of two separate modes of the electromagnetic field. In two-mode squeezing, the variance of one mode's quadrature is squeezed below 1/2, while the variance of the conjugate quadrature in the other mode is simultaneously increased, ensuring that the total uncertainty across both modes adheres to the uncertainty principle [Cav81, Cav82, CS85]. This manipulation of the quantum state reduces noise in one mode while increasing it in the conjugate mode, effectively creating a squeezed vacuum state across both modes. From a DSP perspective, observing two-mode squeezing involves measuring and analyzing the quadratures of the two modes of interest using DDC. This technique has been successfully employed to observe two-mode squeezed vacuum states from non-degenerate parametric amplifiers (NDPA), such as Josephson Parametric Amplifiers (JPA) [EBL+11, EW14] and Josephson Parametric Converters (JPC) [AKD13, FRM+12].

For instance, we use a JPC where upon the amplification of pump at 17.06 GHz, the JPC generates two-mode squeezed signal and idler modes at 10.2 GHz and 6.86 GHz respectively. These signal and idler are downconverted to the IF of 100 MHz and recorded by two input channels of the digitizer at sampling frequency of 1GHz. By applying DDC With RBW = 250 kHz, we obtain the quadratures of signal $\{I_s,Q_s\}$ and idler $\{I_i,Q_i\}$ which contain 1.44×10^6 samples.

The DDC measurements are performed in two conditions: with the JPC pump off, capturing

primarily HEMT noise, and with the pump on, where two-mode squeezed vacuum is generated. When the JPC is continuously pumped, the signal captured by the digitizer contains both the generated signal/idler from the JPC as well as noise introduced by the detection chain. However, after the entangled signal and idler are produced, their interaction with the noise in the detection chain leads to the destruction of entanglement, making it impossible to observe the quantum correlations between the signal and idler.

To observe the two-mode squeezing as referenced at the JPC outputs in phase-space, it is essential to calibrate and subtract the noise. This is achieved by subtracting the quadratures obtained when the JPC is not pumped from the quadratures obtained when the JPC is pumped continuously, as illustrated in Fig. 2.7. Panels Fig. 2.7(a)-(d) show the quadratures with the pump on, subtracted by the quadratures with the pump off. In these histograms, no correlation is visible between the pairs $I_s - Q_s$, $I_i - Q_i$, $I_s - Q_i$ and $I_i - Q_s$; these distributions appear Gaussian, indicating equal uncertainty in all quadratures.

However, in panels Fig. 2.7(e)-(f), the distribution clearly shows an imbalance in the uncertainty between the quadratures. Further post-processing on these quadratures to extract covariance matrix and Duan-Simon criterion [DGCZ00] reveals squeezing in one of the quadratures below the vacuum level, indicating the presence of entanglement between the signal and idler modes. This process effectively visualizes the two-mode squeezed vacuum state and demonstrates the entanglement between the modes.

2.4 Conclusion

In this work, we explored various digital signal processing (DSP) techniques, including averaging, digital downconversion (DDC), power spectral density (PSD) estimation, power and cross-power analysis, as well as first- and second-order auto- and cross-correlations. We then discussed how these methods were applied in different experimental projects, highlighting their role in extracting meaningful information from detected signals.

For implementation, we used C++ with the Intel IPP library, achieving high efficiency for simple operations like averaging, which reached nearly 100% efficiency with capturing data with both input channels of the digitizer due to minimal computational overhead. However, as the complexity of the processing increased, efficiency dropped significantly. DDC achieved around 50% efficiency, time-dependent power estimation around 30%, and second-order correlations ranged between 10-20%, assuming the trigger time was equal to the digitizer acquisition time for dual channel acquisition. This decline is primarily due to increasing memory bandwidth constraints, processing latency, and the limits of sequential execution on CPUs. We define the efficiency as

$$\eta = \frac{t_{\text{ideal}}}{t_{\text{actual}}} \times 100 \,(\%) \tag{2.24}$$

where, $t_{\rm ideal}$ is the minimum time required to acquire and process a complete dataset in real time (i.e., before the arrival of the next trigger), and is calculated as $t_{\rm ideal} = t_{\rm trigger} \times 10^{10}$ number of averages. $t_{\rm actual}$ is the actual time taken by the host PC from the start of acquisition to the completion of processing.

As a concrete example, consider triggering the digitizer at 200 kHz, so $t_{\rm trigger}=5\,\mu s$. During each trigger, the digitizer acquires 4992 samples at 1GS/s sampling rate, corresponding to

4992 ns, or approximately 5 μ s - 100 % acquisition time per trigger. If we average over 500 records per buffer and use 400 buffers per acquisition (see Appendix A.3.1), the total ideal acquisition time becomes $t_{\rm ideal}=1$ s. Assuming two-channel acquisition, in the **Averaging** mode, the host PC completes processing in $t_{\rm actual}=1.005841$ s, yielding nearly 99% efficiency. In contrast, the **DDC** mode yields $t_{\rm actual}\approx 2$ s, resulting in $\eta\approx 50$ %. Further improvements in efficiency can be achieved via decimation and reduced acquisition time, as discussed in Appendix A.3.1.

A significant advantage of our approach is the throughput of measurements and data analysis. Our software framework is optimized to run many measurements in a short time, which is crucial for high-throughput experiments. As the data is acquired, we perform initial processing, such as taking the square of the signal, followed by downsampling. This downsampling step helps prevent the hard drive from becoming overwhelmed with data, ensuring that large datasets are efficiently stored and manageable. By balancing processing and downsampling, the system can continue to capture and analyze data continuously, achieving high throughput without sacrificing performance or storage capacity. For instance, we can perform PSD of 4096 sample points per trigger with $t_{\rm trigger}=5\mu{\rm s}$, with two-channel acquisition, sampling rate of 1GS/s with averaging over 10^6 measurements, typical throughput we achieve in the order of:

Throughput =
$$\frac{\text{Amount of data processed}}{\text{Time interval}}$$

$$= \frac{4096 \times 2 \times 500 \times 200}{5\text{s}}$$

$$= 163840000 \, \text{samples/second}$$
 (2.25)

FPGAs, in contrast, offer significantly higher efficiency for such tasks. They can fully parallelize operations, stream data continuously, and execute computations with minimal latency. Tasks such as DDC or real-time correlation computation can be implemented with near 100% efficiency on an FPGA. Moreover, FPGA systems are uniquely suited for implementing real-time feedback or feedforward control, which is critical for many quantum or low-latency experiments but is not feasible with software-based approaches due to the overheads of operating systems, memory access, and non-deterministic scheduling.

That said, FPGA-based processing has notable trade-offs. It often lacks the numerical flexibility of CPUs, particularly in floating-point arithmetic, making it resource-intensive to implement complex filters or low-frequency DSP operations (e.g., using large FIR filter kernels). Moreover, FPGA development requires specialized knowledge of hardware description languages (HDLs), long iteration cycles, and tight resource management, which can make it difficult to adapt rapidly to evolving experimental requirements.

On the other hand, C++ with Intel IPP provides a highly flexible and accessible platform for implementing and iterating on DSP algorithms. It supports more sophisticated and computationally intensive data analysis, including advanced statistics, machine learning, and adaptive processing methods that would be difficult to realize efficiently on FPGAs. The ease of debugging, visualization, and integration with analysis tools makes software-based DSP an excellent choice during development, testing, or in scenarios where flexibility and complexity outweigh the need for hard real-time performance.

Looking ahead, advancements in CPU architectures—such as wider vector units (e.g., AVX-512), better memory bandwidth, and improved multi-core scaling—are likely to close the gap

between software and hardware-based DSP, making software solutions increasingly viable for even demanding real-time applications.

Photon Blockade Breakdown Phase Transition

This chapter is based on the following publication:

Riya Sett, Farid Hassani, Duc Phan, Shabir Barzanjeh, Andras Vukics, and Johannes M. Fink. Emergent macroscopic bistability induced by a single superconducting qubit. *PRX Quantum*, 5:010327, Feb 2024

© 2011 by American Physical Society. All rights reserved. Reproduced with permission from the American Physical Society. The American Physical Society permits the use of published articles in a thesis or dissertation without requiring explicit permission, provided that proper bibliographic citation and copyright credit are given.

Contributions and collaborations

This work builds upon $[FDV^+17]$ and this chapter is primarily based on our recent publication $[SHP^+24]$. Andras Vukics from the Wigner Research Center for Physics developed the theoretical framework for this project and implemented all the necessary numerical simulations. In addition to contributing to the theoretical aspects, he authored a significant portion of $[SHP^+24]$, including an in-depth understanding of the thermodynamic limit and phase diagram, which serves as the foundation of this chapter.

Duc Phan designed the κ -tunable 3D cavity and simulated the quality factor as a function of the variable pin length inside the cavity using COMSOL. Under the supervision of Shabir Barzanjeh, he conducted the initial measurements of photon blockade breakdown as a function of drive amplitude for different κ values.

Shabir Barzanjeh contributed to the sample design and played a key role in setting up the experiment in the dilution refrigerator. I would also like to express my gratitude to Farid Hassani for designing and fabricating the transmon used in this work.

3.1 Introduction

Quantum phase transitions (QPTs), both first order and second order [Voj03], have been at the forefront of physics research for half a century. The original idea of QPTs as abrupt shifts

in the (pure) ground state of closed quantum systems as a function of a control parameter applied mostly to condensed matter physics. Dissipative quantum phase transitions (DPTs) occurring in the (in general, mixed) steady state of open quantum systems [CCF+05, DMK+08, NKSD10, DTM+10, KGI+12, LBOC13, MBBC18, HRP18, GJC18, RNHY20, SHA+21], however, broadened the scope of phase transitions to encompass mesoscopic systems and later even microscopic systems, where the interaction with the environment essentially affects the system dynamics. A DPT was first realized experimentally in a Bose-Einstein condensate interacting with a single-mode optical cavity field [BGBE10], and DPTs are increasingly relevant to today's quantum science and technology [VWIC09, FLP17b, FSL+17, GBK+20].

In view of this success, it is remarkable that in recent years yet another phase-transition paradigm could emerge, namely, first-order dissipative quantum phase transitions. A first-order phase transition means that two phases can coexist in a certain parameter region, such as water and ice at $0\,^{\circ}\mathrm{C}$ for a certain range of free energy. Coexistence of phases in the quantum steady state seems paradoxical, since the steady-state plus normalization conditions for the density operator constitute a linear system of equations that admits only a single solution. That is, given the Liouvillian superoperator \mathcal{L} for the Markovian evolution of the system, there exists only a single normalized density operator ρ_{st} that satisfies 1

$$\mathcal{L}\rho_{\mathsf{st}} = 0. \tag{3.1}$$

The resolution is that a single density operator can accommodate the mixture of two macroscopically distinct phases expressed as a ratio of the two components. In the water analogy, at 0° C we could symbolically write

$$\rho_{\mathsf{st}} = c \, \rho_{\mathsf{water}} + (1 - c) \, \rho_{\mathsf{ice}},\tag{3.2}$$

with c growing from 0 to 1 as the free energy is increased.

Recently, first-order dissipative quantum phase transitions have been found in various systems. One such platform is the clustering of Rydberg atoms described by Ising-type spin models [AOGL12, MLD+14, OMGW17, RDB18, SHP+21, MJYWX22] and realized experimentally [CRW+13, MVS+14, LTN+17]. Various other systems of ultracold atoms [LSHO16, FRMF+21] and dissipative Dicke-like models [GB18, SGKP20] also exhibit signatures of a first-order DPT. Other platforms include (arrays of) nonlinear photonic or polaritonic modes [LBOC13, CFC17, DMS17, RCS+17, Sav17, FSH+18, VMR+18, LCP20, LCB+22], exciton-polariton condensates [HEOL19, DKSanM21] and circuit QED [MTE+17, FSL+17, FDV+17, BTP+21, BMF+25]. In this work we observe and model the scaling and phase diagram of a first-order DPT in zero dimensions, i.e. for a single qubit strongly coupled to a single cavity mode.

3.2 Photon-Blockade breakdown

The Jaynes-Cummings (JC) model - one of the most important models in quantum science - describes the interaction between atoms and photons trapped in a cavity [HR06]. It is expressed by the Hamiltonian ($\hbar=1$)

$$H_{\text{JC}} = \omega_{\text{R}} a^{\dagger} a + \omega_{\text{A}} \sigma^{\dagger} \sigma + ig \left(a^{\dagger} \sigma - \sigma^{\dagger} a \right) + i\eta \left(a^{\dagger} e^{-i\omega t} - a e^{i\omega t} \right), \tag{3.3}$$

¹That is, barring special cases of reducible quantum dynamical semigroups, cf. D. Nigro, On the uniqueness of the steady-state solution of the Lindblad–Gorini–Kossakowski–Sudarshan equation, Journal of Statistical Mechanics: Theory and Experiment **2019**, 043202 (2019).

with $\omega_{\rm R}$ the angular frequency of the cavity mode with boson operator a, $\omega_{\rm A}$ the angular frequency of the atomic transition with operator σ , g the coupling strength, η the drive strength, and ω the angular frequency of the drive. This model yields the prototype of an anharmonic spectrum in the strong-coupling regime, as demonstrated in cavity QED [BSKM+96] and circuit QED [FGB+08], and with quantum dots in semiconductor microcavities [KRM+10]. Its strong anharmonicity at the single-photon level is the basis of the photon blockade effect [lbgSWD97, LBE+11], in analogy with Coulomb blockade in quantum dots or with polariton blockade [OKTT21]. Photon blockade means that an excitation cannot enter the JC system from a drive tuned in resonance with the bare resonator frequency, or similarly, a second excitation from a drive tuned to resonance with one of the single-excitation levels cannot enter the JC system.

This blockade is, however, not absolute, as it can be broken [Car15, DVD15, CBY $^+$ 21, CGB $^+$ 10, PSR $^+$ 12] by strong-enough driving due to a combination of multi-photon events and photon-number-increasing quantum jumps [VDFD19]. In an intermediary η range, in the time domain the system stochastically alternates between a blockaded, *dim state* without cavity photons and a *bright state* in which the blockade is broken and the system resides in the highly excited quasiharmonic part of the spectrum, resulting in a large transmission of drive photons. In phase space, this behavior results in a bimodal steady-state distribution

$$\rho_{\mathsf{st}} = c \,\rho_{\mathsf{bright}} + (1 - c) \,\rho_{\mathsf{dim}},\tag{3.4}$$

in analogy with Eq. (3.2), with c growing from 0 to 1 with increasing η . This effect has been demonstrated experimentally in a circuit QED system [FDV⁺17].

Bistability in the time domain or bimodality in phase space is, however, not sufficient evidence for a first-order phase transition. It is also necessary that the two constituents in the mixture Eq. (3.4) corresponding to the two states in the temporal bistable signal be macroscopically distinct as is the case in Eq. (3.2). It has been shown theoretically [Car15, VDFD19], that the photon blockade breakdown (PBB) effect has such a regime, i.e. a thermodynamic limit, where both the timescale and the amplitude of the bistable signal go to infinity, resulting in long-lived and macroscopically distinct dim and bright phases. Remarkably, this thermodynamic limit is a strong-coupling limit, defined as $g/\kappa \to \infty$, and is independent of the physical system size, i.e., the system remains the same JC system composed of two microscopic interacting subsystems. In this limit, the temporal bistability is replaced by hysteresis, where the state of the system is determined by its initial condition, since switching to the other state entails an infinite waiting time. The passage to the thermodynamic limit, i.e., the indefinite increase of g/κ has been termed "finite-size scaling" [VDFD19].

In this work, we demonstrate these additional criteria that clearly signify the observed physical effect as a first-order dissipative quantum phase transition. We demonstrate the finite-size scaling over 7 orders of magnitude towards the thermodynamic limit and extract the phase diagram of a first-oder DPT in zero dimensions. We realize this experiment with a superconducting qubit strongly coupled to a bandwidth-tunable microwave cavity mode and find qualitative agreement with large-scale Quantum-Jump Monte Carlo (QJMC) simulations and neoclassical calculations of the phase boundaries.

3.3 Experimental implementation

The schematic of experimental setup inside dilution fridge is shown in Figure 3.1

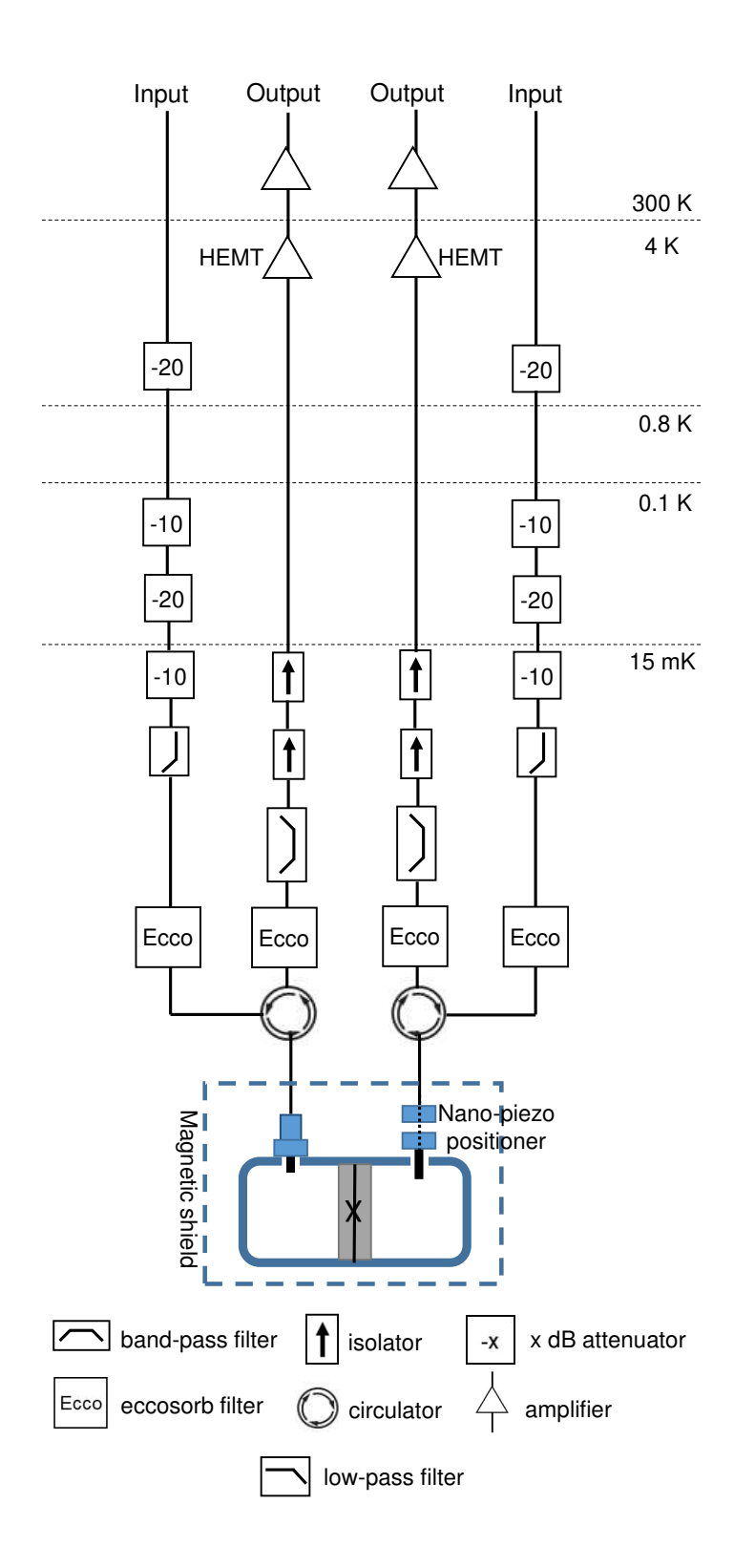


Figure 3.1: **Measurement setup.** Schematic of the wiring of the sample inside a Bluefors dilution refrigerator used for the experiment.

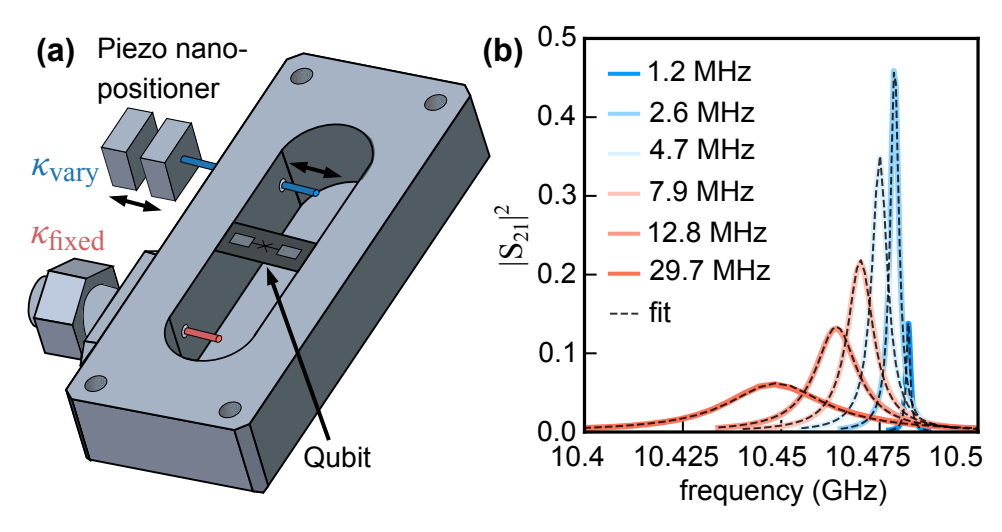


Figure 3.2: **Experimental realization.** (a) Schematics of the experimental device consisting of a superconducting transmon qubit fabricated on a silicon substrate that is placed at the antinode of the fundamental mode of a 3D copper cavity. The cavity has a fixed-length port (red) and an *in situ* variable-length pin coupler port (blue). (b) Measured cavity transmission spectra with the qubit far detuned for different coupler positions (color coded) together with a fit to Eq. (3.5) (dashed lines) and the extracted $\kappa/2\pi$.

Our experimental setting incorporates a transmon qubit [KYG+07, PSB+11] placed at the antinode of the standing wave of a 3D copper-cavity, as shown in Fig. 4.11(a), that can be flux-tuned by application of a magnetic field via a millimeter-sized superconducting bias coil mounted at the outside cavity wall. The transmon qubit has maximum Josephson energy $E_{\rm J,max}/h\approx 48\,{\rm GHz}$, charging energy $E_{\rm C}/h\approx 382\,{\rm MHz}$, and a resulting maximum transition frequency $\omega_{\rm A}/2\pi$ between its ground and first excited states of approximately $12.166\,{\rm GHz}$. When the transmon ground state to first excited state transition is tuned in resonance with the cavity mode at $\omega_{\rm R}/2\pi\approx 10.4725\,{\rm GHz}$, the directly measured coupling strength $g/2\pi$ between the single photon and the qubit transition is as high as $344\,{\rm MHz}$, which is about only a factor of 3 below the so-called ultrastrong-coupling regime [FDLR+19]. The relatively high absolute anharmonicity $\Delta_{\rm an}/h$ between subsequent transmon state transitions is approximately $-418\,{\rm MHz}$ at this flux bias position.

The cavity has two ports, of which the input pin coupler position is fixed with an external coupling strength $\kappa_{\rm fixed}/2\pi$ of approximately $500\,{\rm kHz}$. The output coupler is attached to a cryogenic piezoelectric nanopositioner, which allows adjustment of the pin length extending into the cavity [SPC+12]. With this tunable coupler, the coupling strength can be varied in situ in a wide range, $\kappa_{\rm vary}/2\pi\approx 20\,{\rm kHz}$ to $30\,{\rm MHz}$. The internal cavity loss at low temperature $\kappa_{\rm int}/2\pi$ is approximately $600\,{\rm kHz}$, which is achieved by electropolishing of the high-conductivity copper surface before cooldown to 10 mK in a dilution refrigerator.

All four scattering parameters are measured with a vector network analyzer to calibrate the measurement setup and the cavity properties when the qubit is far detuned from the cavity resonance. Figure 4.11(b) shows transmission measurements fitted with the scattering parameter S_{21} derived from the input-output theory of an open quantum system [GC85]:

$$S_{21} = \frac{\sqrt{\kappa_{\text{fixed}}\kappa_{\text{vary}}}}{\kappa/2 - i(\omega - \omega_{\text{R}})}.$$
(3.5)

From these fits, we extract all loss rates that add up to the total cavity linewidth $\kappa = \kappa_{\text{fixed}} + \kappa_{\text{vary}} + \kappa_{\text{int}}$, also indicated in Fig. 4.11(b).

Time-domain characterization measurements confirm that the qubit is Purcell limited and homogeneously broadened at the flux sweet spot [HSJ+08], where the measured energy relaxation time $T_1=1/\gamma_1\approx 0.5~\mu s$ and the coherence time $T_2=(\frac{\gamma_1}{2}+\gamma_\phi)^{-1}\approx 1~\mu s$, where γ_ϕ is the pure dephasing rate. When the qubit frequency is tuned far below the resonator frequency $\omega_A/2\pi\approx 6.083~\mathrm{GHz}$ by application of an external magnetic field, the measured coherence times are $T_1\approx 18.14~\mu s$ and $T_2\approx 0.496~\mu s$, which we attribute to a higher Purcell limit due to the larger detuning as well as drastically increased flux noise sensitivity. On resonance $\omega_A=\omega_R$, where the following experiments were performed, the energy relaxation is therefore fully dominated by cavity losses. The measured vacuum Rabi peak linewidth changes with and without the qubit in resonance are in agreement with a small amount of flux-noise-induced dephasing expected at this flux bias position.

3.4 Bimodality and characteristic timescales

The photon blockade and its breakdown (PBB) most straightforwardly occur when the two interacting constituents are resonant, i.e., $\omega_{\rm A}=\omega_{\rm R}$. In this and the next Section we furthermore consider the case of driving the system on resonance: $\omega=\omega_{\rm R}$. In contrast to the simplest case of a two-level atom [Car15, VDFD19], where this leads to a critical point, signifying a second-order DPT [Car15, CBY+21] (the so-called spontaneous dressed-state polarization [AC91, AMM09, DRT11]), in our experimental situation where at least three transmon levels are relevant, we still have bistability of the resonator intensity. In Ref. [FDV+17], an interpretation of this difference was given in terms of the spectrum of a three-level system strongly coupled to a harmonic-oscillator mode, which we summarize in Fig. 3.3(a). In Appendix B.2, we further elaborate on this difference in the frame of an approximate neoclassical theory extended to the three-level atom case.

For low input powers corresponding to less than a single intracavity photon on average, we observe a vacuum-Rabi-split spectrum in transmission, as shown in Fig. 3.3(a) and (b) (blue line). No transmission peak is observed at the bare cavity frequency $\omega_{\rm R}$ up to intermediate input drive strengths η . This means that a single photon - or even hundreds of photons at the chosen $g/\kappa=39.1$ - are prevented from entering the cavity due to the presence of a single artificial atom.

This blockade is observed to be broken abruptly by further increasing the applied drive strength η , which is proportional to the square root of the applied drive power and the corresponding drive photon number. As η is increased by only a finite amount close to the PBB, the transmitted output power increases by three orders of magnitude at the bare resonator frequency, as shown in the red spectrum in Fig. 3.3(b). The central sharp peak in the transmission spectrum corresponds to a time-averaged measurement (determined by the resolution bandwidth chosen) of a cavity that is fully transparent for most of the integration time. This PBB effect can be attributed to the nonlinearity of the lower part of the JC spectrum, which is strongly anharmonic [FGB+08, BCK+09], while the higher-lying part of the spectrum has subsets that are closely harmonic over a certain range of excitation numbers [FSS+10] and can hence accommodate a closely coherent state.

In the time domain, with η in the phase coexistence region, the PBB effect results in a bistable telegraph signal, where the system output alternates between a "dim" state, where the qubit-resonator system remains close to the vacuum state unable to absorb an excitation from the externally applied drive, and a "bright" state, where the system resides in an upper-lying, closely harmonic subset of the JC spectrum, cf. Fig. 3.3(c). The switches between these

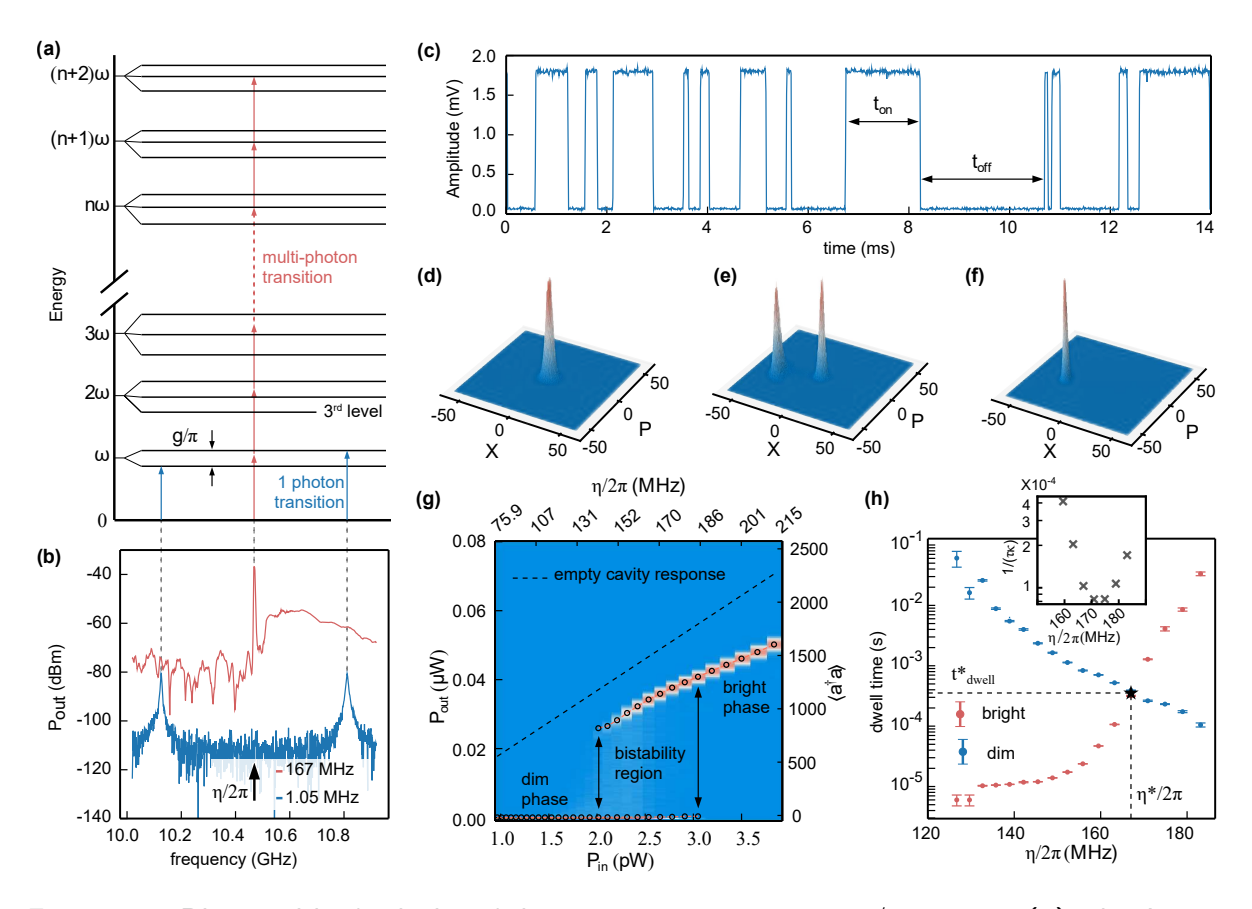


Figure 3.3: Photon blockade breakdown measurements at $g/\kappa \approx 39.1$. (a) The Jaynes-Cummings ladder for a three-level atom illustrating the PBB effect in the frequency domain: single-photon (blue) and multi-photon transitions (red) are indicated according to the measured spectrum at the Rabi-splitting frequencies and near resonance, respectively. As indicated, the third atomic state causes a third subladder in the spectrum starting from the second rung, whose spacing is close to the bare-system frequency. This is a possible explanation for the PBB bistability persisting in the case of resonant driving. (b) Measured cavity transmission spectra for $\omega_A = \omega_R$ for two applied external drive strengths: 1.05 MHz, revealing a typical vacuum Rabi spectrum, and $167.01\,\mathrm{MHz}$, where a sharp peak at ω_R is observed. (c) Measured cavity output bistability at $\omega = \omega_R$ in the time domain indicating the dwell times of the bright state (t_{on}) and the dim state (t_{off}) . (d)-(f) Measured quadrature histograms (proportional to cavity Q functions convolved with amplifier noise) for the dim phase at $\eta/2\pi=105\,\mathrm{MHz}$, for the bistable region with equal probability at $167\,\mathrm{MHz}$, and for the bright phase at $210\,\mathrm{MHz}$, respectively. (g) Measured histograms of the output power (arranged vertically and with probability color coded) as a function of input power. The maxima indicated by circles trace out a typical bistability curve, see Fig. 3.5(b). **(h)** Extracted average dwell times in the dim and bright states (Eq. (3.6)) as a function of η . The error bars represent the standard error that is extracted from five sections of the full dataset. The dwell time and drive strength corresponding to half-filling where $t_{
m dwell}^{
m dim}=t_{
m dwell}^{
m bright}$ are indicated with an asterisk. The inset shows the measured slow-switching eigenvalue $1/\tau$, from Eq. (3.7), in the unit of κ as a function of drive amplitude η close to half-filling [SC88].

two classical attractors are necessarily multiphoton events that are triggered by quantum fluctuations. This bistability was shown to be a finite-size precursor of what would be a first-order DPT in the thermodynamic limit $(g/\kappa \to \infty)$ [VDFD19], where the bistability develops into perfect hysteresis: the system is stuck in the attractor determined by the initial condition as long as the control parameters are set in the transition domain 2 .

To investigate this dynamics qualitatively, we record the real-time single-shot data of both quadratures of the transmitted output field at the bare cavity frequency while applying a continuous-wave (CW) drive tone resonant with the bare cavity over a range of applied drive strengths. The transmitted radiation is first amplified with a high-electron-mobility transistor (HEMT) at $4\,\mathrm{K}$ followed by a room-temperature low-noise amplifier (LNA), and then down-converted with an in-phase and quadrature mixer with appropriate intermediate frequency and finally digitized with a digitizer. This recorded data are then digitally low-pass filtered with appropriate resolution bandwidth and down-converted to 0 Hz to extract the time-dependent quadratures in voltage units. For example, in the case of $\kappa/2\pi=8\,\mathrm{MHz}$, the recorded data are $2.88\,\mathrm{s}$ long and the final time resolution of the extracted quadratures is $2.5\,\mathrm{\mu s}$; see Fig. 3.3(c). The selection of an appropriate resolution bandwidth is critical for a number of reasons: (1) to successfully resolve frequent and sudden switching events caused by very short dwell times at high κ values, (2) to maintain a signal-to-noise ratio that allows one to clearly discriminate single-shot measurement events without averaging, and (3) to achieve a sufficient total measurement time to resolve long dwell times with the available memory.

From the resulting histograms in phase space, [see Fig. 3.3(d-f), which represent the scaled Husimi Q functions convolved with the added amplification chain noise photon number $n_{\rm amp}\approx 9.2$], it can be deduced that for low drive strength the photon blockade is intact (dim phase) with the Q function being centered at the vacuum state. When the input drive strength is increased, the Q function becomes bimodal with decreasing weight of the dim state as described in Eq. 3.4. At high-enough η , only the bright coherent state is measured. Note that the transformation of the Q-function and hence the steady-state density operator of the system as a function of η is continuous, yet a first-order phase transition with a well-defined coexistence region can occur.

A similar conclusion can be drawn from the output power histograms (color map) that trace out a typical bistability curve as shown in Fig. 3.3(g). The most likely output powers P_{out} and calculated equivalent intra-cavity photon numbers of the empty cavity driven on resonance $\bar{n}_{\text{cav}} = \frac{P_{\text{in}}}{\hbar \omega_{\text{R}}} \frac{4\kappa_{\text{fixed}}}{\kappa^2}$ as a function of applied input power P_{in} and resulting drive strength $\eta = \sqrt{\bar{n}_{\text{cav}}} \kappa/2$ are marked with circles. The vacuum, bistability, and bright regions are well defined. We find that the derivative of the bright solution obtained at high P_{in} deviates somewhat from the empty-cavity response measured when the qubit is far detuned (dashed line). For large g/κ values, this is more pronounced and we have observed that this can lead to secondary bistability regions at even higher powers for $g/\kappa \gtrsim 43$, which we believe to originate from the multilevel nature of the transmon qubit. In this work, we focus only on the bistability occurring at the lowest drive strength.

 $^{^2}$ Note that a measurement of the bistable signal in the time domain gives additional information compared to observing the hysteresis cycle by sweeping a parameter of the drive (amplitude or detuning, cf. Fig. 3.3 (g) and Fig. 3.5(c)). This is because the former also tells us about the timescale on which we can expect the hysteresis to manifest. If we sweep the drive amplitude over the bistability domain faster than the dwell time, then we observe perfect hysteresis. However, the sweep should not be too fast, in order to avoid provoking a switch between the attractors, that can be expected by non-adiabatic changes of parameters. In contrast, if the timescale of the sweep is slower than the dwell time, we would observe several switches between the attractors while sweeping over the bistability domain.

In Fig. 3.3(h) we show the measured dwell times of dim and bright states as a function of input power. The average dwell times at each input power are calculated as

$$t_{\text{dwell}}^{\text{dim}} = \frac{1}{N} \sum_{n=1}^{N} t_{\text{off},n}; \quad t_{\text{dwell}}^{\text{bright}} = \frac{1}{N} \sum_{n=1}^{N} t_{\text{on},n};$$

$$(3.6)$$

and the threshold for one of the N switching events during the full measurement duration (with 2.5 μs resolution) is defined at half of the observed full amplitude for the lowest applied $\eta/(2\pi)\approx 140\,\mathrm{MHz}$ where the bistability is fully developed. Note that in cases of low signal to noise ratio, e.g. for large κ or at high drive detunings shown later, we used a higher threshold that at least exceeds the variance of the output power of the dim state.

At low η there are only few switching events because the system remains in the dim state for long time scales. As η is increased to $\eta^*/(2\pi)\approx 167\,\mathrm{MHz}$ the measured average dwell times cross at $t_\mathrm{dwell}^\mathrm{dim}=t_\mathrm{dwell}^\mathrm{bright}=t_\mathrm{dwell}^*\approx 354\,\mu\mathrm{s}$. We call this the "half-filling point" where it is equally likely for the system to be found in the dim state or the bright state, denoted by an asterisk in Fig. 3.3(h). For even higher drive strength, the system prefers to dwell in the bright state, i.e., we observe close to full resonator transmission for most of the time.

Finally, to complete the study of the breakdown process through the bistable cavity transmission, we define the overall characteristic timescale of the system as

$$\tau = ((t_{\text{dwell}}^{\text{dim}})^{-1} + (t_{\text{dwell}}^{\text{bright}})^{-1})^{-1}, \tag{3.7}$$

see Table 1 in Ref. [VDFD19], since it governs the rate with which the system evolves into the appropriate steady-state mixture of the two attractors from an arbitrary initial state. This is the slowest characteristic timescale in the system that diverges in the thermodynamic limit. The unit-less slow-switching eigenvalue of the time evolution of the system is the inverse of this characteristic timescale, $\lambda=1/(\tau\kappa)$, whose dependence on η can be seen in the inset in Fig. 3.3(h). It shows the minimum $\lambda\ll 1$ close to the half-filling point in agreement with the predicted "slowing down" of the system dynamics [SC88].

3.5 Finite size scaling towards the thermodynamic limit

In the context of first-order DPTs, "macroscopic behavior" can be defined independently of experimental characteristics such as the signal-to-noise ratio, or the resolution of a "macroscopic" detector. Rather, it is the concept of a thermodynamic limit that distinguishes a first-order DPT from temporal bistability. Whereas normally the thermodynamic limit of phase transitions is reached by increasing the system size (e.g., the number of particles), in the case of the PBB, it depends on the dynamical parameter g/κ . Moving towards the thermodynamic limit $g/\kappa \to \infty$ has been termed "finite-size scaling" [VDFD19], along which a temporal bistability becomes a first order DPT with attractors of increasingly distinct intensity and dwell time, eventually leading to perfect hysteresis. In this limit, the initial state of the system determines which of the two possible coexisting states it will be frozen into.

While, in principle, the distinction between bright and dim attractors in terms of intensity and dwell time go to infinity in the thermodynamic limit, the drive power necessary to reach the bistability region is also expected to go to infinity. In the experiment, this would at some point put the system into an invalid state, e.g., by breaking the superconductivity of the transmon qubit. Nevertheless, in the present case, we demonstrate the predicted finite-size scaling over many orders of magnitude both in the dwell time and in intensity. With this we

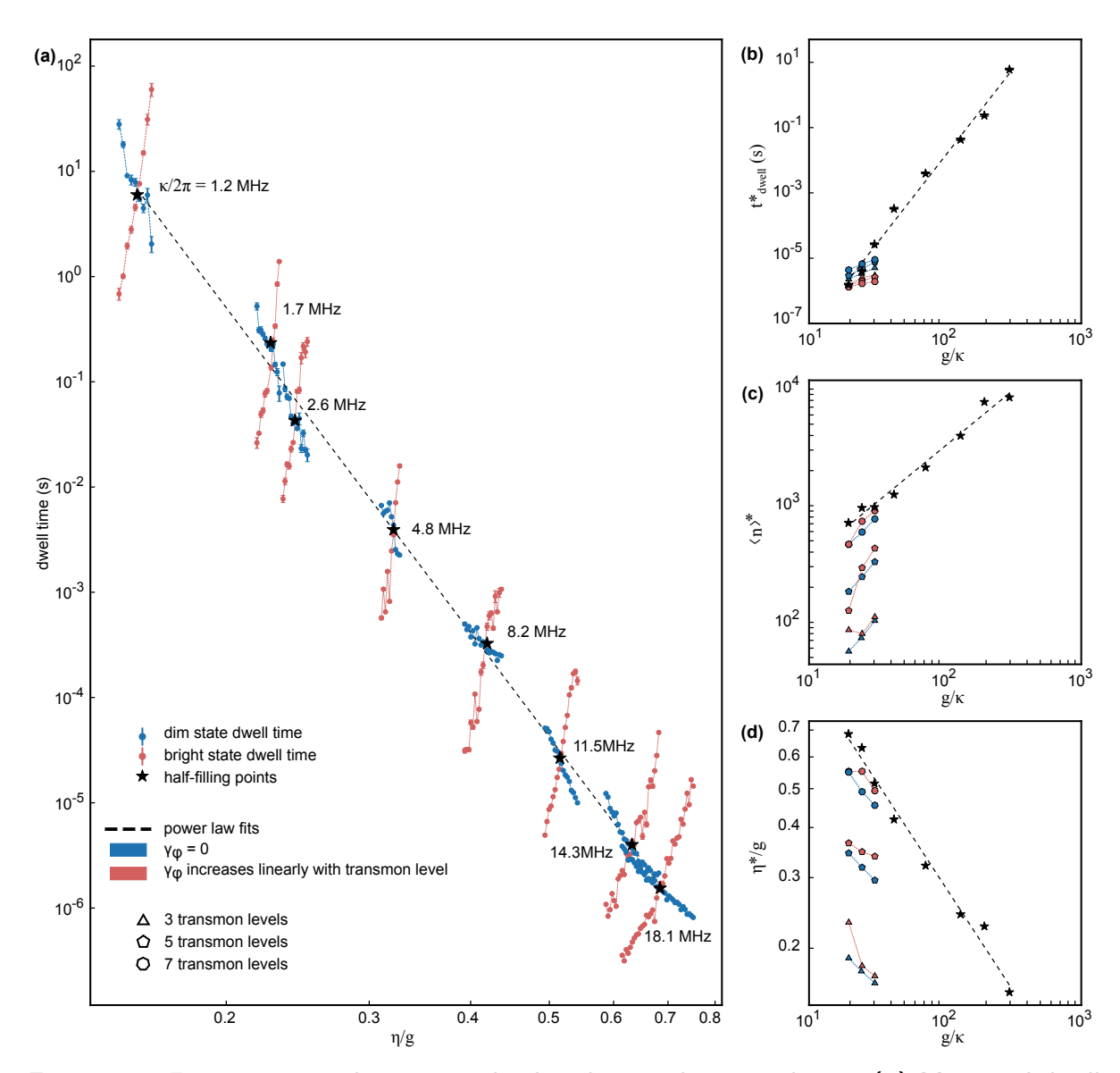


Figure 3.4: Finite size scaling towards the thermodynamic limit. (a) Measured dwell times in the dim state (blue) and the bright state (red) are shown as a function of η/g for different values of κ . Black stars denote half-filling values, where the probabilities of being in the dim state or bright state are equal. The dashed line is a power law fit. The error bars represent the standard error that is extracted from at least three sections of the full dataset. (b)-(d) Measured scaling laws as a function of control parameter g/κ at half filling (asterisks). Fitting the experimental data (dashed lines) yields the exponents $t_{\rm dwell}^* \propto (g/\kappa)^{5.4\pm0.2}$ for the dwell time, $\langle n\rangle^* \propto (g/\kappa)^{0.96\pm0.05}$ for the average resonator photon number, and $\eta^*/g \propto (g/\kappa)^{-0.52\pm0.03}$ for the input drive strength. We compare the experimental values (stars) with those obtained from QJMC simulations (polygons with color code) for computationally manageable $\kappa=11.5,\ 14.3,\$ and $18.1\$ MHz. The simulations include three, five, or seven transmon levels both without transmon dephasing (light blue) and with dephasing increasing linearly with the level number (light red) with $\gamma_{\phi,1}/(2\pi)=50\,$ kHz and $\gamma_1=0.$ Details of the simulation are given in the main text and in Appendix B.1.

show - despite the underlying microscopic nature of the system - a truly macroscopic behavior. We also experimentally determine the finite-size scaling exponents of the characteristic time, corresponding drive strength and intracavity photon number for this DPT.

In Fig. 3.4(a) we show the measured dwell times as a function of drive strength - similar to Fig. 3.3(h) - for different $\kappa/2\pi$ values ranging from $1.21\,\mathrm{MHz}$ to $18.1\,\mathrm{MHz}$. For each κ value the dwell time in the dim state (blue symbols) decreases with increasing drive strength and that of the bright state (red symbols) increases until eventually the system is fully stabilized in the bright state. For each g/κ value, we define a single characteristic time of the process t^*_{dwell} at the drive strength η^* that leads to half-filling of the telegraph signal; see also Fig. 3.3(h).

Remarkably, for the largest realized value of g/κ (i.e., 287), the characteristic dwell time $t_{\rm dwell}^*$ reaches approximately $6\,\rm s$. This exceeds the characteristic microscopic dissipation times of order κ^{-1} and T_2 by a factor of more than approximately 10^6 and is reminiscent of the emergence of two macroscopically distinct states with strongly suppressed transitions that require a cascade of quantum jumps [VDFD19]. This strong-coupling, high photon number limit where the effect of quantum fluctuations vanishes has been defined as the thermodynamic limit of such a finite-size zero-dimensional system [Car15].

Finite-size scaling also requires that the characteristic timescale and brightness scale as a function of g/κ , while the system remains self-similar, which in this case means that it keeps switching stochastically at a fixed filling factor. In Fig. 3.4(b) we plot the measured increase of t^*_{dwell} at filling 0.5 over a range of seven orders of magnitude as a function of g/κ . The behavior follows a strong power law over the full range, and the fitted finite-size scaling exponent is $t^*_{\text{dwell}} \propto (g/\kappa)^{5.4\pm0.2}$. Similarly, the intracavity photon number of the bright state at half-filling increases nearly linearly with $\langle n \rangle^* \propto (g/\kappa)^{0.96\pm0.05}$, as shown in Fig. 3.4(c), and as a consequence the corresponding drive strength decreases with the square root, $\eta^*/g \propto (g/\kappa)^{-0.52\pm0.03}$, as shown in Fig. 3.4(d). Here the normalization of the drive amplitude with g is motivated by the two-level neoclassical theory, where the critical point appears at $\eta/g=0.5$ for $\Delta=0$.

The theoretical results (triangles, pentagons and heptagons) shown in Fig. 3.4(b)-(d) are taken from large-scale numerical simulations performed with C++QED, a framework for simulating open quantum dynamics [Vuk12]. An adaptive version of the QJMC method is applied, where a single stochastic quantum trajectory is considered to correspond to a single experimental run [KV19]. The shown data are based on 64 CPU years of simulation time with a Hilbert space dimension of up to approximately 2^{15} (7 transmon levels and 3-5 times $\langle n \rangle^*$). Another computationally demanding aspect is that the required time step is set by the largest characteristic frequency (typically g or η) of the microscopic system (sampled with $1/\kappa$ to reduce data volume), whereas the total trajectory needs to cover many times $t_{\rm dwell}$ to obtain sufficient statistics of the macroscopic behavior. Together this limits the range of numerically accessible g/κ values to the lowest three values measured. For more details on how we model the system, examples of simulated quantum trajectories and the impact of different transmon dephasing models, see Appendix B.1.

The observed photon number scaling exponent is about half of the analytical prediction of $\langle n \rangle^* \propto (g/\kappa)^2$; see Eq. (6) in Ref. [VDFD19]. This is not surprising since the two-level neoclassical theory does not yield quantitative agreement for the case with a multilevel transmon circuit. Numerical simulations for the lowest three g/κ values taking into account up to seven transmon levels (heptagons in Fig. 3.4(c)), agree with the measured linear exponent to within 15%. The absolute value of $\langle n \rangle^*$ also agrees well (blue) and is further improved when we include qubit dephasing of all transmon levels (red) due to flux noise with the measured

 $\gamma_\phi/2\pi \approx 50$ kHz for the lowest qubit transition. That is, as long as enough transmon levels are taken into account. In the case of just three transmon levels, the simulated value is about an order of magnitude smaller than the measured value. This highlights the importance and participation of multiple transmon levels in the dynamics of the system.

The dwell times and scaling shown in Fig. 3.4(b) are more robust with regard to the number of transmon levels but we observe a substantial deviation between the measured (5.4) and simulated scaling exponents in the range of 0.9-2.2. In [VDFD19], on the basis of a two-level model with finite detuning, the blink-off rate could be calculated from the rate of ladder-switching quantum jumps, and was found to be proportional to $\kappa/\langle n \rangle^*$, so the waiting time for a blink-off is $\langle n \rangle^*/\kappa$, therefore, it scales as g^2/κ^3 . The numerically determined timescale-exponent in the same work was $(\kappa t^*_{\rm dwell}) \propto (g/\kappa)^{2.2}$, which is very close to the analytical value.

The observed scaling exponent is significantly larger, which may be due to ultrastrong-coupling effects kicking in earlier than commonly expected, such as the counter-rotating terms not taken into account in the numerical simulations (for a numerical treatment of the Bloch-Siegert shift, see [PDK $^+$ 18]) and the hybridization of decay channels [BP07, BGB11], which can invalidate our approach of using separate transmon and resonator decay channels in the master equation. Other potentially participating mechanisms could include transmon ionization [SPC $^+$ 22] or dielectric surface loss saturation [ZRP $^+$ 23] that might further stabilize the system - in particular in the bright attractor - and thus reduce the blink-off probability. Taken together, these effects appear to be driving the system significantly faster to the thermodynamic limit compared with what would be expected from the standard Jaynes-Cummings model.

Importantly and irrespective of the origin of the unexpectedly strong scaling, we observe that the system is always able to relax to the vacuum state eventually - despite the continuous driving. This vacuum state is then stabilized for seconds by the presence of a single qubit, even for the highest drive strength corresponding to a photon number of $\langle n \rangle$ approximately 10^4 . In contrast to similarly looking fluorescence signals with dwell times on the order of seconds, which have been known in quantum science since the first electron-shelving experiments with single ions in Penning traps [NSD86, BHIW86] due to long-lived metastable atomic states, in the present case the measured timescale exceeds all microscopic timescales by many orders of magnitude, i.e., the system is very deep in the macroscopic limit, which justifies its classification as a phase transition in a microscopic quantum system.

3.6 Phase Diagram

The PBB phase transition has been predicted to exhibit an interesting phase diagram as a function of drive detuning $\Delta \equiv \omega - \omega_{\rm R} = \omega - \omega_{\rm A}$. From the neoclassical equations, valid for pure two-level qubit states and $\gamma_1 = \gamma_\phi = 0$ [KNV23], the bistable region is expected only at finite detunings away from the critical point at $\Delta = 0$ [Car15, VDFD19]. This model can be extended with a third atomic level to provide a more realistic description of the transmon. For the extension, the population of the third level must be neglected, while we keep the coherences between all levels (for details, see Appendix B.2), which is a reasonable approximation given the anharmonicity of the transmon. Solutions to these models are shown in Fig. 3.5(a) and Fig. 3.5(b) for a two-level transmon and a three-level transmon, respectively. In the latter case, because of the very high order polynomials appearing in the solution, it is impractical to extract the full phase diagram; therefore, the multistable transmission curves are qualitatively different: the latter shows an asymmetry with respect to the $\Delta = 0$ point as well as multistability

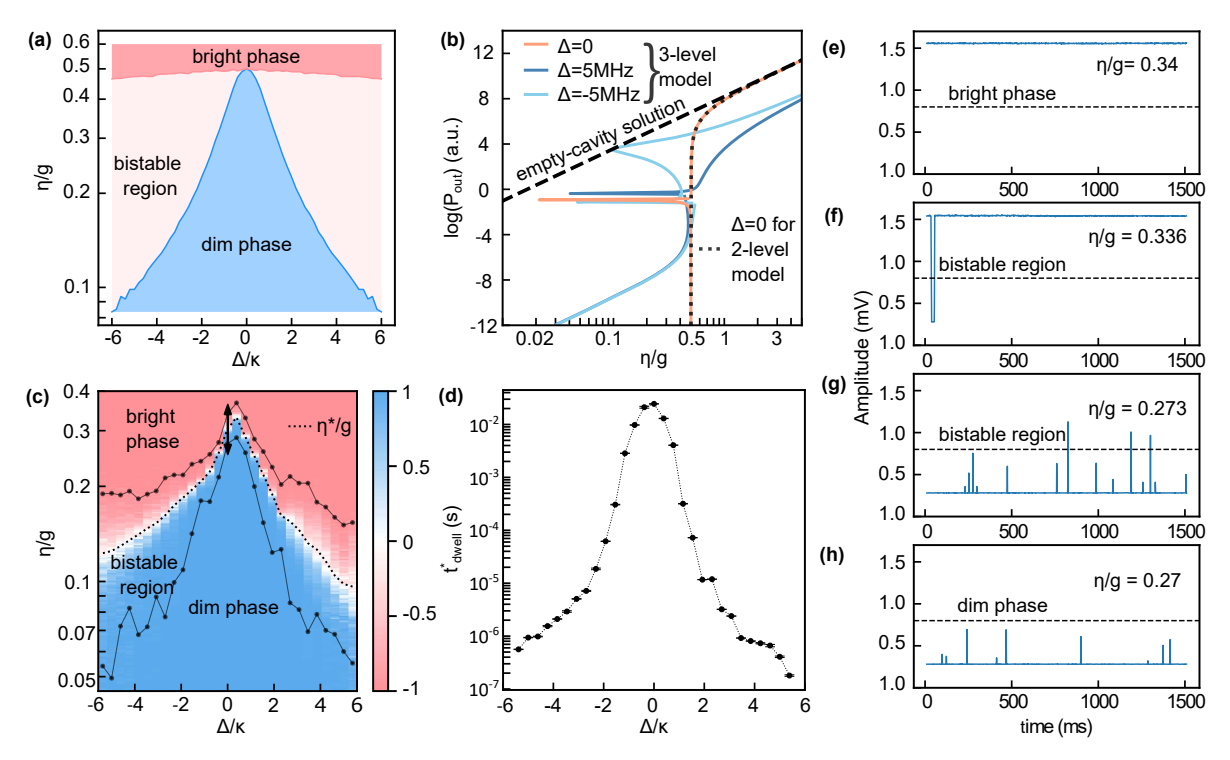


Figure 3.5: The photon blockade breakdown phase diagram. (a) Phase diagram on the $\Delta - \eta$ plane obtained from the neoclassical theory for two transmon levels. (b) Typical multistability curves for the transmitted intensity as a function of the drive amplitude obtained from the approximate three-level neoclassical theory detailed in Appendix B.2. The curves are different for $\Delta = 5\,\mathrm{MHz}$ and $\Delta = -5\,\mathrm{MHz}$ proving the asymmetry of the phase boundaries. For $\Delta=0$, the curve obtained from the two-level theory is plotted as a dotted line for comparison, revealing the role of the third level in the appearance of a bistability on resonance. The solution of the three-level theory contains very high order polynomials that lead to numerical problems when the experimental parameters are used. Therefore, here and in (a), model parameters were used: $g_1/\kappa = 30$, $g_2/\kappa = 2.5$, $\Delta_{an}/\kappa = -40$ (see Appendix B.1 for the definition of all the parameters of the full model). (c) Experimental PBB phase diagram at $g/\kappa \approx 132$ with boundaries (points) and the half-filling drive strength (dotted line) obtained from the experimental trajectories that exhibit the temporal bistable signal [(e)-(h)]. The color scale of the density plot depicts the ratio $r=(h_1-h_2)/(h_1+h_2)$, where h_1 and h_2 are the amplitudes of the peaks of the measured quadrature histograms corresponding to the dim and bright states, respectively, see Fig. 3.3(d-f). (d) Measured dwell times at half-filling as a function of drive detuning. Error bars are extracted from the mean and standard error of the measured dim and bright dwell times. (e)-(h) Experimentally observed telegraph signals that define the phase boundaries at different η values at $\Delta=0$ in the range of $\eta/2\pi$ from 85.6 to 115.5 MHz as indicated by a double arrow in (c).

for negative detunings - this has not been observed experimentally. Importantly though, the three-level model predicts bistability on resonance (orange line), while the two-level model does not (dashed line).

Experimentally we choose a large g/κ approximately 132.3, where the timescales are long and the phases are very well defined, to extract the phase diagram as a function of Δ . We sweep the drive strength for each chosen detuning and record a trace of time-domain single-shot transmission data for each parameter combination. The results are shown in Fig. 3.5(c) and

Fig. 3.5(d), which depict the three regions traced out on the $\Delta - \eta$ parameter plane and the measured dwell time at half filling (dotted lines), respectively.

The color scale in Fig. 3.5(c) is obtained from the relative weight of the phase space distribution, while the phase boundaries (points) are obtained from measured time-domain single-shot telegraph transmission data as shown in Fig. 3.5(e) - Fig. 3.5(h) for the range of η at $\Delta=0$ indicated in Fig. 3.5(a) with a double arrow. Here we define a threshold (dashed line) as described earlier and monitor if a single phase-switching attempt was successful in crossing this threshold within the measurement time. If the answer is yes, the corresponding η and Δ value pair is assigned to the bistable region boundary. If the answer is no, depending on the measured value (below or above threshold), the parameter combination is assigned to the dim phase or the bright phase. The parameter region where multiple crossings occur is assigned to the bistable region. For each detuning, the detection bandwidth and total measurement time have been optimized for us to be able to determine a sharp phase boundary and to resolve the dwell time over 5 orders of magnitude, as shown in Fig. 3.5(d).

The raw data in Fig. 3.5(e) - Fig. 3.5(h) reveal an interesting difference between partial phase-switching attempts from the dim state, which are quite frequent, and from the bright state, which are rather rare and typically of smaller amplitude (not visible in this data). This asymmetry is not observed in the simulated quantum-jump trajectories as shown, for example, in Fig. B.1, and its origin is not clear. However, these data point at an additional stabilization mechanism of the bright phase that might also contribute to the stronger-than-expected scaling towards the thermodynamic limit.

Comparing the theoretical and experimental phase diagrams Fig. 3.5(a) - Fig. 3.5(c), one can see that the two-level neoclassical model, while reproducing the overall resonance-like dependence on the detuning, fails to capture some of the essential features of the experiment. The three-level theory amends these qualitative differences: (i) While the two-level theory can be exactly shown to be independent of the sign of Δ , the three-level theory introduces an asymmetry due to the detuning $\Delta_{\rm an}$ of the third level. (ii) Crucially, the three-level theory exhibits a finite bistability interval on resonance, $\Delta=0$. This comparison underlines the role of the higher-lying transmon levels in shaping the experimental phase diagram, whereas the $g/\kappa \to \infty$ thermodynamic limit is robust with regard to the variation in the number of levels as shown by our simulation results above.

3.7 Discussion, conclusions and outlook

It is important to distinguish the presented PBB phase transition and scaling from several related phenomena. The oldest known such effect is optical bistability, dispersive or absorptive, which is itself a first-order DPT [DW80, CSLBC16, CFC17]. In the case of the PBB, we are not in the dispersive regime, however. The driving is close to or on resonance with the bare frequencies of the resonator and the transmon, and the decay of the latter does not play an essential role either [VDFD19]. Another related model is the Duffing oscillator that appears in a circuit QED context as a Kerr-nonlinear mode (the transmon) interacting with a linear mode (the resonator) [RacTM09, PT10]. Parametric driving can lead to critical behavior [WS19], and driven nonlinear inductors have exhibited slow classical switching events triggered by low-frequency thermal fluctuations on the order of seconds [MGM+18]. Long bit flip times up to 100 s have also been observed in a two-photon dissipative oscillator that is characterized by symmetry breaking of the intracavity field phase, but this system does not exhibit a bistability in the photon number [BMR+22]. In this respect, the transmon, even with

many levels considered, is algebraically very different from a nonlinear oscillator when it comes to jump operators because these are not bosonic. This results in an essential difference, as verified by our quantum simulations, where it is possible to try the consequences of different algebras. Our simulations clearly rule out the Duffing oscillator model [Dyk12], which cannot reproduce the phenomenology of the experiment since its bistable behavior reminiscent of dispersive optical bistability occurs for different parameters and does not exhibit the same scaling towards the thermodynamic limit ³. Finally, with respect to other recently discovered QPTs and DPTs in the Jaynes-Cummings model or Rabi model [HPP15, HP16, LI17, HRP18], where thermodynamic limits can also be defined in an abstract way, the difference of PBB as first-order DPT is that the thermodynamic limit is a strong-coupling limit. The well-resolved discrete spectrum of an interacting bipartite quantum system is essential for the effect.

In this paper, we have experimentally followed the finite-size scaling towards the $g/\kappa \to \infty$ thermodynamic limit with a characteristic time scale ranging over nearly seven orders of magnitude. Just like with a finite-size (nonmacroscopic) sample of water, at $0\,^{\circ}\mathrm{C}$ there is a contest of several metastable and even unstable states instead of true phases of liquid and ice [TFHE⁺19], in the PBB bistability for any finite value of g, there is a contest of nonmacroscopically distinct dim and bright states. We have experimentally determined the finite-size scaling exponent of the bistable switching timescale of approximately 5.4 ± 0.2 as well as the scaling exponent of the intracavity photon number of the bright state of approximately 0.95 ± 0.05 . We have also experimentally determined the phase diagram of the PBB phase transition and found that the characteristic dwell times drop by orders of magnitude for finite drive detunings.

We have compared these experimental results with large-scale quantum simulations based on the QJMC method considering different numbers of transmon levels (three, five and seven) and different dephasing models of higher-lying levels. This comparison indicates that transmon levels up to at least seven play an important role in the dynamics, as does the dephasing, since simulations with dephasing, e.g., due to flux noise, have shown better correspondence to the experimental data. Similarly, the comparison with neoclassical phase diagrams has also underlined the important role of higher transmon levels. The strong-coupling thermodynamic limit is, however, robust with regard to the involvement of the higher-lying states.

While the full quantum simulations reproduce the observed trends correctly, there are significant differences from the experiment in the measured dwell times, which might indicate the presence of further stabilization mechanisms - in particular in the bright attractor - and calls for improved methods to model such strongly coupled multilevel systems.

Even though the computational resources were substantial, the fully quantum numerical simulations were suitable only for modelling the three lowest coupling strengths g/κ investigated. This highlights the need for powerful quantum simulators even in the case of comparably simple circuits and, in particular, to explain how macroscopic phases can be stabilized by individual quantum systems. It is quite surprising that a single transmon qubit can switch back from the bright state - characterized by up to 10^4 intracavity photons - all the way to the dim state

 $^{^3}$ It is straightforward to show that in a mean-field treatment of a linear oscillator (the resonator) coupled to a Duffing oscillator (the transmon), the former can be eliminated from the dynamics, leading to a single Duffing oscillator with rescaled parameters but with the Kerr term unaffected. This shows that the nonlinearity of the model is independent of the coupling strength, in sharp contrast to the PBB, where the nonlinearity increases with g, which is the basis of the strong coupling thermodynamic limit. See also Chen, Qi-Ming, et al. Quantum behavior of the Duffing oscillator at the dissipative phase transition. Nature Communications 14, 2896 (2023).

and stabilize the empty cavity for seconds in the presence of the continuous large-amplitude coherent input field - in particular given its limited potential confinement [SPC^+22]. In the future, a fully confined qubit [HPK^+23] with higher power handling, or larger anharmonicity and superconducting cavities with lower loss could help to explore even more macroscopic phases, pushing the characteristic switching timescales from seconds to days.

Besides its fundamental interest as a quantum-classical phase transition, the PBB bistability also promises a few applications. Since single quantum jumps were shown to trigger the switching from the (nonclassical) dim state to the (closely classical) bright state [VDFD19], our system may be considered as a quantum-jump amplifier, where ultimately a macroscopic microwave device (outside the fridge) is getting switched by microscopic quantum events (inside the fridge). An interesting prospect is the control of the switching behavior, which can be envisaged in a parametric way, but preferably with another strongly coupled quantum system. In the latter case, the bistability could act as a quantum readout device with high signal-to-noise ratio. The capability of preparing the system on the verge of a phase-switching event could therefore make it applicable in quantum metrology and sensing based on microwave photon counting [GE09, PWP+24], a new paradigm for the application of first-order DPTs [FLP17a, RWW18, YJ19, HBZC19, DCMP+23].

The data and code used to produce the figures in this chapter are available online https://doi.org/10.5281/zenodo.10518321.

Quantum Illumination

Contributions and collaborations

The work presented in this chapter is a follow-up to the study reported in [BPVF20]. I would like to express my sincere gratitude to Andrea Trioni for redoing the wirebonding of the JPC chips on the PCB inside the package, which was essential for the success of these experiments. I am deeply thankful to Shabir Barzanjeh for his continuous support and guidance throughout this project—ranging from theoretical insights and numerical simulations to technical improvements across the board. I am also grateful to Joan Agusti and Peter Rabl for helping deepen my understanding of the experiments through valuable discussions and numerical support. Alejandro Juanes assisted me during the measurement phase, while Isabel Carnoto contributed significantly to the numerical modeling of Quantum Illumination, helping to bring the simulation closer to realistic conditions. Additionally, Clemens UIm played a key role in demonstrating phase conjugation using the Josephson Parametric Converter (JPC), which was an important step in this work. I would also like to thank Liu Qiu for many insightful discussions on two-mode squeezing and for exploring future directions, especially toward pulsed experimental schemes.

4.1 Background

Quantum entanglement is a cornerstone of quantum information science, enabling advancements in computation, communication, and sensing beyond classical limitations. One of its most promising applications is Quantum Illumination (QI), a target detection scheme designed to function in entanglement-breaking, high-noise environments. First proposed by Lloyd[Llo08, SL09], QI exploits quantum correlations to enhance detection performance compared to classical methods.

Later [TEG⁺08] compared the coherent-state (CS) illumination and the quantum illumination (QI) with Gaussian state as illustrated in Fig. 4.1, for the task of detecting a weakly-reflecting object ($\eta << 1$) embedded in a noisy environment with high background photon number ($N_B >> 1$). In CS illumination, as shown in Fig. 4.1(a), the source sends pulses prepared in coherent states, each with an average photon number $N_S << 1$, over M=TW >> 1, independent temporal modes, where T is pulse duration and W is bandwidth — resulting in a total mean photon number of MN_S . In contrast, as shown in Fig. 4.1(b), QI employs a source of entangled signal-idler pulses, such as those produced by continuous spontaneous

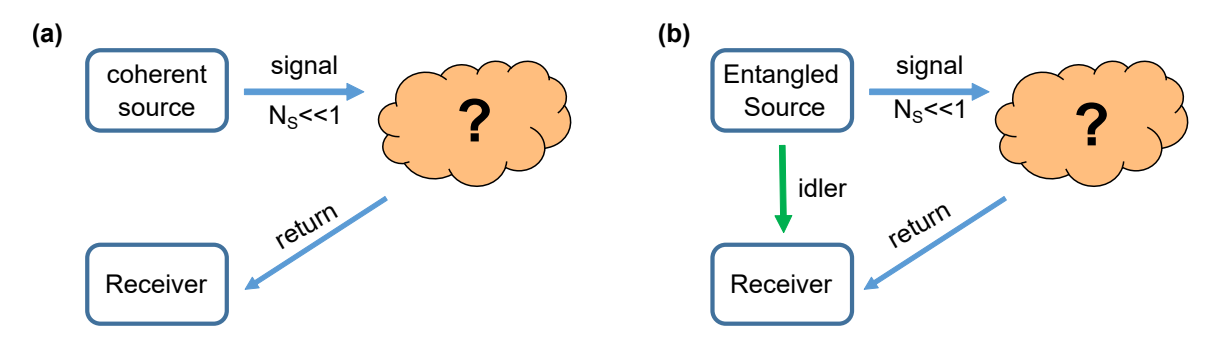


Figure 4.1: Lloyd's idea [Llo08] of detecting a weakly reflecting target in presence of background noise with (a) coherent state light and (b) entangled lights.

parametric down-conversion (SPDC). These pairs span M temporal modes, with the same average photon number $N_S << 1$ per mode. While the entanglement between signal and idler is typically destroyed due to interaction with the noisy environment, the key feature of QI is that the residual correlations between the retained idler and the received (potentially target-reflected) signal still persist and can be exploited for detection. [TEG+08] showed that the probability of error in detecting the target with CS illumination is bounded by,

$$\Pr(e)_{CS} \le e^{-M\eta N_S/4N_B}/2 = e^{-M \times SNR_{CS}}/2$$
 (4.1)

and that with QI is bounded by,

$$\Pr(e)_{QI} \le e^{-M\eta N_S/N_B}/2 = e^{-M \times SNR_{QI}}/2$$
 (4.2)

with ${\rm SNR_{CS}}=\eta N_S/4N_B$ and ${\rm SNR_{QI}}=\eta N_S/N_B$ being the error-exponents for CS illumination and QI respectively. Notably, QI provides a performance advantage over CS illumination — achieving up to a factor of 4 improvement in the SNR for the same total transmitted photon number.

Despite its theoretical promise, practical implementations of QI remain challenging, particularly in achieving the predicted signal-to-noise ratio (SNR) enhancement. To address this, Guha and Erkmen [GE09] proposed two optimal QI receivers for Gaussian states: the optical parametric amplifier (OPA) receiver and the phase conjugator (PC) receiver, both of which offer potential SNR gains of up to 3 dB. Since our experiment employs the PC receiver, this chapter will primarily focus on its implementation.

4.2 State of the art of QI experiments

The experimental realization of QI has been a growing research focus, particularly in high-noise environments where it holds potential for radar and imaging applications. Comprehensive overviews of QI's theoretical foundations and experimental developments can be found in [Sha20, KFSP24]. While initial demonstrations took place in the optical domain, recent efforts have shifted toward the microwave regime, where QI could offer a significant advantage over classical detection techniques.

The first experimental validation of QI was conducted by [LRBD+13], who used photon-number correlations to detect a target. However, this work did not compare QI performance against the

best classical detection methods, leaving its practical benefit unclear. A major advancement came with [ZMWS15], who demonstrated the first measurable QI advantage—achieving up to 0.8 dB SNR improvement—using an OPA receiver.

As interest in microwave QI grew, researchers explored various theoretical refinements, including optomechanical implementations [BGW $^+$ 15], non-Gaussian quantum states [SLHGR $^+$ 17], alternative entangled sources [CVB $^+$ 19], and hetero-homodyne detection strategies [RZSDC23]. These developments laid the groundwork for experimental efforts to transition QI from optics to microwaves.

The first microwave QI demonstration was performed by [LBSC+18, LDB+19] using a Josephson Parametric Amplifier (JPA), showing improved target detection sensitivity with entangled light. In 2020, [BPVF20] experimentally demonstrated microwave QI using a digital phaseconjugator receiver to detect a room-temperature object in free space. Entangled microwave signal-idler pairs were generated via a Josephson parametric converter (JPC), with the signal transmitted toward the target at the room temperature and the idler retained for subsequent joint measurement. The receiver employed heterodyne detection on both the reflected signal and the stored idler, allowing simultaneous measurement of both quadratures of each mode. This approach effectively mimicked the optimal quantum joint measurement through classical post-processing. Under identical conditions—including matched signal photon number per mode—the QI protocol achieved up to a 2 dB signal-to-noise ratio (SNR) advantage over a classical noise radar implemented in the same experimental setup. In addition to the noise radar comparison, the experiment also implemented coherent-state (CS) illumination and a digital homodyne detection scheme, representing the optimal classical strategy. By carefully calibrating the idler path and applying digital post-processing to approximate ideal photodetection, QI demonstrated up to a 1 dB SNR advantage over the CS homodyne receiver. The study further investigated how the QI performance degrades with increasing free-space distance between the target and the transmitter-receiver system. A central limitation of the demonstration was that the joint measurement was not realized in real time but reconstructed through offline processing of the recorded quadrature data. Meanwhile, fundamental theoretical limits of QI [NG20] and its experimental constraints [BW20] were further explored.

More recently, [Ass23] conducted the first microwave QI experiment utilizing an OPA receiver in cryogenic environment and showed real SNR advantage of up to 0.8 dB compared with the theoretical SNR value with CS homodyne receiver. These advancements mark steady progress toward practical QI implementations, bringing the technology closer to real-world applications in quantum radar and imaging [GMTP20].

It is crucial to establish a classical benchmark for comparing the Signal-to-Noise Ratio (SNR) performance of quantum illumination (QI). There are several classical methods for target detection, such as using coherent-state (CS) illumination, where the receiver can be either homodyne or heterodyne. Another approach involves using classically correlated noise pairs, which is commonly employed in radar systems [SSDP+20] and even in ghost imaging [ES10]. The homodyne receiver for coherent-state detection is considered the optimal classical receiver, as it provides the highest SNR. However, it requires phase coherence between the probe and received signals. In contrast, the heterodyne receiver is more robust and doesn't require perfect phase coherence, but it suffers from a 3 dB reduction in SNR compared to the homodyne case. In radar applications, comparing quantum illumination (QI) with classical noise radar that uses classically correlated noise pairs is more relevant. However, both of these methods rely heavily on phase coherence. If the phase of the returned signal is not coherent with the retained signal (which is phase-locked to the probe signal), the correlation needed for detection cannot be

Figure 4.2: The schematic of PC receiver to realize QI.

accessed, affecting both QI and noise radar performance.

4.3 Numerical model of QI with ideal PC receiver

The system begins with a continuous-wave spontaneous parametric down-conversion (SPDC) source, which generates entangled signal-idler pairs. The annihilation operators for the signal and idler modes are denoted as a_S and a_I respectively. The resulting entangled state, expressed in the number-ket representation, is given by [TEG⁺08] as:

$$|\Psi\rangle_{\mathsf{SI}} = \sum_{n=0}^{\infty} \sqrt{\frac{N_S^n}{(N_S + 1)^{n+1}}} |n\rangle_S |n\rangle_I \tag{4.3}$$

where N_S represents the mean number of signal photons per mode. In the quadrature representation, the entangled state, $|\Psi\rangle_{SI}$ is a zero-mean Gaussian state, with a covariance matrix in the Wigner distribution given by:

$$V_{SI} = \begin{bmatrix} N_S + 1/2 & 0 & C_q & 0 \\ 0 & N_S + 1/2 & 0 & -C_q \\ C_q & 0 & N_I + 1/2 & 0 \\ 0 & -C_q & 0 & N_I + 1/2 \end{bmatrix}$$
(4.4)

Here, $C_q=\langle a_Sa_I\rangle=\sqrt{N_S(N_S+1)}$ represents the maximum possible quantum correlation magnitude between a maximally entangled signal-idler pair. In contrast, a classically correlated signal-idler pair would have a correlation magnitude of $C_c=N_S$. In the low-photon regime where, $N_S<<1$, the quantum correlation exceeds the classical correlation $C_q>>C_c$ which is a clear indication of strong non-classicality in the covariance matrix V_{SI} .

To analyze detection performance, the signal beam is sent toward the interrogation region, where two possible scenarios exist:

- (i) H_0 (Target Absent): The signal returns as pure background noise.
- (ii) H_1 (Target Present): The signal is reflected by the target and mixed with noise.

In the following section, we numerically evaluate the SNR for both hypotheses to determine the effectiveness of the QI system in distinguishing between these cases.

In **Hypothesis** H_0 (target is absent), the returned signal from the target a_R contains only the noise background,

$$a_R = a_B \tag{4.5}$$

with a_B being the annihilation operator of the thermal state with mean noise photon number $N_B >> 1$. Now, the returned signal is fed in the PC receiver, whose first component is a phase-conjugator. The phase-conjugated returned signal is,

$$a_{PC} = \sqrt{G_{PC}} a_v + \sqrt{G_{PC} - 1} a_R^{\dagger}$$

$$= \sqrt{G_{PC}} a_v + \sqrt{G_{PC} - 1} a_B^{\dagger}$$
(4.6)

Here, $G_{\rm PC}$ is the gain of the phase-conjugator in reflection and a_v being the annihilation operator of the vacuum at the input of the phase-conjugated port of the phase-conjugator. The mean number of phase-conjugated signal photons considering an ideal phase-conjugator with $G_{\rm PC}=2$ is:

$$N_{PC} = \langle a_{PC}^{\dagger} a_{PC} \rangle$$

$$= \langle (\sqrt{2} a_v^{\dagger} + a_B) (\sqrt{2} a_v + a_B^{\dagger}) \rangle$$

$$= \langle a_B a_B^{\dagger} \rangle$$

$$= N_B + 1$$

$$(4.7)$$

The phase-conjugated signal and the retained idler are fed through an ideal 50:50 Beam-splitter to obtain at the Beam-splitter outputs as,

$$a_X = \frac{a_{\mathsf{PC}} + a_I}{\sqrt{2}} \tag{4.8}$$

and

$$a_Y = \frac{a_{\mathsf{PC}} - a_I}{\sqrt{2}} \tag{4.9}$$

Then the difference in the mean number of photons from both the beam-splitter outputs is detected with mean N_0 given by,

$$N_0 = N_X - N_Y = 0 (4.10)$$

and variance given by $\sigma_0^2 = N_X(N_X+1) + N_Y(N_Y+1)$

where

$$N_X = N_Y = \langle a_X^{\dagger} a_X \rangle$$

$$= \frac{1}{2} \langle (a_{PC}^{\dagger} + a_I^{\dagger}) (a_{PC} + a_I) \rangle$$

$$= \frac{1}{2} (N_{PC} + N_I)$$
(4.11)

In **Hypothesis** H_1 (target is present), the returned signal contains a tiny fraction of the probed signal along with the thermal noise.

$$a_R = \sqrt{\eta} a_S + \sqrt{1 - \eta} a_B \tag{4.12}$$

with $0 < \eta < 1$ being the reflectivity of the target and a_B represents thermal noise with mean photon number $N_B/(1-\eta)$. Now, the returned signal is fed through the ideal phase-conjugator and the phase-conjugated returned signal will be,

$$a_{PC} = \sqrt{G_{PC}} a_v + \sqrt{G_{PC} - 1} a_R^{\dagger}$$

$$= \sqrt{G_{PC}} a_v + \sqrt{G_{PC} - 1} (\sqrt{\eta} a_S + \sqrt{1 - \eta} a_B)^{\dagger}$$
(4.13)

In an ideal situation with $G_{\rm PC}=2$,

$$a_{PC} = \sqrt{2}a_v + a_R^{\dagger}$$

$$= \sqrt{2}a_v + (\sqrt{\eta}a_S + \sqrt{1 - \eta}a_B)^{\dagger}$$
(4.14)

and the mean number of phase-conjugated returned signal photons will be,

$$N_{PC} = \langle a_{PC}^{\dagger} a_{PC} \rangle$$

$$= \langle (\sqrt{2}a_v^{\dagger} + \sqrt{\eta}a_S + \sqrt{1 - \eta}a_B)$$

$$(\sqrt{2}a_v + \sqrt{\eta}a_S^{\dagger} + \sqrt{1 - \eta}a_B^{\dagger}) \rangle$$

$$= \eta(N_S + 1) + (1 - \eta)(N_B/(1 - \eta) + 1)$$

$$= \eta N_S + N_B + 1$$

$$(4.15)$$

After the phase-conjugated signal and the retained idler are interfered through the beam-splitter we obtain same as in Eq. (4.6) and (4.7) except, we now have an extra term related to the residual quantum correlation. The difference in the mean number of photons from both the beam-splitter outputs is detected with mean N_1 is given by,

$$N_1 = N_X - N_Y = 2\sqrt{\eta}C_q (4.16)$$

and variance is given by

$$\sigma_1^2 = \text{var}(N_X + N_Y)$$

$$= \text{var}(N_X) + \text{var}(N_Y) - 2\text{cov}(N_X, N_Y)$$

$$= N_X(N_X + 1) + N_Y(N_Y + 1) - \frac{(N_{PC} - N_I)^2}{2}$$
(4.17)

where,

$$N_{X} = \langle a_{X}^{\dagger} a_{X} \rangle$$

$$= \frac{1}{2} \langle (a_{PC}^{\dagger} + a_{I}^{\dagger}) (a_{PC} + a_{I}) \rangle$$

$$= \frac{1}{2} (N_{PC} + N_{I} + \langle a_{PC}^{\dagger} a_{I} \rangle + \langle a_{I}^{\dagger} a_{PC} \rangle)$$

$$= \frac{1}{2} (N_{PC} + N_{I} + 2\sqrt{\eta} C_{q})$$

$$(4.18)$$

and

$$N_{Y} = \langle a_{Y}^{\dagger} a_{Y} \rangle$$

$$= \frac{1}{2} \langle (a_{PC}^{\dagger} - a_{I}^{\dagger}) (a_{PC} - a_{I}) \rangle$$

$$= \frac{1}{2} (N_{PC} + N_{I} - \langle a_{PC}^{\dagger} a_{I} \rangle - \langle a_{I}^{\dagger} a_{PC} \rangle)$$

$$= \frac{1}{2} (N_{PC} + N_{I} - 2\sqrt{\eta} C_{q})$$

$$(4.19)$$

with

$$\langle a_{\mathsf{PC}}^{\dagger} a_I \rangle = \langle a_{\mathsf{PC}}^{\dagger} a_I \rangle = \sqrt{\eta} \langle a_S a_I \rangle = \sqrt{\eta} N_S (N_S + 1) = \sqrt{\eta} C_q$$
 (4.20)

From these, the SNR can be calculated as,

$$SNR_{QI} = \frac{(N_1 - N_0)^2}{2(\sigma_0 + \sigma_1)^2}$$

$$= \frac{2\eta N_S(N_S + 1)}{2N_B + 4N_S N_B + 6N_S + 4\eta N_S^2 + 3\eta N_S + 2}$$

$$= \frac{\eta N_S}{2N_B}$$
(4.21)

with the assumptions $N_S \ll 1$, $\eta \ll 1$, $N_B \gg 1$.

In case of the optimum classical illumination, a coherent-state signal with mean photon number same as in QI is probed to detect the target. In hypothesis H_0 , the returned signal contains only thermal noise with $N_0=N_B$ and in hypothesis H_1 the returned signal contains both the thermal noise as well as the reflected part of the probed signal with $N_1=\eta N_S+N_B$. In both hypotheses, the variance of the coherent state is same and dominated by the thermal noise. Hence we obtain the SNR as,

$$\mathsf{SNR}_{\mathsf{hom}} = \frac{\eta N_S}{4N_B} \tag{4.22}$$

Hence, the QI PC receiver achieves the maximum 3dB error-exponent gain over the optimum-classical receiver with coherent state detection.

Figure 4.3 (a) shows how the SNR for QI changes with average number of probing signal photons. At low signal power, we can observe maximum 3dB advantage in the SNR for QI, in comparison with the optimum case of CS homodyne detection and 6 dB advantage compared to using a heterodyne detection scheme. But with increase in signal power this advantage starts to reduce and at enough high signal power, classical scenario takes the advantage. Moreover, this advantage also depends on how high the background noise is. From Figure 4.3 (b) we can observe that, at zero background noise or even very low background noise, in comparison with the probing signal power, there is no advantage using QI technique. Rather with increase in background noise, the SNR advantage for QI starts increasing until it converges to maximum 3dB. So, it is very important to understand that QI is special only in specific scenarios with: $N_S << 1, 0 < \eta < 1$ and $N_B >> 1$.

This was the ideal PC receiver for QI technique. In the next section we will discuss about the possible imperfections in our experiment and including them in the model we will see how the advantage affects for QI.

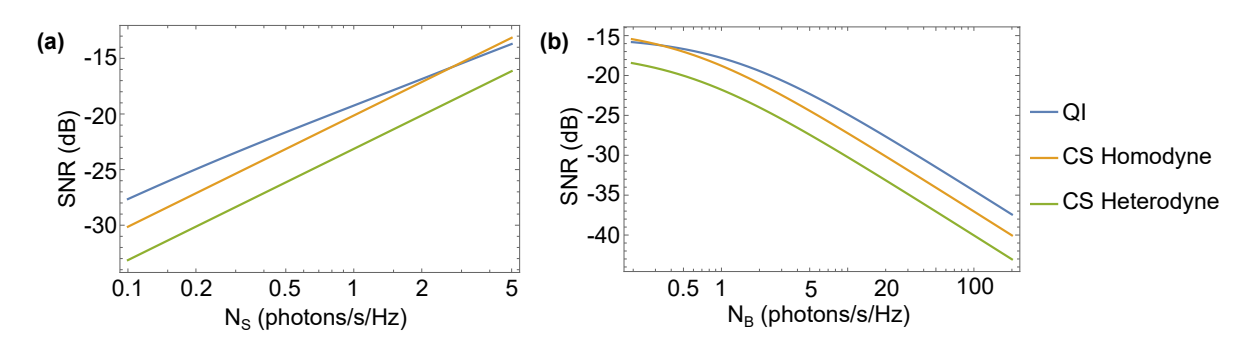


Figure 4.3: SNR comparisons between QI, coherent state(CS) with homodyne receiver and heterodyne receiver as (a) function of probing signal photon number at fixed reflectivity $\eta=1dB$ and background noise $N_B=20$; and (b) function of average number of background noise photons per mode at fixed $N_S=0.1$ with same reflectivity of the target.

4.4 Numerical model of experimental PC receiver

In the proposed phase conjugator (PC) receiver, as discussed in the previous section, the detection process involves photon counters at the beam-splitter outputs, followed by dual balanced joint detection. However, before directly implementing photon counters, we first aimed to investigate whether a quantum advantage could be achieved using the Josephson Parametric Converter (JPC) available in our lab.

To do so, we initially approached Quantum Illumination (QI) using a heterodyne detection scheme, commonly employed in superconducting quantum circuits housed in a dilution refrigerator. The experiment was conducted at millikelvin (mK) temperatures, with thermal noise artificially injected from an arbitrary waveform generator (AWG) at room temperature. The beam-splitter outputs were amplified using a HEMT at 4K, followed by two room-temperature low-noise amplifiers. The signals were then down-converted to an intermediate frequency and acquired using a $1~{\rm GS/s}$ digitizer, recording voltages for post-processing. Instead of directly using photon counters or radiometers, we digitally processed the acquired data to emulate their readings.

In this section, we numerically model the experimental setup (Fig. 4.4), initially assuming maximally entangled signal-idler pairs to assess how different setup imbalances impact the QI advantage. We then extend this analysis by incorporating the actual correlation levels obtained from the JPC, providing a more realistic evaluation of its performance.

4.4.1 Hypothesis H_1

In this case, the signal mode from JPC goes through high background noise and a tiny bit of it depending on the reflectivity η of the object reflects back to the PC-receiver. Hence, the reflected signal in this scenario will be:

$$a_R = \sqrt{\eta} a_S + \sqrt{1 - \eta} a_B \tag{4.23}$$

After this reflected signal is incident on the phase-conjugtor, the output of the PC is:

$$a_{PC} = \sqrt{G_{PC}} a_v + \sqrt{G_{PC} - 1} a_R^{\dagger}$$

$$= \sqrt{G_{PC}} a_v + \sqrt{G_{PC} - 1} (\sqrt{\eta} a_S + \sqrt{1 - \eta} \hat{a}_B)^{\dagger}$$
(4.24)

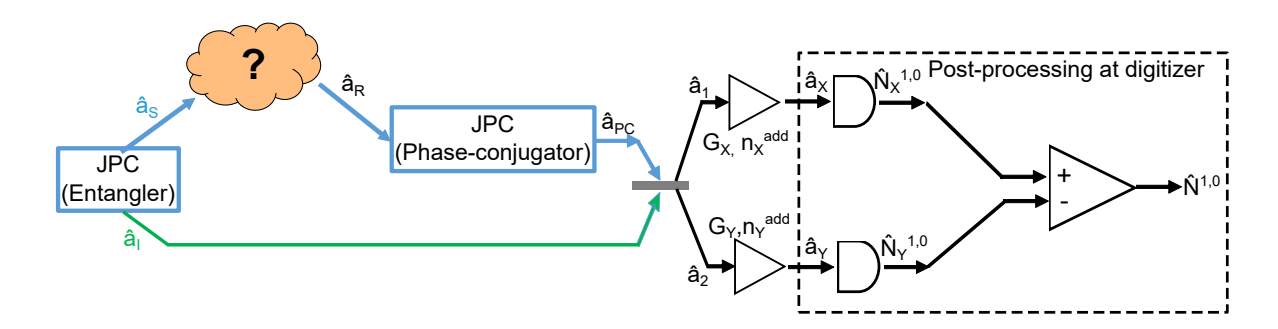


Figure 4.4: Schematic of QI setup including the heterodyne detection chain with amplifiers.

and the mean number of phase-conjugated photons will be:

$$N_{PC} = \langle a_{PC}^{\dagger} a_{PC} \rangle$$

$$= \langle (\sqrt{G_{PC}} a_v^{\dagger} + \sqrt{\eta (G_{PC} - 1)} a_S + \sqrt{(1 - \eta)(G_{PC} - 1)} a_B)$$

$$(\sqrt{G_{PC}} a_v + \sqrt{\eta (G_{PC} - 1)} a_S^{\dagger} + \sqrt{(1 - \eta)(G_{PC} - 1)} a_B^{\dagger}) \rangle$$

$$= (G_{PC} - 1)[\eta (N_S + 1) + (1 - \eta)(N_B/(1 - \eta) + 1)]$$

$$= (G_{PC} - 1)(\eta N_S + N_B + 1)$$
(4.25)

Even though we use NbTiN superconducting cable for iddler propagation from JPC to the beam splitter, there should still be some non-zero amount of loss in amplitude, let's denote that as $\sqrt{\kappa}$. The phase-conjugated signal and the idler from the JPC interact with each other through a non-ideal Beam-Splitter with amplitude splitting ratio: $\sqrt{t}:\sqrt{1-t}$. The outputs of the Beam-Splitter are:

$$a_1 = \sqrt{t} \ a_{PC} \ e^{i\phi_{PC}} + \sqrt{1-t} \ \sqrt{\kappa} \ a_I \tag{4.26}$$

$$a_2 = \sqrt{1 - t} \ \hat{a}_{PC} \ e^{i\phi_{PC}} - \sqrt{t} \ \sqrt{\kappa} \ a_I \tag{4.27}$$

Here, ϕ_{PC} is the phase introduced in the phase-conjugated signal due to the pump phase of the phase-conjugator with reference to the pump phase of the entangler JPC.

The mean number of photons at the beam-splitter outputs will be:

$$N_{1} = \langle a_{1}^{\dagger} a_{1} \rangle = \langle (\sqrt{t} \ a_{\mathsf{PC}}^{\dagger} \ e^{-i\phi_{\mathsf{PC}}} + \sqrt{1-t} \ \sqrt{\kappa} \ a_{I}^{\dagger}) \ (\sqrt{t} \ a_{\mathsf{PC}} \ e^{i\phi_{\mathsf{PC}}} + \sqrt{1-t} \ \sqrt{\kappa} \ a_{I}) \rangle$$

$$= t \ N_{\mathsf{PC}} + (1-t) \ \kappa N_{I} + \sqrt{t \ (1-t) \ \kappa} \ (\langle a_{\mathsf{PC}}^{\dagger} \ a_{I} \rangle e^{-i\phi_{\mathsf{PC}}} + \langle a_{\mathsf{PC}} \ a_{I}^{\dagger} \rangle e^{i\phi_{\mathsf{PC}}})$$

$$= t \ N_{\mathsf{PC}} + (1-t) \ \kappa N_{I} + \sqrt{t \ (1-t) \ \kappa} \ C_{q} \ (e^{-i\phi_{\mathsf{PC}}} + e^{i\phi_{\mathsf{PC}}})$$

$$= t \ N_{\mathsf{PC}} + (1-t) \ \kappa N_{I} + 2\sqrt{t \ (1-t) \ \kappa} \ C_{q} \ \cos\phi_{\mathsf{PC}}$$

$$(4.28)$$

and,

$$N_{2} = \langle a_{2}^{\dagger} a_{2} \rangle = \langle (\sqrt{1 - t} \ \hat{a}_{\mathsf{PC}}^{\dagger} \ e^{-i\phi_{\mathsf{PC}}} - \sqrt{t} \ \sqrt{\kappa} \ \hat{a}_{I}^{\dagger}) \ (\sqrt{1 - t} \ \hat{a}_{\mathsf{PC}} \ e^{i\phi_{\mathsf{PC}}} - \sqrt{t} \ \sqrt{\kappa} \ \hat{a}_{I}) \rangle$$

$$= (1 - t) \ N_{\mathsf{PC}} + t \ \kappa N_{I} - \sqrt{t \ (1 - t) \ \kappa} \ (\langle a_{\mathsf{PC}}^{\dagger} \ a_{I} \rangle e^{-i\phi_{\mathsf{PC}}} + \langle a_{\mathsf{PC}} \ a_{I}^{\dagger} \rangle e^{i\phi_{\mathsf{PC}}})$$

$$= (1 - t) \ N_{\mathsf{PC}} + t \ \kappa N_{I} - \sqrt{t \ (1 - t) \ \kappa} \ C_{q} \ (e^{-i\phi_{\mathsf{PC}}} + e^{i\phi_{\mathsf{PC}}})$$

$$= (1 - t) \ N_{\mathsf{PC}} + t \ \kappa N_{I} - 2\sqrt{t \ (1 - t) \ \kappa} \ C_{q} \ \cos \phi_{\mathsf{PC}}$$

$$(4.29)$$

The beam-splitter outputs pass through the amplifiers and cables with finite losses, hence assuming effective gain $G_{X,Y}$ and effective number of noise photons added by the amplified detection chain referenced at the beam-splitter outputs $n_{X,Y}^{add}$, the outputs at the end of the detection chain in annihilation terms will be,

$$a_X = \sqrt{G_X} \ a_1 + \sqrt{G_X - 1} \ h_X^{\dagger}$$
 (4.30)

$$a_Y = \sqrt{G_Y} \ a_2 + \sqrt{G_Y - 1} \ h_Y^{\dagger} \tag{4.31}$$

From digital post-processing, mimicking photon-counting method, the mean photon numbers at the outputs of detection chain will be,

$$N_X^1 = G_X N_1 + (G_X - 1) (n_X^{add} + 1)$$
(4.32)

$$N_Y^1 = G_Y N_2 + (G_Y - 1) (n_Y^{add} + 1)$$
(4.33)

Hence, we can calculate mean and variance of difference in photon numbers as:

Mean:

$$N^1 = N_X^1 - N_Y^1 (4.34)$$

Variance:

$$(\Delta N^{1})^{2} = Var(N_{X}^{1} - N_{Y}^{1})$$

$$= N_{X}^{1}(N_{X}^{1} + 1) + N_{Y}^{1}(N_{Y}^{1} + 1) - \sqrt{t}\sqrt{1 - t}G_{X}G_{Y}(N_{PC} - N_{I})^{2}$$
(4.35)

The detailed derivation can be found in Appendix B

4.4.2 Hypothesis H_0

When the target is absent, the returned signal is solely the thermal noise,

$$a_R = a_B \tag{4.36}$$

with $\langle a_B^\dagger a_B \rangle = N_B$ And its phase-conjugated version would be,

$$a_{PC} = (\sqrt{G_{PC}}a_v + \sqrt{G_{PC} - 1}a_R^{\dagger})e^{i\phi_{PC}}$$

$$= (\sqrt{G_{PC}}a_v + \sqrt{G_{PC} - 1}a_B^{\dagger})e^{i\phi_{PC}}$$
(4.37)

and the number of phase-conjugated photons is

$$N_{PC} = \langle a_{PC}^{\dagger} a_{PC} \rangle$$

$$= \langle (\sqrt{G_{PC}} a_v^{\dagger} + \sqrt{G_{PC}} - 1 a_B) e^{-i\phi_{PC}} (\sqrt{G_{PC}} a_v + \sqrt{G_{PC}} - 1 a_B^{\dagger}) e^{i\phi_{PC}} \rangle$$

$$= G_{PC} \langle a_v^{\dagger} a_v \rangle + (G_{PC} - 1) \langle a_B a_B^{\dagger} \rangle$$

$$= (G_{PC} - 1)(N_B + 1)$$

$$(4.38)$$

The phase-conjugator output and the idler from the JPC interacts at the Beam-Splitter. The outputs from the Beam-splitters are:

$$a_1 = \sqrt{t} \ a_{PC} \ e^{i\phi_{PC}} + \sqrt{1-t} \ \sqrt{\kappa} \ a_I \tag{4.39}$$

$$a_2 = \sqrt{1 - t} \,\,\hat{a}_{PC} \,\,e^{i\phi_{PC}} - \sqrt{t} \,\,\sqrt{\kappa} \,\,\hat{a}_I \tag{4.40}$$

The mean number of photons at the beam-splitter outputs will be:

$$N_{1} = \langle a_{1}^{\dagger} a_{1} \rangle = \langle (\sqrt{t} \ a_{\mathsf{PC}}^{\dagger} \ e^{-i\phi_{\mathsf{PC}}} + \sqrt{1-t} \ \sqrt{\kappa} \ a_{I}^{\dagger}) \ (\sqrt{t} \ a_{\mathsf{PC}} \ e^{i\phi_{\mathsf{PC}}} + \sqrt{1-t} \ \sqrt{\kappa} \ a_{I}) \rangle$$

$$= t \ N_{\mathsf{PC}} + (1-t) \ \kappa N_{I}$$

$$(4.41)$$

and,

$$N_{2} = \langle a_{2}^{\dagger} a_{2} \rangle = \langle (\sqrt{1-t} \ \hat{a}_{\mathsf{PC}}^{\dagger} \ e^{-i\phi_{\mathsf{PC}}} - \sqrt{t} \ \sqrt{\kappa} \ \hat{a}_{I}^{\dagger}) \ (\sqrt{1-t} \ \hat{a}_{\mathsf{PC}} \ e^{i\phi_{\mathsf{PC}}} - \sqrt{t} \ \sqrt{\kappa} \ \hat{a}_{I}) \rangle$$

$$= (1-t) \ N_{\mathsf{PC}} + t \ \kappa N_{I}$$

$$(4.42)$$

Similar to hypothesis H1, at the end of the amplified detection chain,

$$a_X = \sqrt{G_X} \ a_1 + \sqrt{G_X - 1} \ h_X^{\dagger}$$
 (4.43)

$$a_Y = \sqrt{G_Y} \ a_2 + \sqrt{G_Y - 1} \ h_Y^{\dagger} \tag{4.44}$$

From digital post-processing the mean photon numbers at the outputs of detection chain will be,

$$N_X^0 = G_X N_1 + (G_X - 1) (n_X^{add} + 1)$$
(4.45)

$$N_Y^0 = G_Y N_2 + (G_Y - 1) (n_Y^{add} + 1)$$
(4.46)

Hence, we will again calculate mean and variance of difference in photon numbers as:

Mean:

$$N^0 = N_X^0 - N_Y^0 (4.47)$$

Variance:

$$(\Delta N^{0})^{2} = Var(N_{X}^{0} - N_{Y}^{0})$$

$$= N_{X}^{0}(N_{X}^{0} + 1) + N_{Y}^{0}(N_{Y}^{0} + 1) - \sqrt{t}\sqrt{1 - t}G_{X}G_{Y}(N_{PC} - N_{I})^{2}$$
(4.48)

Finally, SNR in QI including amplified detection chain would be,

$$\mathsf{SNR}_{\mathsf{QI}} = \frac{(N^1 - N^0)^2}{2(\sqrt{\mathsf{var}(N^1)} + \sqrt{\mathsf{var}(N^0)})^2} \tag{4.49}$$

In order to compare QI SNR with coherent state illumination, we also find the SNR using best homodyne receiver is:

$$SNR_{Hom} = \frac{\eta G N_S}{4(G N_{env} + (G-1)n_{add})}$$

$$\tag{4.50}$$

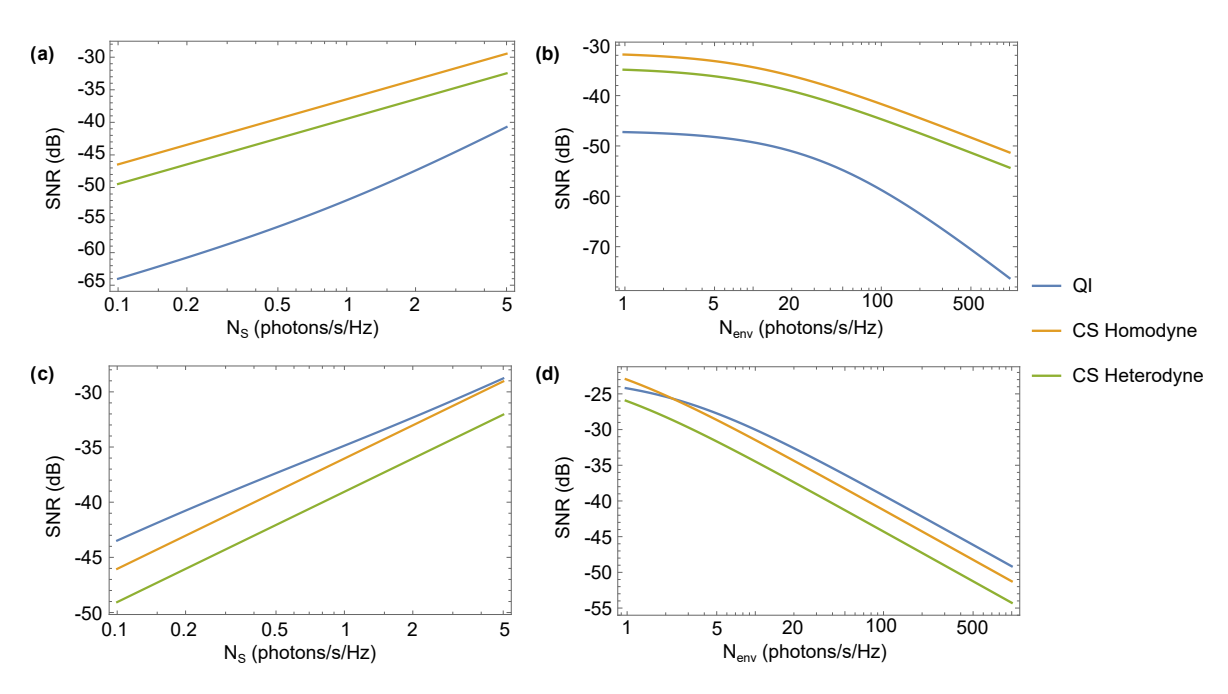


Figure 4.5: (a) SNR comparisons between QI, CS Homodyne and CS Heterodyne as function of signal photon number for $N_B=100$, $\eta=0.1$, $G_X=90$ dB, $G_Y=100$ dB, $n_{\rm add}^X=10$, $n_{\rm add}^Y=14$. (b) same as function of background noise at $N_S=0.3$. (c)-(d) same as (a)-(b) with calibrated gain and added noise in the output detection chain.

where G and $n_{\rm add}$ can be from either of the detection chains.

To better understand the **impact of gain in the detection chain**, we analyze the scenario after a perfect 50:50 beam-splitter, as shown in Figure 4.5. From Figures 4.5(a) and (b), we observe that Quantum Illumination (QI) does not exhibit any advantage over classical receivers when plotted as a function of both N_S (signal photon number) and N_B (background noise photon number). This is due to the fact that, for large gains (G >> 1), which is typically the case in our setup, the coherent-state SNR definitions remain unaffected by G. However, in QI, the gain has a significant effect, particularly in the denominator of the QI SNR definition, leading to a loss of advantage.

To recover the expected QI advantage, we must calibrate the gain and noise introduced by the detection chain and simulate the scenario as if we were counting photons immediately at the beam-splitter outputs. By doing so, we restore the advantage predicted in ideal numerical models (as derived in Section 4.3) when plotted over the same range of N_S and N_B . To further investigate, Figure 4.6(a) illustrates how QI advantage degrades as a function of gain (in dB) in the detection chain. Assuming a quantum-limited amplifier with $n_{\rm add}=0.5$, $N_S=0.1$, $N_B=24$, , no idler loss and a perfect 50:50 beam-splitter, we observe that the QI advantage persists up to 0.2 dB compared to a homodyne receiver and up to 0.5 dB relative to a heterodyne receiver. This result strongly suggests that avoiding amplification between the beam-splitter output and the photon counter is crucial to preserving QI advantage.

Another imperfection in our setup arises from **the beam-splitter's imperfect split ratio**, as we use a commercially available 3 dB 90-degree hybrid instead of a perfectly balanced 50:50 beam-splitter. Figure 4.6(b) shows the impact of this imbalance, assuming a perfect entanglement source, no idler loss, and ideal photon counters at the beam-splitter outputs. The results indicate that the QI advantage is maximized at a split ratio of t=0.5, while

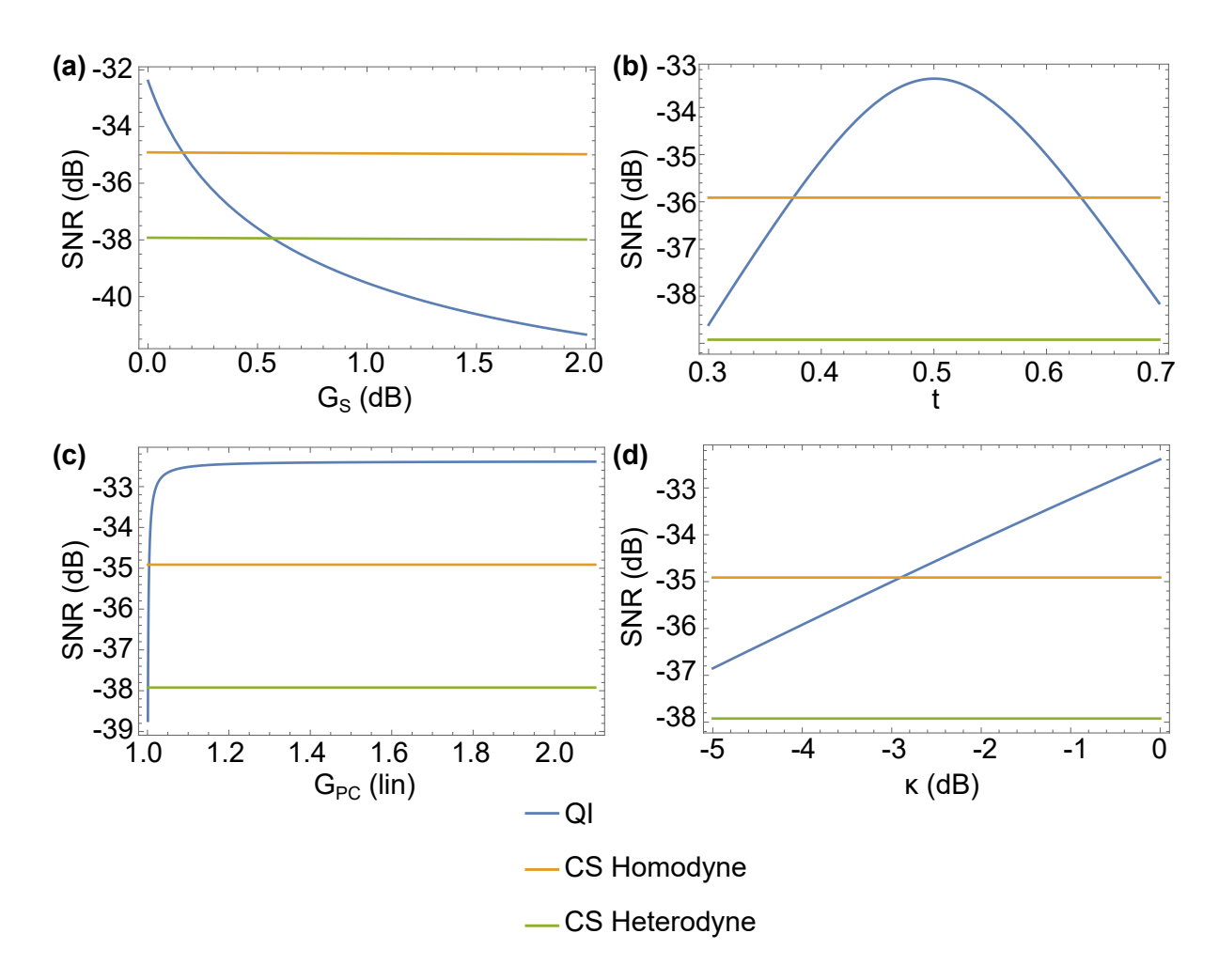


Figure 4.6: SNR comparisons between QI, CS Homodyne and CS Heterodyne (a) as function of gain $G_X=G_Y=G_S$ of the detection chain; (b) beam-splitter amplitude splitting ratio t; (c) the phase-conjugator gain G_{PC} and (d) loss in idler path κ . In all these four cases, $N_S=0.1,\ N_B=24$, and $\eta=-5$ dB.

deviations from this value lead to an asymmetric degradation of performance.

The next source of imperfection comes from **the phase-conjugation efficiency** of the phase conjugator, which in our case is another Josephson Parametric Converter (JPC) operating in a non-degenerate mode with a gain $G_{\rm PC}$. As shown in Figure 4.6(c), for the specific conditions mentioned in the figure caption, we find that once $G_{\rm PC}>1.1$ (in linear scale), the QI advantage converges, meaning that beyond this point, increasing $G_{\rm PC}$ does not further improve performance. However, this threshold in $G_{\rm PC}$ is not universal and will depend on N_S and N_B , requiring further optimization based on experimental conditions.

Finally, an unavoidable yet significant imperfection arises from **loss in the idler path**, primarily due to the circulator and the nonzero loss of the NbTiN superconducting cable used in our setup. Figure 4.6(d) reveals that even with a loss κ exceeding 2 dB, a QI advantage still exists, although it diminishes as losses increase. This highlights the importance of minimizing losses in the idler path to maximize the benefits of QI.

Through these numerical analyses, we identify several key technical imperfections—detection chain gain, beam-splitter imbalance, phase-conjugation efficiency, and idler path loss—that significantly affect the quantum advantage in our QI setup. While some imperfections,

such as beam-splitter imbalance and phase-conjugation efficiency, can be optimized through proper hardware selection and calibration, idler loss and unwanted amplification present more fundamental challenges that must be carefully managed to preserve the full benefits of QI.

4.5 The QI Experiment

The primary goal of Quantum Illumination (QI) is to detect weakly reflecting targets in the presence of high background noise, ideally at room temperature in the microwave regime. However, before advancing to this final stage, we first conduct a detailed study of QI at millikelvin (mK) temperatures.

Our setup utilizes a Josephson Parametric Converter (JPC) inside a dilution refrigerator as the entanglement generator. When pumped at frequency ω_P , the JPC produces signal (a_S) and idler (a_I) microwave modes at frequencies ω_S and ω_I respectively. The signal mode is sent to probe a noisy target inside the fridge, where its reflectivity is controlled by introducing losses from components such as cables, a cryogenic 3 dB attenuator, and cryogenic circulators. Simultaneously, background noise is artificially introduced by injecting broadband noise from an arbitrary waveform generator (AWG) at room temperature, coupled into the signal path through a 20 dB port of a directional coupler.

The attenuated signal, now mixed with high background noise, is fed into the signal port of a second JPC, which operates at the same $(\omega_S, \, \omega_I)$ working point with an identical pump frequency ω_P . This second JPC performs phase conjugation, frequency-converting the signal at its idler port to match the idler frequency of the entangler JPC. The idler outputs from both JPCs are then interfered using a 3 dB 90-degree hybrid (beam-splitter), and the resulting outputs are measured to calculate the SNR for QI.

The complete experimental setup inside the dilution refrigerator is illustrated in Figure 4.7.

4.5.1 The Experimental setup

In our implementation of Quantum Illumination (QI), we utilize a continuous-wave spontaneous parametric down-conversion (cw-SPDC) source to generate entangled signal-idler pairs in the microwave regime. A Josephson Parametric Converter (JPC) serves as an effective source for producing these pairs, with a frequency separation of nearly 4 GHz.

The target region is modeled using a series of cryogenic components, including a latching switch, a 3 dB attenuator, circulators, and a directional coupler with a 20 dB coupling port for injecting broadband noise. A cryogenic 2:1 switch determines the measurement hypothesis: when set to a 50-ohm matched port, no signal is transmitted (H_0 hypothesis), while switching to the second port, connected to the signal port of the entangler JPC, simulates H_1 hypothesis (signal transmission).

To implement the phase conjugator (PC) receiver, we introduce a second JPC, operating as a phase-conjugator, followed by a 3 dB 90-degree hybrid (beam-splitter). This hybrid combines the phase-conjugated signal with the retained idler from the first JPC. Under the H_1 hypothesis, constructive or destructive interference is observed based on the phase difference between the two signals, whereas in the H_0 hypothesis, no interference occurs.

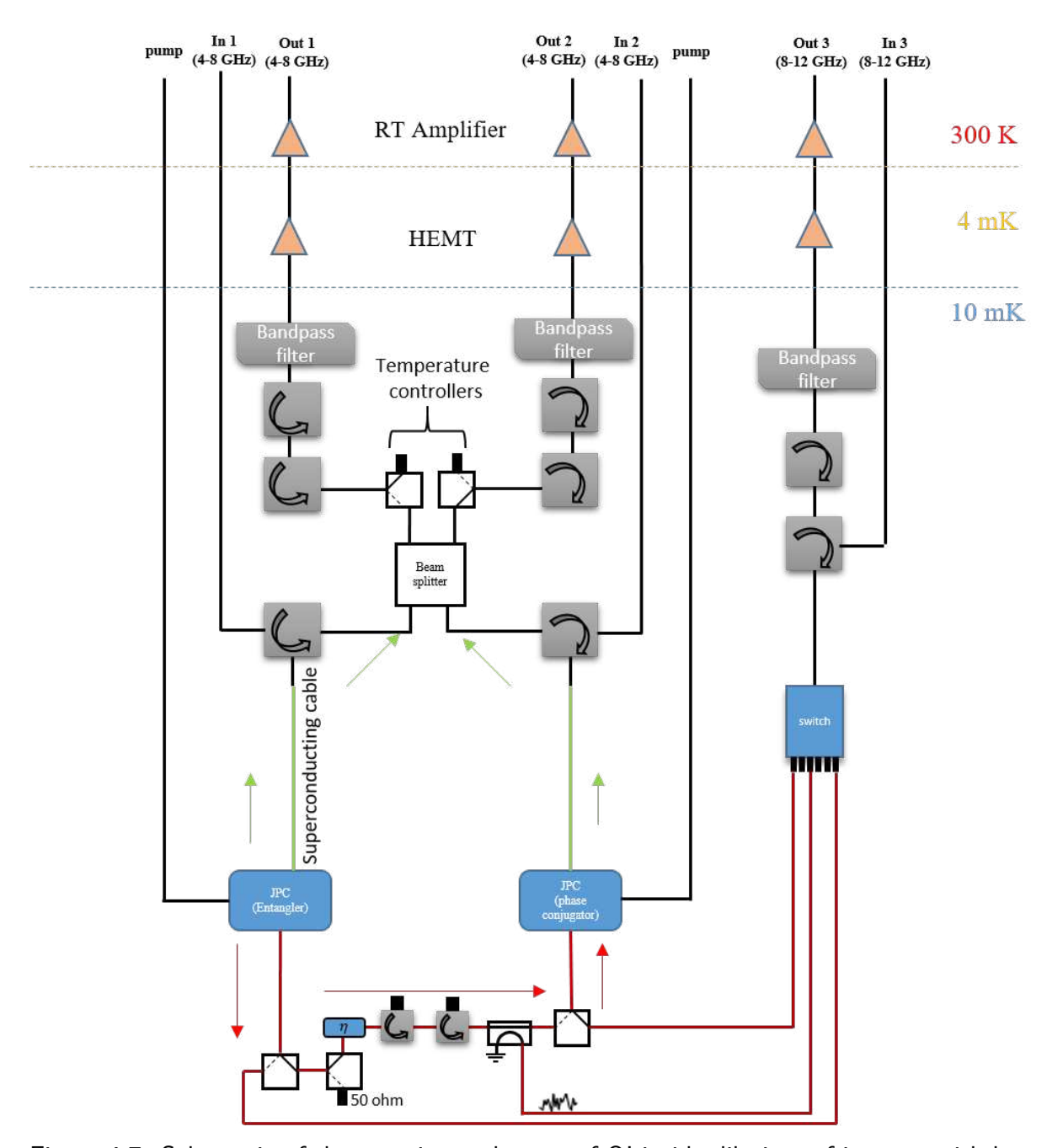


Figure 4.7: Schematic of the experimental setup of QI inside dilution refrigerator with base temperature at around 15 mK. The JPCs were donated by IBM.

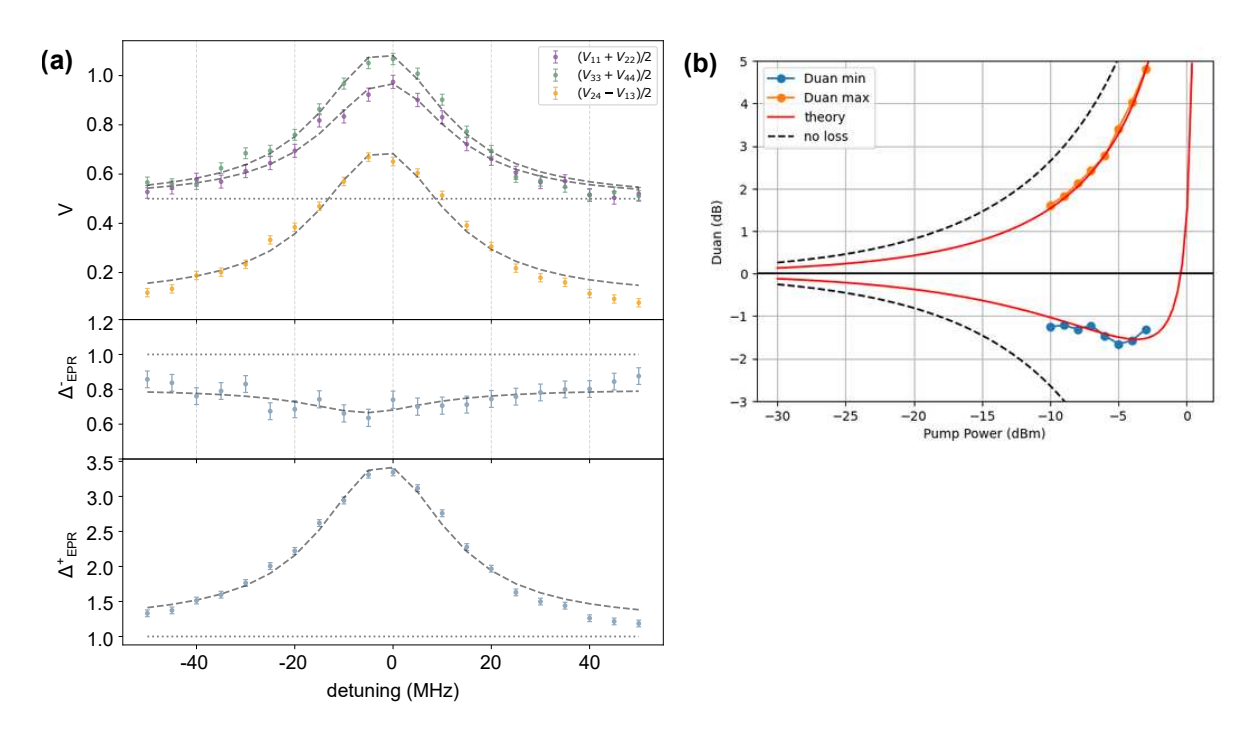


Figure 4.8: (a) The top section shows the measured covariance matrix elements as function of LO frequency detuning at pump power -1 dBm. The middle section shows how minimum Duan value Δ^- and the bottom section shows maximum Duan value Δ^+ as function of LO detuning. At detuning 0 MHz, the entanglement is the maximum observed from both squeezing (Δ^-) and anti-squeezing (Δ^+) as expected. The black dashed lines show the fits. (b) The measured Duan values both minimum (squeezing) and maximum (anti-squeezing) at detuning 0 MHz as function of pump power from entangler JPC is shown alongwith the theory-fit including losses (orange curve) as well as ideal case (black dashed line) with zero loss.

4.5.2 JPC as source of Entangled light

The nonlinearity of a Josephson Parametric Converter (JPC) [SBF10], [AKD13], [FRM+12], [SZGH+16], [ASJ+25] arises from a Josephson ring modulator (JRM) connected to two half-wavelength microstrip transmission line resonators, one for the signal mode and one for the idler mode. When a pump at frequency $\omega_P/2\pi$ is applied, the nonlinearity generates signal and idler microwave modes at frequencies $\omega_S/2\pi$ and $\omega_I/2\pi$ respectively. This process follows both energy and momentum conservation rules, so we have the relations:

$$\hbar\omega_P = \hbar\omega_S + \hbar\omega_I
\vec{k}_P = \vec{k}_S + \vec{k}_I$$
(4.51)

 $ec{k}_P, ec{k}_S$ and $ec{k}_I$ are the wavevectors of the pump, signal, and idler, respectively.

The signal mode corresponds to a differential excitation of two $\lambda/2$ signal resonators, and similarly, the idler mode corresponds to a differential excitation of two idler resonators. The signal and idler frequencies can be tuned by applying a magnetic field through a superconducting coil mounted outside the JPC package, vertically on top of the JRM. Two broadband 180° hybrids are used outside the JPC package to excite the signal and idler modes through the Δ ports. The pump drive is applied through the Σ port on the idler side, and the other Σ port on the signal side is terminated by a cryogenic 50Ω termination. In the current experiment, we

chose the working point where the signal mode is at $\omega_S/2\pi=10.2$ GHz and the idler mode is at $\omega_I/2\pi=6.86$ GHz. The amplification bandwidth at 10 dB gain is approximately 30 MHz, and the 1 dB compression point is around -112 dBm at the input of the device. The signal and idler frequencies can be tuned over a 100 MHz range by adjusting the magnetic field.

When pumping the JRM in the non-degenerate amplification mode, the produced signal and idler modes are in a squeezed state. The input-output relation for the amplifier modes is described by:

$$a_{S,\text{out}} = \cosh(r)a_{S,\text{in}} + e^{i\phi_P}\sinh(r)a_{I,\text{in}}^{\dagger}$$

$$a_{I,\text{out}}^{\dagger} = \cosh(r)a_{I,\text{in}}^{\dagger} + e^{-i\phi_P}\sinh(r)a_{S,\text{in}}$$

$$(4.52)$$

Here a_S and a_I are the signal and idler modes of the amplifier, $re^{i\phi_P}$ is the squeezing parameter with ϕ_P being the pump phase and r>=0 depends on the amplitude of the applied pump which determines the gain $G=\cosh^2(r)$.

The two-mode squeezing operation can be understood as follows: the input vacuum states at the modes a_S and b_I within their respective bandwidths are amplified and reflected at the outputs during the pumping process. In quadrature representation, let the dimensionless quadratures of the modes be $\{I_S,Q_S,I_I,Q_I\}$ for the output fields at the signal and idler modes. A pair of EPR operators can be constructed from these quadratures: $I_-=(I_S-I_I)$ and $Q_+=(Q_S+Q_I)$. If the modes are entangled, the orthogonal linear combinations of these quadratures exhibit squeezing and anti-squeezing. In the ideal case, when there is no loss, the squeezing and anti-squeezing are given by: $\langle I_-^2-Q_+^2\rangle=e^{-2r}/2$ and $\langle I_-^2+Q_+^2\rangle=e^{2r}/2$ respectively [BvL05].

However, in the presence of losses at the output resonators, the output modes can be modeled as a beam-splitter interaction with thermal baths at the inputs:

$$a'_{S, \mathsf{out}} = \sqrt{1 - \alpha} \quad a_{S, \mathsf{out}} + \sqrt{\alpha} \quad a_{S, \mathsf{th}}$$

$$a'_{I, \mathsf{out}} = \sqrt{1 - \beta} \quad a_{I, \mathsf{out}} + \sqrt{\beta} \quad a_{I, \mathsf{th}}$$
(4.53)

where, $a_{S,\text{th}}, a_{I,\text{th}}$ are the input thermal modes at the modes a and b and α, β are the power losses of the output fields.

Since the output fields are Gaussian states, their Wigner function is given by: [BvL05]

$$W(\zeta) = \frac{1}{4\pi^2 \sqrt{\det V}} exp\left\{-\frac{1}{2}\zeta V^{-1}\zeta^T\right\}$$
 (4.54)

where V is the covariance matrix with elements $V_{ij} = \langle \zeta_i \zeta_j + \zeta_j \zeta_i \rangle$ and $\zeta \in \{I_S, Q_S, I_I, Q_I\}$. The covariance matrix will look like:

$$\begin{bmatrix} \alpha + \bar{\alpha} \cosh(2r) & 0 & \sqrt{\bar{\alpha}\bar{\beta}} \sinh(2r) & 0 \\ 0 & \alpha + \bar{\alpha} \cosh(2r) & 0 & -\sqrt{\bar{\alpha}\bar{\beta}} \sinh(2r) \\ \sqrt{\bar{\alpha}\bar{\beta}} \sinh(2r) & 0 & \beta + \bar{\beta} \cosh(2r) & 0 \\ 0 & -\sqrt{\bar{\alpha}\bar{\beta}} \sinh(2r) & 0 & \beta + \bar{\beta} \cosh(2r) \end{bmatrix}$$
(4.55)

with
$$\bar{\alpha}=1-\alpha$$
 and $\bar{\beta}=1-\beta$

Figure 4.8 (a) shows both the diagonal and off-diagonal elements of the covariance matrix constructed from the recorded output fields, after applying the proper temperature calibration referenced at the output of the device. The diagonal elements V_{ii} represent the average number of output photons in each mode, including vacuum contributions, while the off-diagonal element V_{13} represents the correlation between the output modes. From these elements, we can compute the EPR measures: $\Delta_{\text{EPR}}^{\pm} = V_{11} + V_{33} \mp 2V_{13}$. As shown in Figure 4.8 (a), as a function of the local oscillator (LO) detuning, at zero detuning, the correlation between the modes is maximized, leading to the maximum Δ^+ and minimum Δ^- . Figure 4.8(b) shows the experimentally extracted Duan values as a function of pump power. From the theoretical fit, we extracted the losses in the signal and idler modes, which were found to be 0.68 and 0.17, respectively.

4.5.3 JPC as phase-conjugator

Phase conjugation is a nonlinear optical process in which an incoming wave is transformed into its complex-conjugated counterpart. This means that the phase of the wave is reversed while its amplitude remains unchanged. As a result, the phase-conjugated wave propagates in the opposite direction but maintains the same wavefront as the original wave. This unique property makes phase conjugation useful in various applications like wavefront correction.

Several nonlinear interactions can generate phase-conjugated waves, including three-wave mixing, four-wave mixing, and Stimulated Brillouin Scattering. To understand the concept mathematically, we express an electromagnetic wave as:

$$\vec{E}(\vec{r},t) = \vec{A}(\vec{r},t)e^{i(\vec{k}\cdot\vec{r}-\omega t)} + \text{c.c}$$
 (4.56)

where ω is the angular frequency, \vec{k} is the wave vector, and $\vec{A}(\vec{r},t)$ is the amplitude, which depends on position \vec{r} .

Now, if a system induces phase conjugation, the resulting wave takes the form:

$$\vec{E}_{PC}(\vec{r},t) = \vec{A}(\vec{r},t)e^{i(-\vec{k}\cdot\vec{r}-\omega t)} + \text{c.c}$$

$$= \vec{E}(\vec{r},-t)$$
(4.57)

This equation reveals a key feature of phase conjugation: the phase-conjugated wave is identical to the original wave but exhibits time reversal. In other words, if the incident wave

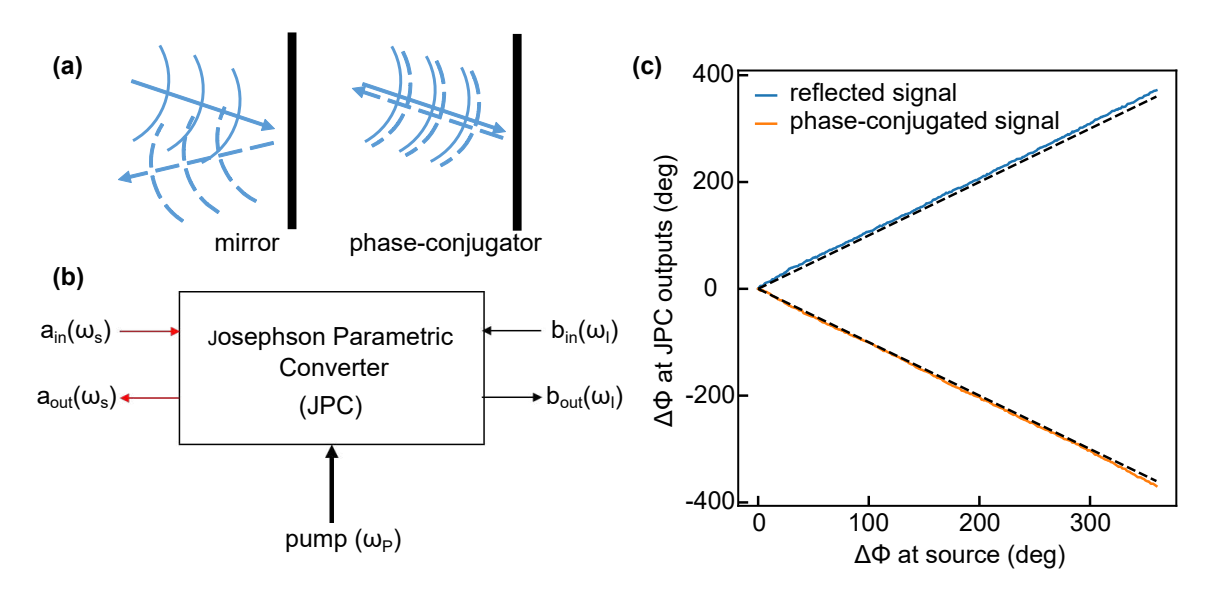


Figure 4.9: **(a)** Schematics of difference between reflection and phase-conjugation. **(b)** A schematic of Josephson Parametric Converter in non-degenerate mode where signal and idler photons emerge through two spatially separated resonators with pump interacting with the nonlinear element, that is Josephson ring modulator. **(c)** Observation of phase conjugation in JPC and differentiating it from the reflection.

were to propagate forward in time, the phase-conjugated wave would behave as if time were running backward. This property directly relates to frequency conjugation, making phase conjugation particularly valuable in signal recovery and quantum applications.

One way to achieve phase conjugation is through three-wave mixing, a process that occurs in a Josephson Parametric Converter (JPC). In the non-degenerate mode, the interaction among the signal, idler, and pump waves follows the frequency relation:

$$\omega_P = \omega_S + \omega_I \tag{4.58}$$

where ω_P , ω_S , and ω_I are the angular frequencies of the pump, signal, and idler waves, respectively.

The input-output relations of the JPC in the frequency domain can be written as:

$$a_{\text{out}}(\omega_S) = \sqrt{G}a_{\text{in}}(\omega_S) + \sqrt{G - 1}b_{\text{in}}(-\omega_I)$$

$$b_{\text{out}}(\omega_I) = \sqrt{G}b_{\text{in}}(\omega_I) + \sqrt{G - 1}a_{\text{in}}(-\omega_S)$$
(4.59)

These equations highlight a key feature of the JPC: the outgoing signal is not only amplified but also phase-conjugated and frequency-converted. This property is particularly valuable in our application, as it enables interference between the phase-conjugated returned signal and the stored idler.

The phase-conjugation effect in the JPC can be directly observed by analyzing how the output signal's phase responds to changes in the input. Specifically, if the phase of the input signal increases (or decreases), the phase of the phase-conjugated output decreases (or increases) by the same amount. This behavior differs from conventional reflection, where the phase shift of the reflected wave follows that of the input.

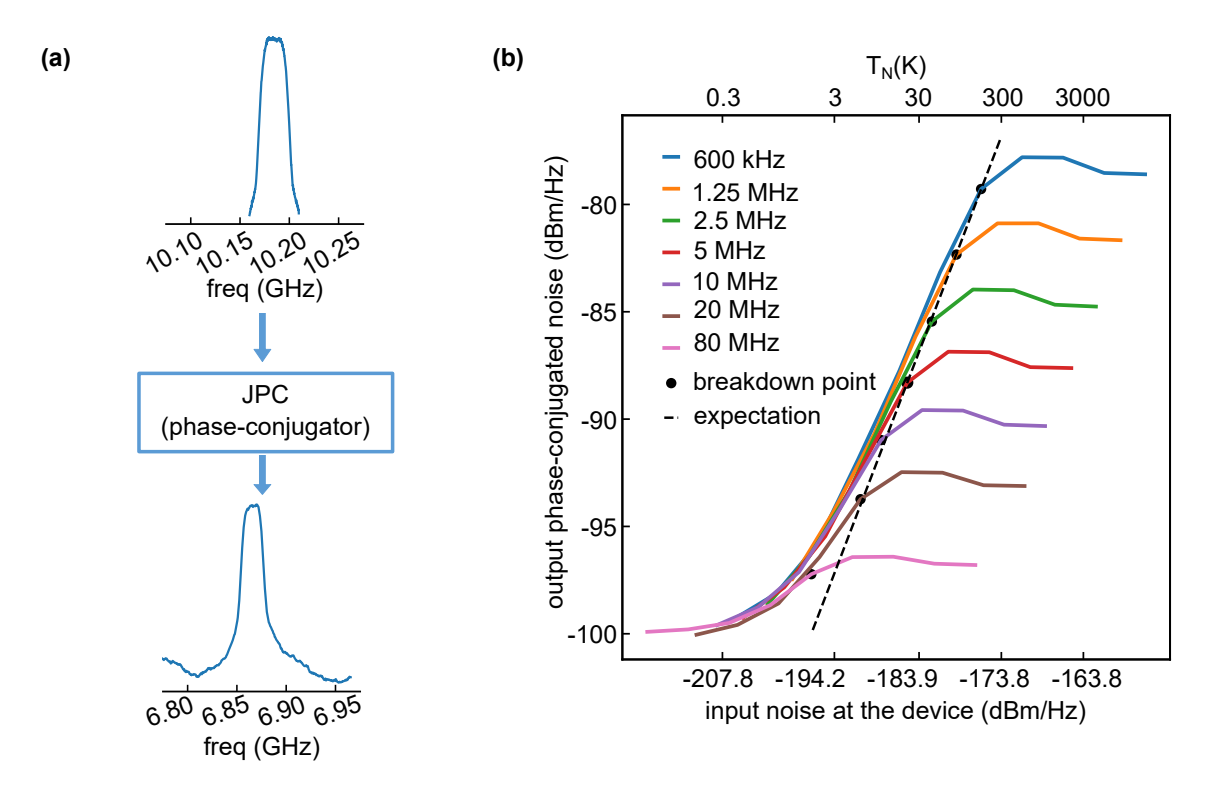


Figure 4.10: **(a)** 20 MHz noise from AWG is fed to phase-conjugator at Idler port and the noise is phase-conjugated and frequency converted to signal frequency range. **(b)** Output phase-conjugated noise power as function of input noise power for different noise bandwidth is shown.

Noise resilience of our phase-conjugator

The primary goal of the quantum illumination (QI) approach is to enhance target detection in a high-noise environment, ideally matching the level of room-temperature thermal noise in the microwave regime. To achieve this, it is essential to determine the noise tolerance of the phase-conjugator. In the experiment, the noise under Hypothesis H_0 (absence of the target) and both the signal and noise under Hypothesis H_1 (presence of the target) pass through the phase-conjugator. If the phase-conjugator saturates, it may obscure the expected advantage of QI, making it crucial to understand its noise-handling capability.

To test this, we generate a broadband noise signal (up to 80 MHz) using an arbitrary waveform generator (AWG) and then upconvert it to match the operating frequency of the phase-conjugator. Due to this upconversion, the noise bandwidth effectively doubles. The noise is then fed into the JPC's idler input via a digitally controlled attenuator, allowing precise control over the input noise power. The JPC is continuously pumped at 3 dB gain, as this is the point where we expect to observe the maximum advantage of QI.

The output noise power is analyzed as a function of both input noise power and input noise bandwidth. Our observations show that as the input noise bandwidth decreases, the input noise power increases, leading to a higher saturation threshold for the JPC. Specifically, when using a 600 kHz wide noise signal, we can push the saturation point close to the equivalent of thermal noise at 300 K. Given that our measurement bandwidth is 250 kHz, the 600 kHz noise can be effectively considered broadband noise for this experiment.

4.5.4 The Target

The target setup consists of a cryogenic 2:1 switch, a 3 dB attenuator, and a directional coupler. One port of the switch is connected to the signal port of the Entangler JPC via two circulators, which help minimize reflections back to the JPC. Switching to this port corresponds to the H_1 hypothesis, allowing the signal to pass through. The second port is terminated with a cryogenic 50-ohm load, properly thermalized to ensure that no signal reaches the phase-conjugator JPC, thus realizing the H_0 hypothesis.

Broadband noise is introduced into the signal path through the 20 dB coupling port of the directional coupler, ensuring a constant noise level at the signal port of the phase-conjugator JPC in both H_1 and H_0 scenarios. In practice, the overall reflectivity (or attenuation) is influenced by 3 dB attenuator, two circulators,the directional coupler and the Cu-cables, collectively contributing to an attenuation of approximately 5 dB.

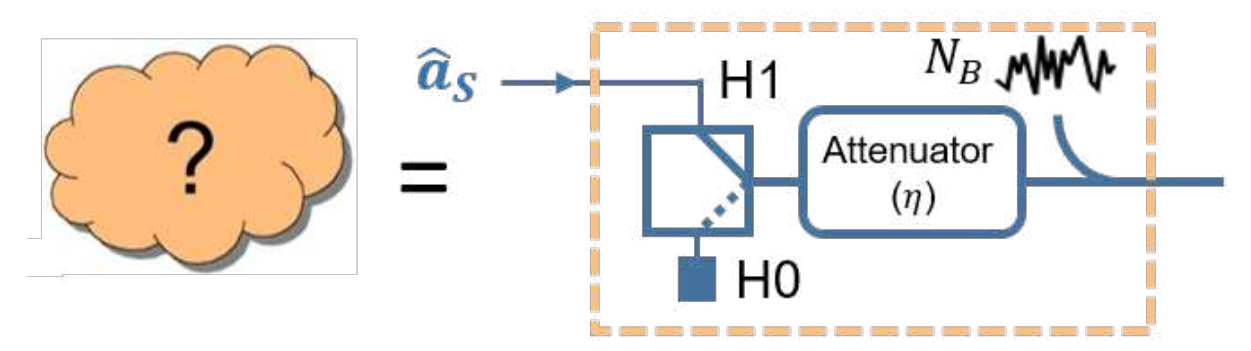


Figure 4.11: We mimic the target by combining a cryo 2:1 switch and a directional coupler to combine the noise in the path.

4.5.5 Calibration of the output detection chain

The system gain G_i and system noise $n_i^{\rm add}$, for both the signal and idler measurement chains are determined by introducing a calibrated thermal noise source using temperature-controlled 50-ohm cold loads [FRM+12], [KKM+15], [SBF19], [BPVF20], [SQH+23]. These loads are connected to the measurement setup via two identical copper coaxial cables, matching the length and material of those linking the JPC. The connections are managed through two latching microwave switches (Radiall R573423600), while a thin copper braid provides weak thermal anchoring to the mixing chamber plate to maintain temperature stability.

To characterize the system response, the noise power spectral density (V^2/Hz) is recorded at various temperatures (as depicted in Figure 4.12) and fitted to the expected theoretical model:

$$N_i = \hbar \omega \mathsf{B} \; \mathsf{R} G_i [\frac{1}{2} \mathsf{coth}(\frac{\hbar \omega}{2k_B T}) + n_i^{\mathsf{add}}] \tag{4.60}$$

where B = 250 kHz, R = 50 Ω , $\omega/2\pi=6.854$ GHz. Using this calibration approach, we extract the total system gains:

$$G_X = 112.235 \pm 0.187$$
 dB, $G_Y = 112.307 \pm 0.072$ dB (4.61)

and the mean number of added noise photons, referenced to the beam-splitter outputs:

$$n_X^{\text{add}} = 20.785 \pm 1, \quad n_Y^{\text{add}} = 13.906 \pm 0.277$$
 (4.62)

The uncertainties represent the 95% confidence interval derived from the curve fitting process.

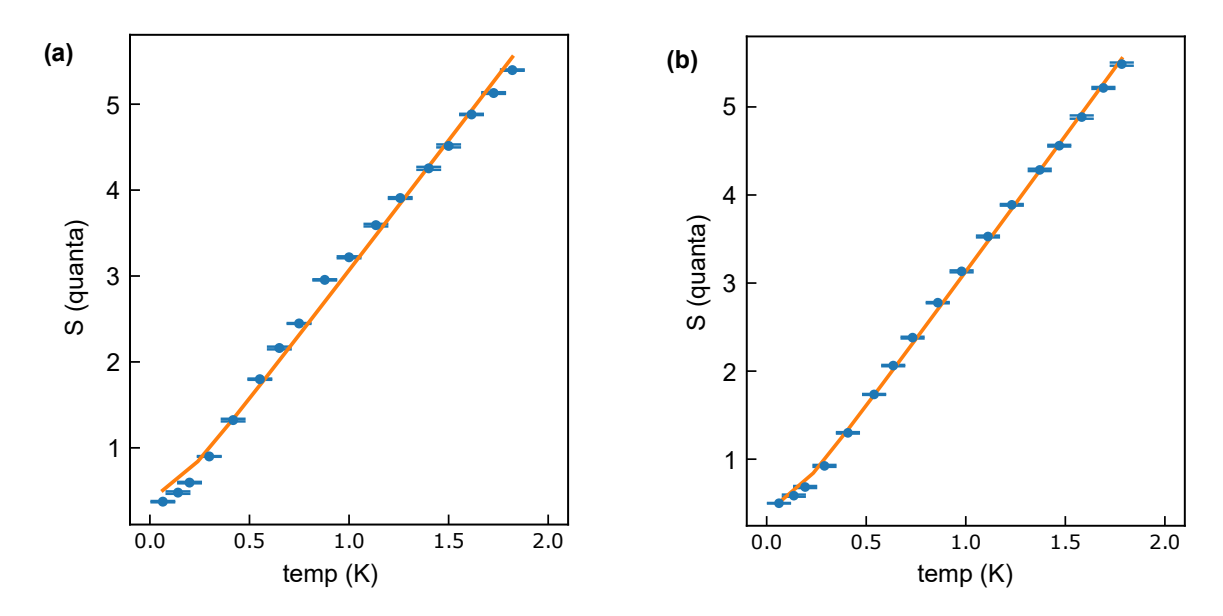


Figure 4.12: (a) and (b) show the noise spectral density in the unit of quanta as function of temperature. From fitting them with Eq.(4.57) we obtain the effective gains and total noise added referenced at the temperature calibration tool respectively in two output detection chains

4.5.6 QI experimental method

Under H_1 , the signal ports of both JPCs are connected with approximately 5 dB attenuation. Both JPCs are continuously pumped at 17.06 GHz, generating entangled photon pairs at 6.854 GHz (idler) and 10.206 GHz (signal) from the Entangler. The idler outputs from the Entangler JPC and the phase-conjugator JPC interfere at a 3 dB 90-degree hybrid (beam-splitter). The idler from the second JPC contains both the attenuated signal from the Entangler and the injected noise from the directional coupler in the signal path.

The beam-splitter outputs are first amplified using a HEMT at 4K, followed by two room-temperature low-noise amplifiers. The signals are then down-converted to an intermediate frequency $f_{\rm IF}=100$ MHz using IQ mixers. A high IF was chosen because the entangler's amplification bandwidth, at the working pump powers, is only around 40–50 MHz. The signals are then filtered through a 300 MHz low-pass filter before being digitized by an ADC.

To extract the time-dependent quadratures in voltage units, the digitized data is digitally down-converted to 0 Hz and low-pass filtered with a resolution bandwidth of 250 kHz. This acquisition process of recording 10^6 samples is repeated while varying the pump phase of the phase-conjugator JPC relative to the Entangler JPC pump phase. Under H_1 , the power difference between the beam-splitter outputs should reflect the attenuated correlation between the signal and idler of the Entangler JPC. This correlation manifests as a sinusoidal variation in power difference as a function of the phase of the phase-conjugator pump, as seen in Fig. 4.13(a). This sinusoidal variation confirms the successful operation of the Quantum Illumination (QI) experiment.

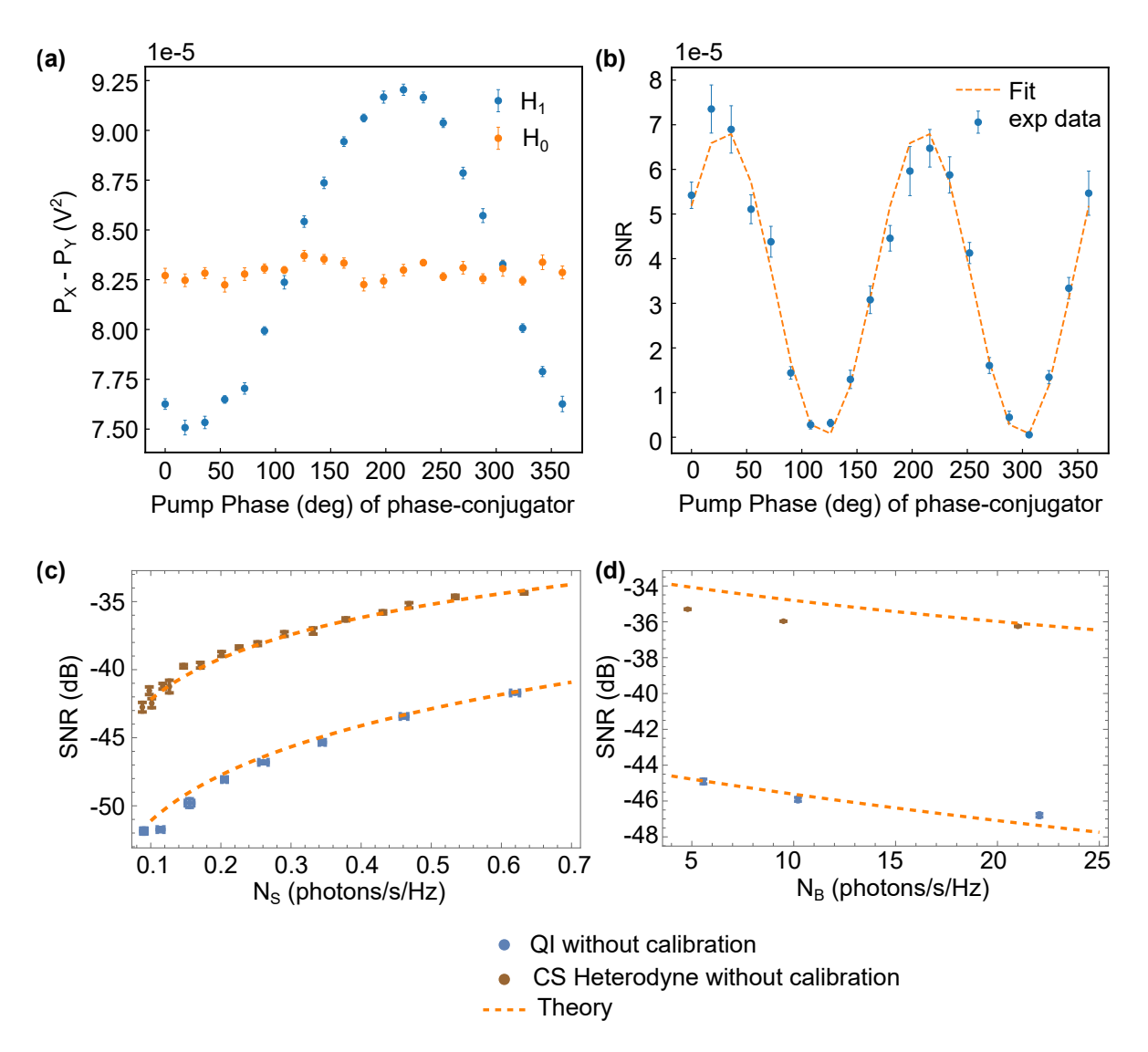


Figure 4.13: (a) The power difference between the beam-splitter outputs as function of pump phase of the phase-conjugator with respect to that of the entangler. (b) The calculated QI SNR as function of pump-phase of the phase-conjugator. Comparison between SNRs with QI and CS heterodyne receivers as (c) function of probing signal photon number N_S and (d) thermal noise present at the detection region N_B . In last two cases, the QI SNR value is taken at pump phase equivalent to zero from (b).

Under H_0 , the signal port of the Entangler JPC is disconnected from the signal path. Both JPCs are still pumped identically to the H_1 scenario, and the data is recorded using the same intermediate frequency, digitizer sampling rate, and resolution bandwidth. Since the signal from the Entangler is absent, the beam-splitter output power difference should ideally show zero correlation between the idler of the Entangler JPC and the phase-conjugated noise from the second JPC. As a result, there should be no variation in the power difference as a function of the phase-conjugator pump phase, which is evident in Fig. 4.13(b). Ideally, the power difference should be zero under H_0 and exhibit a sinusoidal variation around zero under H_1 . However, in our experiments, we observe a small offset in the power difference. This deviation is due to the imbalanced split ratio of the beam-splitter, as discussed in Section 4.4.

4.5.7 QI SNR extraction without calibration

Using the raw data, the Quantum Illumination (QI) SNR is given by:

$$SNR = \frac{(\bar{P}^1 - \bar{P}^0)^2}{2(\Delta P^1 + \Delta P^0)^2}$$
(4.63)

where, $\bar{P}^{1(0)}$ represents the difference between the beam-splitter output powers recorded at the digitizer under H_1 (signal present) and H_0 (signal absent). This is defined as:

$$\bar{P}^{1(0)} = \bar{P_X}^{1(0)} - \bar{P_Y}^{1(0)} \tag{4.64}$$

with the individual power terms calculated as:

$$\bar{P_X}^{1(0)} = \frac{\langle (I_X^{1(0)})^2 + (Q_X^{1(0)})^2 \rangle}{2}, \quad \bar{P_Y}^{1(0)} = \frac{\langle (I_Y^{1(0)})^2 + (Q_Y^{1(0)})^2 \rangle}{2}$$
(4.65)

Here, $\{I_X,Q_X,I_Y,Q_Y\}$ are measured in both H_1 and H_0 conditions. Measurements are performed in two scenarios: (i) Everything off - - to quantify the added noise in the detection chain; and (ii) Everything on - to analyze the full system performance.

Initially, the raw data SNR is calculated using only the "Everything On" measurements, without applying any calibration from the "Everything Off" data. Following Eq. (4.63), we can calculate SNR as function of the phase-conjugator's pump phase as shown in Fig. 4.13(b) from data shown in Fig. 4.13(a). From fitting it with a sinusoid function, we can get the amplitude of the sinusoid which is the maximum SNR we can get at this particular situation. If we repeat the same measurements for different pump powers of the entangler JPC, we can plot SNR values from each of these measurement as function of average signal photon number per mode as shown in blue dots with error bars in both axes in Fig. 4.13(c). Under these conditions, the QI SNR does not surpass the Classical Heterodyne SNR, as shown in Fig. 4.13(c)-(d). The figure also presents the theory (orange dashed line) including the real correlation values referenced at the JPC outputs (shown in Fig. 4.8(b)), the power-split ratio, t=0.55, the gain of the phase-conjugator $G_{PC}\approx 2.2$, the applied average background noise $N_B\approx 22$ and the heterodyne detection chain properties $G_{X,Y}$ as well as $n_{X,Y}^{\mathsf{add}}$ values obtained from the calibration measurement and we could extract $\eta \approx 4.5$ dB. The fit demonstrating strong agreement between theory and experiment in the non-calibrated scenario. As previously predicted numerically in Section 4.4, no QI advantage is observed at this stage.

4.5.8 Coherent state illumination experiment

A coherent state with the same mean photon number as in Quantum Illumination (QI) is generated using a microwave R&S source. This signal is then mixed with up-converted broadband noise before being sent into the dilution refrigerator. Inside the fridge, it is injected into the signal path through the 20 dB coupling port of a directional coupler.

The attenuation of the coherent state in the signal path is controlled by adjusting the RF output power of the R&S source. Once inside the system, both the coherent signal and noise undergo phase conjugation through the phase-conjugator JPC, with an amplification of 3 dB, before passing through a beam-splitter. Since the phase-conjugator gain and beam-splitter

attenuation are part of the detection chain, they do not affect the SNR for coherent state illumination. This can be directly observed from the coherent-state SNR equation.

Since we perform heterodyne detection, we have direct access to the Coherent-State (CS) Heterodyne SNR, which is calculated as:

$$\mathsf{SNR} = \frac{(\langle I_{X(Y)}^1 \rangle - \langle I_{X(Y)}^0 \rangle)^2 + (\langle Q_{X(Y)}^1 \rangle - \langle Q_{X(Y)}^0 \rangle)^2}{2(\sqrt{(\Delta I_{X(Y)}^1)^2 + (\Delta Q_{X(Y)}^1)^2} + \sqrt{(\Delta I_{X(Y)}^0)^2 + (\Delta Q_{X(Y)}^0)^2})^2} \tag{4.66}$$

where X and Y denote the two beam-splitter outputs used to compute the SNR. The SNR values from both channels are identical, confirming consistency in measurement. Fig. 4.13(c)-(d) show comparison between the SNR's of CS heterodyne and QI with their theoretical fits.

4.6 Conclusions and outlook

In this work, we successfully implemented and experimentally observed the Quantum Illumination (QI) protocol, even though we did not achieve an advantage over the Coherent-State (CS) illumination with heterodyne detection. By fitting our results to the numerical model in Section 4.4, we identified that the loss of quantum advantage primarily resulted from amplification and added noise in the detection chain. However, additional limitations—including an imperfect beam-splitter, unavoidable idler path loss, and squeezing impurity—also played a crucial role, particularly since high-purity squeezing is essential for any observable QI benefit. Furthermore, aging effects led to significant losses in both signal and idler resonators of the Josephson Parametric Converters (JPCs), further degrading squeezing purity.

Moving forward, our immediate objective is to extract the signal-to-noise ratio (SNR) at the output of the beam splitter with resolution bandwidth (RBW) of 250 kHz through proper calibration in digital post-processing. Using data obtained from heterodyne detection, we can employ the photon state tomography method described in [EBL+11] to reconstruct the Wigner function for Fock states. From the reconstructed Wigner function, we can construct a histogram as a function of Fock state occupation. This histogram allows us to directly extract both the mean photon number and the variance—two key quantities required to evaluate the SNR of both QI and classical detection techniques.

Ultimately, our goal is to utilize real cryogenic microwave photon counters, such as the device demonstrated in [LDA+20]. It uses a buffer-qubit-waste architecture and is capable of detecting, on average, up to 1.2 itinerant microwave photons in a cycle of 7 μs with detection bandwidth of 140 kHz. If our setup involves detecting approximately 20 photons $\rm s^{-1}Hz^{-1}$ per mode — which, after being split at the beam splitter, results in an average of about 10 photons per output — we can mitigate the photon flux by implementing an ideal bandpass filter with a bandwidth of approximately 14 kHz, but this approach increases the measurement duration — requiring roughly 10 times more time per repetition to detect a photon. Or, we could measure with the detector only 10% of the time ,i.e., 700 ns and it would be easier to implement. But in any case, we need to perform to accumulate sufficient statistics, we need to perform a large number of repetitions, typically $M>10^5$ leading to a total acquisition time on the order of hours. From the detection clicks, we can directly extract the mean photon number. Instead of filtering the bandwidth before the detector, another possibility is to reduce the gain of the phase-conjugator, thereby decreasing the photon number in the phase-conjugated signal.

4. Quantum Illumination

However, as shown in Fig. 4.6(c), the signal-to-noise ratio (SNR) begins to deteriorate below a certain threshold. However, to determine the photon number variance, we must perform heterodyne detection on the field emitted from the waste resonator, conditioned on a detector click. This heralded measurement enables photon state tomography of the single-photon Fock state, following the method described in $[EBL^+11]$. But this variance might also depend on the qubit linewidth or the lowest bandwidth of the detector.

Additionally, through our experiments, we identified several key technical aspects essential for observing signal-idler correlations in H_1 (Fig. 4.13(a)). We found that locking all pump sources, LO sources, the noise upconverter, and the coherent source to a common 1 GHz clock—with the Entangler JPC pump source referenced to a 10 MHz clock—significantly improved correlation. Moreover, the phase stability of both JPCs was highly dependent on the locking between the pump and LO sources.

One advantage of using a continuous-wave (CW) signal-idler generation scheme was that precise path-length matching of the signal and idler before reaching the beam-splitter was unnecessary. Instead, we leveraged digital signal processing, applying a 250 kHz resolution bandwidth to extract correlations, which was sufficient in the time domain to ensure signal-idler overlap.

The ultimate long-term goal is to realize QI at room temperature. One possible approach is to use cryogenic components as the QI transmitter-receiver while sending the signal out of the fridge to detect a target in a room-temperature environment. However, reintroducing the signal—now mixed with substantial noise—back into the fridge poses cooling load challenges, typically requiring at least 50 dB attenuation in the input lines. A potential solution is to implement a narrow-band bandpass filter to reduce total noise power before feeding the signal back into the phase-conjugator.

Another critical requirement for future QI implementation is the development of efficient microwave photon counters capable of handling large photon numbers without saturation. This work opens opportunities for advancing existing quantum microwave photon counters or developing a high-dynamic-range cryogenic radiometer.

Finally, achieving higher purity squeezing remains essential for enhancing quantum advantage in QI. Encouragingly, recent research efforts suggest promising advancements in this direction $[ASJ^+25]$, paving the way for more robust and scalable QI implementations in the future.

Bibliography

- [AC91] P Alsing and HJ Carmichael. Spontaneous dressed-state polarization of a coupled atom and cavity mode. *Quantum Optics: Journal of the European Optical Society Part B*, 3(1):13, 1991.
- [AKD13] Baleegh Abdo, Archana Kamal, and Michel Devoret. Nondegenerate three-wave mixing with the josephson ring modulator. *Phys. Rev. B*, 87:014508, Jan 2013.
- [AL86] D. V. Averin and K. K. Likharev. Coulomb blockade of single-electron tunneling, and coherent oscillations in small tunnel junctions. *Journal of Low Temperature Physics*, 62(3):345–373, Feb 1986.
- [Alaa] AlazarTech. ATS9371 User Manual.
- [Alab] AlazarTech. ATS9870 User Manual.
- [AMM09] Michael A Armen, Anthony E Miller, and Hideo Mabuchi. Spontaneous dressed-state polarization in the strong driving regime of cavity qed. *Physical review letters*, 103(17):173601, 2009.
- [AOGL12] Cenap Ates, Beatriz Olmos, Juan P. Garrahan, and Igor Lesanovsky. Dynamical phases and intermittency of the dissipative quantum ising model. *Phys. Rev. A*, 85:043620, Apr 2012.
- [ASJ⁺25] Baleegh Abdo, William Shanks, Oblesh Jinka, J. R. Rozen, and Jason Orcutt. Teleportation and entanglement swapping of continuous quantum variables of microwave radiation. *arXiv preprint arXiv:2501.05537*, 2025.
- [Ass23] Dassonneville R. Peronnin T. Bienfait A. Huard B. Assouly, R. Quantum advantage in microwave quantum radar. *Nat. Phys.*, 19:1418–1422, Jun 2023.
- [BCK⁺09] Lev S. Bishop, J. M. Chow, Jens Koch, A. A. Houck, M. H. Devoret, E. Thuneberg, S. M. Girvin, and R. J. Schoelkopf. Nonlinear response of the vacuum rabi resonance. *Nature Physics*, 5(2):105–109, Feb 2009.
- [BGB11] Félix Beaudoin, Jay M. Gambetta, and A. Blais. Dissipation and ultrastrong coupling in circuit qed. *Phys. Rev. A*, 84:043832, Oct 2011.
- [BGBE10] Kristian Baumann, Christine Guerlin, Ferdinand Brennecke, and Tilman Esslinger. Dicke quantum phase transition with a superfluid gas in an optical cavity. *nature*, 464(7293):1301–1306, 2010.
- [BGGW21] Alexandre Blais, Arne L. Grimsmo, S. M. Girvin, and Andreas Wallraff. Circuit quantum electrodynamics. *Rev. Mod. Phys.*, 93:025005, May 2021.

- [BGW+15] Shabir Barzanjeh, Saikat Guha, Christian Weedbrook, David Vitali, Jeffrey H. Shapiro, and Stefano Pirandola. Microwave quantum illumination. *Phys. Rev. Lett.*, 114:080503, Feb 2015.
- [BHIW86] J. C. Bergquist, Randall G. Hulet, Wayne M. Itano, and D. J. Wineland. Observation of quantum jumps in a single atom. *Phys. Rev. Lett.*, 57:1699–1702, Oct 1986.
- [BLS+11] D. Bozyigit, C. Lang, L. Steffen, J. M. Fink, C. Eichler, M. Baur, R. Bianchetti, P. J. Leek, S. Filipp, M. P. da Silva, A. Blais, and A. Wallraff. Antibunching of microwave-frequency photons observed in correlation measurements using linear detectors. *Nature Physics*, 7(2):154–158, Feb 2011.
- [BMF⁺25] Guillaume Beaulieu, Fabrizio Minganti, Simone Frasca, Vincenzo Savona, Simone Felicetti, Roberto Di Candia, and Pasquale Scarlino. Observation of first- and second-order dissipative phase transitions in a two-photon driven kerr resonator. *Nature Communications*, 16(1):1954, Mar 2025.
- [BMR+22] C. Berdou, A. Murani, U. Reglade, W. C. Smith, M. Villiers, J. Palomo, M. Rosticher, A. Denis, P. Morfin, M. Delbecq, T. Kontos, N. Pankratova, F. Rautschke, T. Peronnin, L. A. Sellem, P. Rouchon, A. Sarlette, M. Mirrahimi, P. Campagne-Ibarcq, S. Jezouin, R. Lescanne, and Z. Leghtas. One hundred second bit-flip time in a two-photon dissipative oscillator, 2022.
- [BP07] Heinz-Peter Breuer and Francesco Petruccione. *The theory of open quantum systems*. Oxford University Press, January 2007.
- [BPVF20] S. Barzanjeh, S. Pirandola, D. Vitali, and J. M. Fink. Microwave quantum illumination using a digital receiver. *Science Advances*, 6(19):eabb0451, 2020.
- [BSKM⁺96] Michel Brune, F Schmidt-Kaler, Abdelhamid Maali, J Dreyer, E Hagley, JM Raimond, and S Haroche. Quantum rabi oscillation: A direct test of field quantization in a cavity. *Physical review letters*, 76(11):1800, 1996.
- [BTP+21] Paul Brookes, Giovanna Tancredi, Andrew D. Patterson, Joseph Rahamim, Martina Esposito, Themistoklis K. Mavrogordatos, Peter J. Leek, Eran Ginossar, and Marzena H. Szymanska. Critical slowing down in circuit quantum electrodynamics. *Science Advances*, 7(21):eabe9492, 2021.
- [BvL05] Samuel L. Braunstein and Peter van Loock. Quantum information with continuous variables. *Rev. Mod. Phys.*, 77:513–577, Jun 2005.
- [BW20] Jérôme Bourassa and Christopher M. Wilson. Progress toward an all-microwave quantum illumination radar. *IEEE Aerospace and Electronic Systems Magazine*, 35(11):58–69, 2020.
- [Car15] H. J. Carmichael. Breakdown of photon blockade: A dissipative quantum phase transition in zero dimensions. *Phys. Rev. X*, 5:031028, Sep 2015.
- [Cav81] Carlton M. Caves. Quantum-mechanical noise in an interferometer. *Phys. Rev. D*, 23:1693–1708, Apr 1981.
- [Cav82] Carlton M. Caves. Quantum limits on noise in linear amplifiers. *Phys. Rev. D*, 26:1817–1839, Oct 1982.

- [CBY⁺21] Jonathan B. Curtis, Igor Boettcher, Jeremy T. Young, Mohammad F. Maghrebi, Howard Carmichael, Alexey V. Gorshkov, and Michael Foss-Feig. Critical theory for the breakdown of photon blockade. *Phys. Rev. Research*, 3:023062, Apr 2021.
- [CCF⁺05] Luca Capriotti, Alessandro Cuccoli, Andrea Fubini, Valerio Tognetti, and Ruggero Vaia. Dissipation-driven phase transition in two-dimensional josephson arrays. *Physical review letters*, 94(15):157001, 2005.
- [CFC17] W. Casteels, R. Fazio, and C. Ciuti. Critical dynamical properties of a first-order dissipative phase transition. *Phys. Rev. A*, 95:012128, Jan 2017.
- [CGB+10] I Chiorescu, N Groll, Sylvain Bertaina, T Mori, and S Miyashita. Magnetic strong coupling in a spin-photon system and transition to classical regime. *Physical Review B*, 82(2):024413, 2010.
- [Cor21] Intel Corporation. Intel integrated performance primitives (intel ipp). https://www.intel.com/content/www/us/en/developer/tools/oneapi/ipp.html, 2021.
- [CRW+13] C. Carr, R. Ritter, C. G. Wade, C. S. Adams, and K. J. Weatherill. Nonequilibrium phase transition in a dilute rydberg ensemble. *Phys. Rev. Lett.*, 111:113901, Sep 2013.
- [CS85] Carlton M. Caves and Bonny L. Schumaker. New formalism for two-photon quantum optics. i. quadrature phases and squeezed states. *Phys. Rev. A*, 31:3068–3092, May 1985.
- [CSLBC16] W. Casteels, F. Storme, A. Le Boité, and C. Ciuti. Power laws in the dynamic hysteresis of quantum nonlinear photonic resonators. *Phys. Rev. A*, 93:033824, Mar 2016.
- [CVB⁺19] C. W. Sandbo Chang, A. M. Vadiraj, J. Bourassa, B. Balaji, and C. M. Wilson. Quantum-enhanced noise radar. *Applied Physics Letters*, 114(11):112601, 03 2019.
- [DCMP+23] R Di Candia, F Minganti, KV Petrovnin, GS Paraoanu, and S Felicetti. Critical parametric quantum sensing. *npj Quantum Information*, 9(1):23, 2023.
- [DGCZ00] Lu-Ming Duan, G. Giedke, J. I. Cirac, and P. Zoller. Inseparability criterion for continuous variable systems. *Phys. Rev. Lett.*, 84:2722–2725, Mar 2000.
- [DKSanM21] Galbadrakh Dagvadorj, Michał Kulczykowski, Marzena H. Szymańska, and Michał Matuszewski. First-order dissipative phase transition in an exciton-polariton condensate. *Phys. Rev. B*, 104:165301, Oct 2021.
- [DMK+08] Sebastian Diehl, A Micheli, A Kantian, B Kraus, HP Büchler, and P Zoller. Quantum states and phases in driven open quantum systems with cold atoms. *Nature Physics*, 4(11):878–883, 2008.
- [DMS17] Kamanasish Debnath, Eduardo Mascarenhas, and Vincenzo Savona. Nonequilibrium photonic transport and phase transition in an array of optical cavities. New Journal of Physics, 19(11):115006, 2017.

- [DRT11] M Delanty, S Rebić, and J Twamley. Superradiance and phase multistability in circuit quantum electrodynamics. *New Journal of Physics*, 13(5):053032, may 2011.
- [DTM⁺10] Sebastian Diehl, Andrea Tomadin, Andrea Micheli, Rosario Fazio, and Peter Zoller. Dynamical phase transitions and instabilities in open atomic many-body systems. *Physical review letters*, 105(1):015702, 2010.
- [DVD15] András Dombi, András Vukics, and Peter Domokos. Bistability effect in the extreme strong coupling regime of the jaynes-cummings model. *The European Physical Journal D*, 69(3):60, Mar 2015.
- [DW80] PD Drummond and DF Walls. Quantum theory of optical bistability. i. nonlinear polarisability model. *Journal of Physics A: Mathematical and General*, 13(2):725, 1980.
- [Dyk12] Mark Dykman. Fluctuating nonlinear oscillators: From nanomechanics to quantum superconducting circuits. Oxford University Press, July 2012.
- [EBL⁺11] C. Eichler, D. Bozyigit, C. Lang, L. Steffen, J. Fink, and A. Wallraff. Experimental state tomography of itinerant single microwave photons. *Phys. Rev. Lett.*, 106:220503, Jun 2011.
- [ES10] Baris I. Erkmen and Jeffrey H. Shapiro. Ghost imaging: from quantum to classical to computational. *Adv. Opt. Photon.*, 2(4):405–450, Dec 2010.
- [EW14] Christopher Eichler and Andreas Wallraff. Controlling the dynamic range of a josephson parametric amplifier. *EPJ Quantum Technology*, 1(1):2, Jan 2014.
- [FDLR⁺19] P. Forn-Díaz, L. Lamata, E. Rico, J. Kono, and E. Solano. Ultrastrong coupling regimes of light-matter interaction. *Rev. Mod. Phys.*, 91:025005, Jun 2019.
- [FDV+17] J. M. Fink, A. Dombi, A. Vukics, A. Wallraff, and P. Domokos. Observation of the photon-blockade breakdown phase transition. *Phys. Rev. X*, 7:011012, Jan 2017.
- [FGB⁺08] JM Fink, M Göppl, M Baur, R Bianchetti, Peter J Leek, Alexandre Blais, and Andreas Wallraff. Climbing the jaynes–cummings ladder and observing its nonlinearity in a cavity ged system. *Nature*, 454(7202):315–318, 2008.
- [FLP17a] Samuel Fernández-Lorenzo and Diego Porras. Quantum sensing close to a dissipative phase transition: Symmetry breaking and criticality as metrological resources. *Phys. Rev. A*, 96:013817, Jul 2017.
- [FLP17b] Samuel Fernández-Lorenzo and Diego Porras. Quantum sensing close to a dissipative phase transition: Symmetry breaking and criticality as metrological resources. *Physical Review A*, 96(1):013817, 2017.
- [FRM+12] E. Flurin, N. Roch, F. Mallet, M. H. Devoret, and B. Huard. Generating entangled microwave radiation over two transmission lines. *Phys. Rev. Lett.*, 109:183901, Oct 2012.

- [FRMF⁺21] Francesco Ferri, Rodrigo Rosa-Medina, Fabian Finger, Nishant Dogra, Matteo Soriente, Oded Zilberberg, Tobias Donner, and Tilman Esslinger. Emerging dissipative phases in a superradiant quantum gas with tunable decay. *Phys. Rev. X*, 11:041046, Dec 2021.
- [FSH⁺18] Thomas Fink, Anne Schade, Sven Höfling, Christian Schneider, and Ataç Imamoglu. Signatures of a dissipative phase transition in photon correlation measurements. *Nature Physics*, 14(4):365–369, Apr 2018.
- [FSL⁺17] Mattias Fitzpatrick, Neereja M. Sundaresan, Andy C. Y. Li, Jens Koch, and Andrew A. Houck. Observation of a dissipative phase transition in a one-dimensional circuit qed lattice. *Phys. Rev. X*, 7:011016, Feb 2017.
- [FSS+10] J. M. Fink, L. Steffen, P. Studer, Lev S. Bishop, M. Baur, R. Bianchetti, D. Bozyigit, C. Lang, S. Filipp, P. J. Leek, and A. Wallraff. Quantum-to-classical transition in cavity quantum electrodynamics. *Phys. Rev. Lett.*, 105:163601, Oct 2010.
- [GB18] Jan Gelhausen and Michael Buchhold. Dissipative dicke model with collective atomic decay: Bistability, noise-driven activation, and the nonthermal first-order superradiance transition. *Phys. Rev. A*, 97:023807, Feb 2018.
- [GBA⁺19] A. Grimm, F. Blanchet, R. Albert, J. Leppäkangas, S. Jebari, D. Hazra, F. Gustavo, J.-L. Thomassin, E. Dupont-Ferrier, F. Portier, and M. Hofheinz. Bright on-demand source of antibunched microwave photons based on inelastic cooper pair tunneling. *Phys. Rev. X*, 9:021016, Apr 2019.
- [GBK⁺20] Louis Garbe, Matteo Bina, Arne Keller, Matteo GA Paris, and Simone Felicetti. Critical quantum metrology with a finite-component quantum phase transition. *Physical review letters*, 124(12):120504, 2020.
- [GC85] C. W. Gardiner and M. J. Collett. Input and output in damped quantum systems: Quantum stochastic differential equations and the master equation. *Phys. Rev.* A, 31:3761–3774, Jun 1985.
- [GE09] Saikat Guha and Baris I. Erkmen. Gaussian-state quantum-illumination receivers for target detection. *Phys. Rev. A*, 80:052310, Nov 2009.
- [GJC18] R. Gutiérrez-Jáuregui and H. J. Carmichael. Dissipative quantum phase transitions of light in a generalized jaynes-cummings-rabi model. *Phys. Rev. A*, 98:023804, Aug 2018.
- [Gla63] Roy J. Glauber. Coherent and incoherent states of the radiation field. *Phys. Rev.*, 131:2766–2788, Sep 1963.
- [GMTP20] T. Gregory, P.-A. Moreau, E. Toninelli, and M. J. Padgett. Imaging through noise with quantum illumination. *Science Advances*, 6(6):eaay2652, 2020.
- [HBZC19] Toni L. Heugel, Matteo Biondi, Oded Zilberberg, and R. Chitra. Quantum transducer using a parametric driven-dissipative phase transition. *Phys. Rev. Lett.*, 123:173601, Oct 2019.

- [HEOL19] Ryo Hanai, Alexander Edelman, Yoji Ohashi, and Peter B. Littlewood. Non-hermitian phase transition from a polariton bose-einstein condensate to a photon laser. *Phys. Rev. Lett.*, 122:185301, May 2019.
- [HP16] Myung-Joong Hwang and Martin B. Plenio. Quantum phase transition in the finite Jaynes-Cummings lattice systems. *Phys. Rev. Lett.*, 117:123602, Sep 2016.
- [HPK⁺23] Farid Hassani, Matilda Peruzzo, LN Kapoor, Andrea Trioni, Martin Zemlicka, and Johannes M Fink. Inductively shunted transmons exhibit noise insensitive plasmon states and a fluxon decay exceeding 3 hours. *Nature Communications*, 14(1):3968, 2023.
- [HPP15] Myung-Joong Hwang, Ricardo Puebla, and Martin B. Plenio. Quantum phase transition and universal dynamics in the Rabi model. *Phys. Rev. Lett.*, 115:180404, Oct 2015.
- [HR06] Serge Haroche and Jean-Michel Raimond. *Exploring the Quantum: Atoms, Cavities, and Photons.* Oxford University Press, Aug 2006.
- [HRP18] Myung-Joong Hwang, Peter Rabl, and Martin B. Plenio. Dissipative phase transition in the open quantum rabi model. *Phys. Rev. A*, 97:013825, Jan 2018.
- [HSJ⁺08] A. A. Houck, J. A. Schreier, B. R. Johnson, J. M. Chow, Jens Koch, J. M. Gambetta, D. I. Schuster, L. Frunzio, M. H. Devoret, S. M. Girvin, and R. J. Schoelkopf. Controlling the spontaneous emission of a superconducting transmon qubit. *Phys. Rev. Lett.*, 101:080502, Aug 2008.
- [lbgSWD97] A. Imamoglu, H. Schmidt, G. Woods, and M. Deutsch. Strongly interacting photons in a nonlinear cavity. *Phys. Rev. Lett.*, 79:1467–1470, Aug 1997.
- [KFSP24] Athena Karsa, Alasdair Fletcher, Gaetana Spedalieri, and Stefano Pirandola. Quantum illumination and quantum radar: a brief overview. *Reports on Progress in Physics*, 87(9):094001, aug 2024.
- [KGI+12] E. M. Kessler, G. Giedke, A. Imamoglu, S. F. Yelin, M. D. Lukin, and J. I. Cirac. Dissipative phase transition in a central spin system. *Phys. Rev. A*, 86:012116, Jul 2012.
- [KKM+15] H. S. Ku, W. F. Kindel, F. Mallet, S. Glancy, K. D. Irwin, G. C. Hilton, L. R. Vale, and K. W. Lehnert. Generating and verifying entangled itinerant microwave fields with efficient and independent measurements. *Phys. Rev. A*, 91:042305, Apr 2015.
- [KNV23] Árpád Kurkó, Nikolett Német, and András Vukics. Is the photon-blockade breakdown a quantum effect? a neoclassical story. *arXiv preprint arXiv:2310.08388*, 2023.
- [KRM+10] Jacek Kasprzak, S Reitzenstein, Egor A Muljarov, C Kistner, C Schneider, M Strauss, S Höfling, A Forchel, and W Langbein. Up on the jaynes-cummings ladder of a quantum-dot/microcavity system. *Nature materials*, 9(4):304–308, 2010.

- [KV19] Miklós Kornyik and András Vukics. The monte carlo wave-function method: A robust adaptive algorithm and a study in convergence. *Computer Physics Communications*, 238:88–101, 2019.
- [KYG+07] Jens Koch, Terri M. Yu, Jay Gambetta, A. A. Houck, D. I. Schuster, J. Majer, Alexandre Blais, M. H. Devoret, S. M. Girvin, and R. J. Schoelkopf. Chargeinsensitive qubit design derived from the cooper pair box. *Phys. Rev. A*, 76:042319, Oct 2007.
- [Lan14] Christian Lang. Quantum Microwave Radiation and its Interference Characterized by Correlation Function Measurements in Circuit Quantum Electrodynamics. PhD thesis, ETH Zurich, 2014.
- [LBE+11] C. Lang, D. Bozyigit, C. Eichler, L. Steffen, J. M. Fink, A. A. Abdumalikov, M. Baur, S. Filipp, M. P. da Silva, A. Blais, and A. Wallraff. Observation of resonant photon blockade at microwave frequencies using correlation function measurements. *Phys. Rev. Lett.*, 106:243601, Jun 2011.
- [LBOC13] Alexandre Le Boité, Giuliano Orso, and Cristiano Ciuti. Steady-state phases and tunneling-induced instabilities in the driven dissipative bose-hubbard model. *Phys. Rev. Lett.*, 110:233601, Jun 2013.
- [LBSC⁺18] David Luong, Bhashyam Balaji, Chung Wai Sandbo Chang, Vadiraj Manjunath Ananthapadmanabha Rao, and Christopher Wilson. Microwave quantum radar: An experimental validation. In *2018 International Carnahan Conference on Security Technology (ICCST)*, pages 1–5, 2018.
- [LCB+22] Zejian Li, Ferdinand Claude, Thomas Boulier, Elisabeth Giacobino, Quentin Glorieux, Alberto Bramati, and Cristiano Ciuti. Dissipative phase transition with driving-controlled spatial dimension and diffusive boundary conditions. *Phys. Rev. Lett.*, 128:093601, Feb 2022.
- [LCP20] Johannes Lang, Darrick Chang, and Francesco Piazza. Interaction-induced transparency for strong-coupling polaritons. *Phys. Rev. Lett.*, 125:133604, Sep 2020.
- [LDA+20] Raphaël Lescanne, Samuel Deléglise, Emanuele Albertinale, Ulysse Réglade, Thibault Capelle, Edouard Ivanov, Thibaut Jacqmin, Zaki Leghtas, and Emmanuel Flurin. Irreversible qubit-photon coupling for the detection of itinerant microwave photons. *Phys. Rev. X*, 10:021038, May 2020.
- [LDB⁺19] David Luong, Anthony Damini, Bhashyam Balaji, C. W. Sandbo Chang, A. M. Vadiraj, and Christopher Wilson. A quantum-enhanced radar prototype. In *2019 IEEE Radar Conference (RadarConf)*, pages 1–6, 2019.
- [LI17] Jonas Larson and Elinor K Irish. Some remarks on 'superradiant' phase transitions in light-matter systems. *Journal of Physics A: Mathematical and Theoretical*, 50(17):174002, 2017.
- [Llo08] Seth Lloyd. Enhanced sensitivity of photodetection via quantum illumination. *Science*, 321(5895):1463–1465, 2008.

- [LRBD+13] E. D. Lopaeva, I. Ruo Berchera, I. P. Degiovanni, S. Olivares, G. Brida, and M. Genovese. Experimental realization of quantum illumination. *Phys. Rev. Lett.*, 110:153603, Apr 2013.
- [LSHO16] Ralf Labouvie, Bodhaditya Santra, Simon Heun, and Herwig Ott. Bistability in a driven-dissipative superfluid. *Phys. Rev. Lett.*, 116:235302, Jun 2016.
- [LTN⁺17] F. Letscher, O. Thomas, T. Niederprüm, M. Fleischhauer, and H. Ott. Bistability versus metastability in driven dissipative rydberg gases. *Phys. Rev. X*, 7:021020, May 2017.
- [Lyn97] Peter Lynch. The dolph-chebyshev window: A simple optimal filter. *Monthly Weather Review*, 125(4):655 660, 1997.
- [Lyo96] Richard G. Lyons. Understanding Digital Signal Processing. Pearson Education, Inc., Rights and Contracts Department, 501 Boylston Street, Suite 900, Boston, MA 02116, USA, 1996.
- [MBBC18] Fabrizio Minganti, Alberto Biella, Nicola Bartolo, and Cristiano Ciuti. Spectral theory of liouvillians for dissipative phase transitions. *Phys. Rev. A*, 98:042118, Oct 2018.
- [MGM+18] P. R. Muppalla, O. Gargiulo, S. I. Mirzaei, B. Prasanna Venkatesh, M. L. Juan, L. Grünhaupt, I. M. Pop, and G. Kirchmair. Bistability in a mesoscopic josephson junction array resonator. *Phys. Rev. B*, 97:024518, Jan 2018.
- [Mit89] R.L. Mitchell. Creating complex signal samples from a band-limited real signal. IEEE Transactions on Aerospace and Electronic Systems, 25(3):425–427, 1989.
- [MJYWX22] Nayan E Myerson-Jain, Stephen Yan, David Weld, and Cenke Xu. Construction of fractal order and phase transition with rydberg atoms. *Physical Review Letters*, 128(1):017601, 2022.
- [MLD⁺14] Matteo Marcuzzi, Emanuele Levi, Sebastian Diehl, Juan P Garrahan, and Igor Lesanovsky. Universal nonequilibrium properties of dissipative rydberg gases. *Physical review letters*, 113(21):210401, 2014.
- [Mol69] B. R. Mollow. Power spectrum of light scattered by two-level systems. *Phys. Rev.*, 188:1969–1975, Dec 1969.
- [MTE+17] Th. K. Mavrogordatos, G. Tancredi, M. Elliott, M. J. Peterer, A. Patterson, J. Rahamim, P. J. Leek, E. Ginossar, and M. H. Szymańska. Simultaneous bistability of a qubit and resonator in circuit quantum electrodynamics. *Phys. Rev. Lett.*, 118:040402, Jan 2017.
- [MVS+14] N. Malossi, M. M. Valado, S. Scotto, P. Huillery, P. Pillet, D. Ciampini, E. Arimondo, and O. Morsch. Full counting statistics and phase diagram of a dissipative rydberg gas. *Phys. Rev. Lett.*, 113:023006, Jul 2014.
- [NG20] Ranjith Nair and Mile Gu. Fundamental limits of quantum illumination. *Optica*, 7(7):771–774, Jul 2020.

- [NKSD10] D Nagy, G Kónya, G Szirmai, and P Domokos. Dicke-model phase transition in the quantum motion of a bose-einstein condensate in an optical cavity. *Physical review letters*, 104(13):130401, 2010.
- [NSD86] Warren Nagourney, Jon Sandberg, and Hans Dehmelt. Shelved optical electron amplifier: Observation of quantum jumps. *Phys. Rev. Lett.*, 56:2797–2799, Jun 1986.
- [OKTT21] Ryutaro Ohira, Shota Kume, Hiroki Takahashi, and Kenji Toyoda. Polariton blockade in the jaynes–cummings–hubbard model with trapped ions. *Quantum Science and Technology*, 6(2):024015, 2021.
- [OMGW17] Vincent R. Overbeck, Mohammad F. Maghrebi, Alexey V. Gorshkov, and Hendrik Weimer. Multicritical behavior in dissipative ising models. *Phys. Rev. A*, 95:042133, Apr 2017.
- [PDK⁺18] I Pietikäinen, Sergey Danilin, KS Kumar, J Tuorila, and GS Paraoanu. Multilevel effects in a driven generalized rabi model. *Journal of Low Temperature Physics*, 191:354–364, 2018.
- [PSB+11] Hanhee Paik, D. I. Schuster, Lev S. Bishop, G. Kirchmair, G. Catelani, A. P. Sears, B. R. Johnson, M. J. Reagor, L. Frunzio, L. I. Glazman, S. M. Girvin, M. H. Devoret, and R. J. Schoelkopf. Observation of high coherence in josephson junction qubits measured in a three-dimensional circuit qed architecture. *Phys. Rev. Lett.*, 107:240501, Dec 2011.
- [PSR⁺12] András Pályi, P. R. Struck, Mark Rudner, Karsten Flensberg, and Guido Burkard. Spin-orbit-induced strong coupling of a single spin to a nanomechanical resonator. *Phys. Rev. Lett.*, 108:206811, May 2012.
- [PT10] V Peano and M Thorwart. Dynamical bistability in the driven circuit qed. *EPL* (*Europhysics Letters*), 89(1):17008, 2010.
- [PWP+24] Kirill Petrovnin, Jiaming Wang, Michael Perelshtein, Pertti Hakonen, and Gheorghe Sorin Paraoanu. Microwave photon detection at parametric criticality. *PRX Quantum*, 5:020342, May 2024.
- [RacTM09] Stojan Rebić, Jason Twamley, and Gerard J. Milburn. Giant kerr nonlinearities in circuit quantum electrodynamics. *Phys. Rev. Lett.*, 103:150503, Oct 2009.
- [Rad84] Charles M. Rader. A simple method for sampling in-phase and quadrature components. *IEEE Transactions on Aerospace and Electronic Systems*, AES-20(6):821–824, 1984.
- [RCS+17] S. R. K. Rodriguez, W. Casteels, F. Storme, N. Carlon Zambon, I. Sagnes, L. Le Gratiet, E. Galopin, A. Lemaître, A. Amo, C. Ciuti, and J. Bloch. Probing a dissipative phase transition via dynamical optical hysteresis. *Phys. Rev. Lett.*, 118:247402, Jun 2017.
- [RDB18] Dietrich Roscher, Sebastian Diehl, and Michael Buchhold. Phenomenology of first-order dark-state phase transitions. *Phys. Rev. A*, 98:062117, Dec 2018.

- [RNHY20] Florentin Reiter, Thanh Long Nguyen, Jonathan P. Home, and Susanne F. Yelin. Cooperative breakdown of the oscillator blockade in the dicke model. *Phys. Rev. Lett.*, 125:233602, Nov 2020.
- [RPS⁺23] Elena S. Redchenko, Alexander V. Poshakinskiy, Riya Sett, Martin Žemlička, Alexander N. Poddubny, and Johannes M. Fink. Tunable directional photon scattering from a pair of superconducting qubits. *Nature Communications*, 14(1):2998, May 2023.
- [RWW18] Meghana Raghunandan, Jörg Wrachtrup, and Hendrik Weimer. High-density quantum sensing with dissipative first order transitions. *Physical Review Letters*, 120(15):150501, 2018.
- [RZicvcv⁺25] E. S. Redchenko, M. Zens, M. Žemlička, M. Peruzzo, F. Hassani, R. Sett, P. Zieliński, H. S. Dhar, D. O. Krimer, S. Rotter, and J. M. Fink. Observation of collapse and revival in a superconducting atomic frequency comb. *Phys. Rev. Lett.*, 134:063601, Feb 2025.
- [RZSDC23] Maximilian Reichert, Quntao Zhuang, Jeffrey H. Shapiro, and Roberto Di Candia. Quantum illumination with a hetero-homodyne receiver and sequential detection. *Phys. Rev. Appl.*, 20:014030, Jul 2023.
- [Sav17] Vincenzo Savona. Spontaneous symmetry breaking in a quadratically driven nonlinear photonic lattice. *Phys. Rev. A*, 96:033826, Sep 2017.
- [SBF10] M. Peruzzo M. Wulf D. P. Lewis G. Arnold S. Barzanjeh, E. S. Redchenko and J. M. Fink. Phase-preserving amplification near the quantum limit with a josephson ring modulator. *Nature*, 465:64–68, 2010.
- [SBF19] M. Peruzzo M. Wulf D. P. Lewis G. Arnold S. Barzanjeh, E. S. Redchenko and J. M. Fink. Stationary entangled radiation from micromechanical motion. *Nature*, 570:480–483, 2019.
- [SC88] C.M. Savage and H.J. Carmichael. Single atom optical bistability. *IEEE Journal of Quantum Electronics*, 24(8):1495–1498, 1988.
- [SGKP20] Kevin C. Stitely, Andrus Giraldo, Bernd Krauskopf, and Scott Parkins. Nonlinear semiclassical dynamics of the unbalanced, open dicke model. *Phys. Rev. Research*, 2:033131, Jul 2020.
- [Sha20] Jeffrey H. Shapiro. The quantum illumination story. *IEEE Aerospace and Electronic Systems Magazine*, 35(4):8–20, 2020.
- [SHA+21] Matteo Soriente, Toni L. Heugel, Keita Arimitsu, R. Chitra, and Oded Zilberberg. Distinctive class of dissipation-induced phase transitions and their universal characteristics. *Phys. Rev. Research*, 3:023100, May 2021.
- [SHK+08] J. A. Schreier, A. A. Houck, Jens Koch, D. I. Schuster, B. R. Johnson, J. M. Chow, J. M. Gambetta, J. Majer, L. Frunzio, M. H. Devoret, S. M. Girvin, and R. J. Schoelkopf. Suppressing charge noise decoherence in superconducting charge qubits. *Phys. Rev. B*, 77:180502, May 2008.

- [SHP+21] Rhine Samajdar, Wen Wei Ho, Hannes Pichler, Mikhail D Lukin, and Subir Sachdev. Quantum phases of rydberg atoms on a kagome lattice. *Proceedings of the National Academy of Sciences*, 118(4), 2021.
- [SHP+24] Riya Sett, Farid Hassani, Duc Phan, Shabir Barzanjeh, Andras Vukics, and Johannes M. Fink. Emergent macroscopic bistability induced by a single superconducting qubit. *PRX Quantum*, 5:010327, Feb 2024.
- [SHS+07] D. I. Schuster, A. A. Houck, J. A. Schreier, A. Wallraff, J. M. Gambetta, A. Blais, L. Frunzio, J. Majer, B. Johnson, M. H. Devoret, S. M. Girvin, and R. J. Schoelkopf. Resolving photon number states in a superconducting circuit. *Nature*, 445(7127):515–518, Feb 2007.
- [SL09] Jeffrey H Shapiro and Seth Lloyd. Quantum illumination versus coherent-state target detection. *New Journal of Physics*, 11(6):063045, jun 2009.
- [SLHGR⁺17] M. Sanz, U. Las Heras, J. J. García-Ripoll, E. Solano, and R. Di Candia. Quantum estimation methods for quantum illumination. *Phys. Rev. Lett.*, 118:070803, Feb 2017.
- [SPC+12] A. P. Sears, A. Petrenko, G. Catelani, L. Sun, Hanhee Paik, G. Kirchmair, L. Frunzio, L. I. Glazman, S. M. Girvin, and R. J. Schoelkopf. Photon shot noise dephasing in the strong-dispersive limit of circuit qed. *Phys. Rev. B*, 86:180504, Nov 2012.
- [SPC⁺22] Ross Shillito, Alexandru Petrescu, Joachim Cohen, Jackson Beall, Markus Hauru, Martin Ganahl, Adam G.M. Lewis, Guifre Vidal, and Alexandre Blais. Dynamics of transmon ionization. *Phys. Rev. Appl.*, 18:034031, Sep 2022.
- [SQH⁺23] R. Sahu, L. Qiu, W. Hease, G. Arnold, Y. Minoguchi, P. Rabl, and J. M. Fink. Entangling microwaves with light. *Science*, 380(6646):718–721, 2023.
- [SSDP+20] Kubilay Savci, Andrew G. Stove, Francesco De Palo, Ahmet Yasin Erdogan, Gaspare Galati, Konstantin A. Lukin, Sergii Lukin, Paulo Marques, Gabriele Pavan, and Christoph Wasserzier. Noise radar—overview and recent developments. *IEEE Aerospace and Electronic Systems Magazine*, 35(9):8–20, 2020.
- [SSH+12] Gesine A. Steudle, Stefan Schietinger, David Höckel, Sander N. Dorenbos, Iman E. Zadeh, Valery Zwiller, and Oliver Benson. Measuring the quantum nature of light with a single source and a single detector. *Phys. Rev. A*, 86:053814, Nov 2012.
- [SZGH+16] Matti Silveri, Evan Zalys-Geller, Michael Hatridge, Zaki Leghtas, Michel H. Devoret, and S. M. Girvin. Theory of remote entanglement via quantum-limited phase-preserving amplification. *Phys. Rev. A*, 93:062310, Jun 2016.
- [TEG⁺08] Si-Hui Tan, Baris I. Erkmen, Vittorio Giovannetti, Saikat Guha, Seth Lloyd, Lorenzo Maccone, Stefano Pirandola, and Jeffrey H. Shapiro. Quantum illumination with gaussian states. *Phys. Rev. Lett.*, 101:253601, Dec 2008.
- [TFHE⁺19] Uwe Thiele, Tobias Frohoff-Hülsmann, Sebastian Engelnkemper, Edgar Knobloch, and Andrew J Archer. First order phase transitions and the thermodynamic limit. *New Journal of Physics*, 21(12):123021, 2019.

- [VDFD19] A. Vukics, A. Dombi, J. M. Fink, and P. Domokos. Finite-size scaling of the photon-blockade breakdown dissipative quantum phase transition. *Quantum*, 3:150, June 2019.
- [VMR⁺18] Filippo Vicentini, Fabrizio Minganti, Riccardo Rota, Giuliano Orso, and Cristiano Ciuti. Critical slowing down in driven-dissipative bose-hubbard lattices. *Phys. Rev. A*, 97:013853, Jan 2018.
- [Voj03] Matthias Vojta. Quantum phase transitions. *Reports on Progress in Physics*, 66(12):2069, 2003.
- [Vuk12] András Vukics. C++qedv2: The multi-array concept and compile-time algorithms in the definition of composite quantum systems. *Computer Physics Communications*, 183(6):1381–1396, 2012.
- [VWIC09] Frank Verstraete, Michael M Wolf, and J Ignacio Cirac. Quantum computation and quantum-state engineering driven by dissipation. *Nature physics*, 5(9):633–636, 2009.
- [WA92] P.D. West and M.D. Austin. Extracting in-phase and quadrature signal components from a bandlimited real signal using a closed form optimal (mse) halfband multirate filter design and its implementation on the motorola dsp56001/dsp56adc16. In [Proceedings] ICASSP-92: 1992 IEEE International Conference on Acoustics, Speech, and Signal Processing, volume 4, pages 685–688 vol.4, 1992.
- [WS19] Waltraut Wustmann and Vitaly Shumeiko. Parametric effects in circuit quantum electrodynamics. Low Temperature Physics, 45(8):848–869, 2019.
- [YJ19] Li-Ping Yang and Zubin Jacob. Engineering first-order quantum phase transitions for weak signal detection. *Journal of Applied Physics*, 126(17):174502, 2019.
- [ZMWS15] Zheshen Zhang, Sara Mouradian, Franco N. C. Wong, and Jeffrey H. Shapiro. Entanglement-enhanced sensing in a lossy and noisy environment. *Phys. Rev. Lett.*, 114:110506, Mar 2015.
- [ZRP+23] M. Zemlicka, E. Redchenko, M. Peruzzo, F. Hassani, A. Trioni, S. Barzanjeh, and J.M. Fink. Compact vacuum-gap transmon qubits: Selective and sensitive probes for superconductor surface losses. *Phys. Rev. Appl.*, 20:044054, Oct 2023.

APPENDIX A

Digitizer

There are two PCI Express Digitizers with two channels used in the laboratory till now - one is with 8-bit sampling (ATS9870) and the other one is with 12-bit sampling (ATS9371) - both with 1GS/s simultaneous real-time sampling rate on each input. These digitizers can be used in either Python or C++ versions. Let's briefly discuss some important features of the digitizers to be kept in mind while using it for data processing.

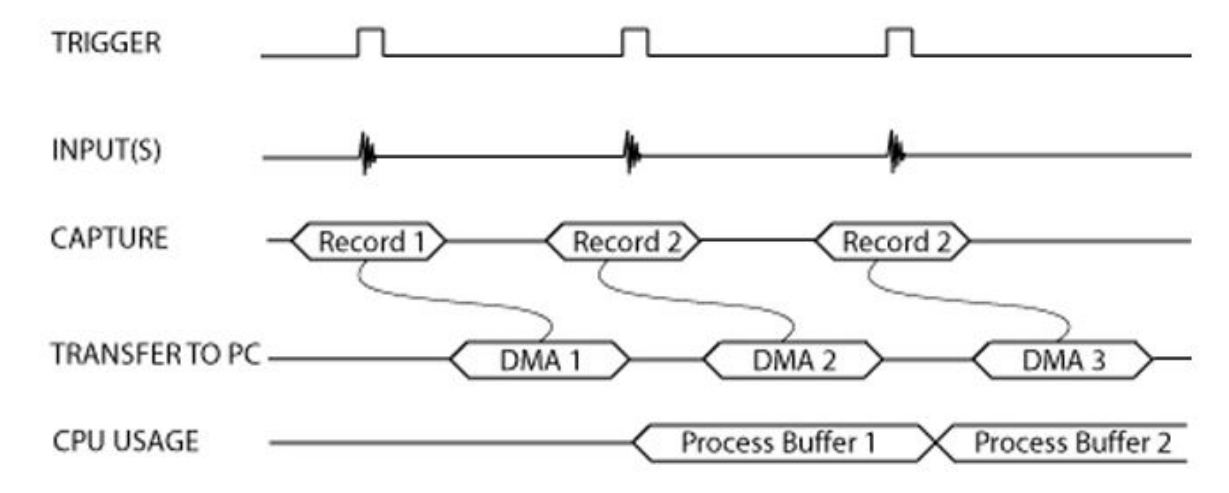
A.1 The Digitizer Hardware

Both ATS9870 and ATS9371 digitizers have one External Clock input (ECLK), two signal inputs (CH A and CH B), one trigger input (TRIG IN) to feed external trigger and one Auxiliary input and output port (AUX I/O). In our applications we don't use Aux I/O port.

External clock input. There are three types of external clock supported by both the digitizers - (i) Fast external clock; (ii) Slow external clock; and (iii) 10 MHz clock reference. We generally use 10 MHz clock reference from Rubidium clock to ECLK port. The 10 MHz reference produces 1 GHz sampling frequency in the digitizer. In ATS9870, lower sampling rate can be achieved by using decimation in the software. In ATS9371, the sampling rate is fixed at 1 GHz.

Analog signal inputs. Both the digitizers have two analog signal inputs CH A and CH B with 50Ω input impedance. Other than normal data acquisition through these two ports, they can also be used as trigger for the data acquisition. In ATS9870, these channels can be AC or DC coupled from software according to application requirements. But in ATS9371 the channels are DC-coupled only. AC coupling is very useful when the input signals have high DC component. Moreover, in ATS9870, the input range at these ports are ± 200 mV to ± 4 V, whereas in ATS9371, this range is fixed at ± 400 mV. Since we generally use low-noise amplifiers and post-IF amplifier before acquiring data with digitizer, the signal amplitude might be larger than ± 400 mV. In that case one can use attenuators on the signal path to acquire data by ATS9371 in correct volt range. So it is necessary to always choose proper volt range in ATS9870 and proper attenuation in signal path for ATS9371 so that the acquired data cannot get clipped and hence it produces wrong results in the end.

External trigger input. We apply external trigger generated from a DDG (Digital Delay Generator) required to acquire the data by the digitizer. The Ext trigger input has a fixed



NOTE 1: No Trigger Events Are Missed - Guaranteed

NOTE 2: Over 95% of CPU cycles are available for data processing

Figure A.1: Data acquisition with external trigger using dual-port memory [Alab] [Alaa]

input range of ± 5 V. Since the DDG output has high impedance, we apply ± 2.5 V which becomes ± 5 V at the output.

A.2 Data Acquisition with Digitizer

The advantage with these digitizers is that they have on-board dual port acquisition memory which works as very deep FIFO (First In First Out) and dual-DMA (Direct Memory Access) engine. It is particularly useful for capturing data from continuously occurring triggers as well as continuous data streaming to PC host memory. In most of the general digitizers, the basic throughput problem occurs due to the usage of single-port memory. It leads to the problem with that reading data from acquisition memory and data acquisition cannot occur in parallel. The whole process depends solely on the operating system response time. On the contrary, ATS9870 and ATS9371 use dual-port memory which enables the streaming rate of data to PC host memory at up to 1.4 - 1.6 GB/s depending on the motherboard of the host PC. In this case, capturing data and reading the captured data take place in parallel.

There are four types of data acquisition available with these digitizers -

- (i) Traditional AutoDMA
- (ii) No Pre-trigger (NPT) AsyncDMA
- (iii) Continuous AutoDMA
- (iv) Triggered streaming AutoDMA

We only used NPT AutoDMA since we generally didn't require pre-triggered data. Hence, we will discuss shortly about NPT AutoDMA data acquisition as below.

NPT AutoDMA only stores post-trigger data, which leads to optimized memory bandwidth. In this mode, the entire on-board memory works like a very deep FIFO. When the digitizer receives a trigger, it captures one record of data and stores in DMA of the digitizer. When it receives the next trigger it records the next record of data and stores in the second DMA

while the first DMA is already transfering its data to the host memory. With correct trigger and length of record (records per buffer) settings, the data capture and transfer of data to host memory continuously progress without missing any trigger as can be seen in Figure A.1.

A.3 Programming in C++ for data acquisition

Here, I will try to explain how the simple data acquisition task is written in C++ communicating both 8-bit and 12-bit digitizers. To be noted: they acquire data in different ways. The C++ code can found in gitlab repository of finkgroup/C-ATS Drivers. The data acquisition is written in 'cats_multithread.cpp'

A.3.1 Adopt Digitizer Settings

The first step is to adopt the digitizer setting according to what user wants. The user needs to input in VIP the following settings parameters -

- (i) **Decimation** The digitizers produce maximum 1 GHz sampling rate in order to acquire the digitized data every 1ns interval. Though in ATS9371, this sampling rate is fixed, in ATS9870, this sampling rate can be reduced by choosing decimation. If you select decimation let's say d then the sampling frequency of the digitizer will be 1/d GHz. For example if I select decimation to be 10, the sampling frequency will be 100 MHz and the digitizer will capture data point every 10ns.
- (ii) post trigger samples The number of data points to be acquired in one record. This size has to be a multiple of 64.
- (iii) records per buffer This is where, the user asks the digitizer how many records it will acquire per buffer. The digitizer acquire one record when it receives a trigger and it stores N records in one buffer. After capturing one record, it waits ffor the next trigger to arrive and again it captures the next record and so on. After capturing one buffer, the digitizer transfers the whole buffer to host memory.
- (iv) buffers per acquisition Here, the user instructs how many buffers (each buffer includes N records) to capture. So at the end, for example, if number of post trigger samples is pTs; number of records per buffer is rPB, and number of beffers per acquisition is bPA, the total number of records the digitizer capture is rPB \times bPA and the total number of data points is pTS \times rPB \times bPA.
- (v) Channels The user has to input if the digitizer will capture data from only one channel (either A or B) or both channels A and B.
- (vi) Volt range The voltage range in the selected input channels need to be declared. In the 8-bit digitizer ATS9870, the possible voltranges can be selected are $\pm 0.04, \pm 0.1, \pm 0.2, \pm 0.4, \pm 1.0, \pm 4.0$ Volts, whereas for 12-bit digitizer ATS9371, this voltage range is fixed at ± 0.4 volts.
- (vii) Coupling In ATS9870, we can choose AC or DC coupling at the input channels A and B, but for ATS9371, it is fixed at DC coupling.

The other parameters, we kept fixed like the external clock reference at 10 MHz, the trigger voltage at 5V with positive slope detection and trigger coupling type to be DC.

int acquireData(double* averageSignal, int averageLength, int rPB, int bPA,
 int pTS, int preTS, double channelAVolts, double channelBVolts, int
 chMask)

```
2 {
3
      int success = TRUE;
      U32 preTriggerSamples = 0;
4
5
      U32 postTriggerSamples = pTS;
      U32 recordsPerBuffer = rPB;
6
7
      U32 buffersPerAcquisition = bPA;
8
      U32 channelMask;
9
      HANDLE boardHandle = AlazarGetBoardBySystemID(1, 1);
10
      if (chMask == 0)
11
12
13
           channelBVolts = NULL;
           channelMask = CHANNEL_A;
14
15
      if (chMask == 1)
16
17
           channelAVolts = NULL;
           channelMask = CHANNEL B;
19
20
      if (chMask == 2)
21
           channelMask = CHANNEL_A | CHANNEL_B;
22
23
24
      int channelCount = 0;
      int channelsPerBoard = 2;
25
26
      for (int channel = 0; channel < channelsPerBoard; channel++)</pre>
27
           U32 channelId = 1U << channel;
28
           if (channelMask & channelId)
               channelCount++;
30
      }
31
32
33
      U8 bitsPerSample;
      U32 maxSamplesPerChannel;
34
35
      RETURN_CODE retCode = AlazarGetChannelInfo(boardHandle, &
      maxSamplesPerChannel, &bitsPerSample);
      if (retCode != ApiSuccess)
36
37
           printf("Error: AlazarGetChannelInfo failed -- %s\n",
38
      AlazarErrorToText (retCode));
39
           return FALSE;
40
```

Listing A.1: Adopt settings in Digitizer

A.3.2 Preparations before capturing data

Before starting capturing data, it is important to allocate proper dynamic memories to store the data. Since ATS9870 captures data in 8-bit, the memories assigned for data coming from this digitizer are of 8-bit length. But ATS9371 captures data in 12 bit, hence digitizing data with more bit-resolution (and hence better SNR), the data is packed in 16-bit and transferred to host memory. So for this digitizer, the memories are allocated with 16-bit long space. Moreover, we also set the "Flags" of which type of data acquisition we are going to use. In our case, we choose to use "ADMA_EXTERNAL_STARTCAPTURE" or "ADMA_NPT" or "ADMA_FIFO_ONLY_STREAMING".

```
1 U8 bitsPerSample;
2 U32 maxSamplesPerChannel;
```

```
3 RETURN_CODE retCode = AlazarGetChannelInfo(boardHandle, &
     maxSamplesPerChannel, &bitsPerSample);
4 if (retCode != ApiSuccess)
5 {
      printf("Error: AlazarGetChannelInfo failed -- %s\n", AlazarErrorToText(
     retCode));
7
     return 2;
8 }
9 float bytesPerSample = (float)((bitsPerSample + 7) / 8);
10 U32 samplesPerRecord = preTriggerSamples + postTriggerSamples;
11 U32 bytesPerRecord = (U32) (bytesPerSample * samplesPerRecord +
      0.5); // 0.5 compensates for double to integer conversion
13 U32 bytesPerBuffer = bytesPerRecord * recordsPerBuffer * channelCount;
14 U32 bufferIndex;
15 for (bufferIndex = 0; (bufferIndex < BUFFER_COUNT) && success; bufferIndex
     ++)
16 {
17
      BufferArray[bufferIndex] = (Ipp16u*)AlazarAllocBufferU16(boardHandle,
      bytesPerBuffer); // (U16*) AlazarAllocBufferU16 (boardHandle,
      bytesPerBuffer);
      if (BufferArray[bufferIndex] == NULL)
18
19
20
          printf("Error: Alloc %u bytes failed\n", bytesPerBuffer);
21
          success = 3;
22
23 }
24 if (averageSignal == NULL)
25 {
26
      printf("Error: Alloc %zu bytes failed\n", samplesPerRecord *
     channelCount * sizeof(double));
27
      success = 4;
28 }
29 else
30 {
      success = StartWorkerThreads(channelCount, inputRangeVolts, "AVERAGE",
31
      O, NULL, NULL, NULL, NULL);
32 }
33
34 Ipp64f* pAccRecord = NULL;
35 if (success)
36 {
      U32 bytesPerAccBuffer = samplesPerRecord * channelCount * sizeof(Ipp64f
37
      ) * ThreadCount;
      pAccRecord = ippsMalloc_64f(bytesPerAccBuffer);
38
39
      if (pAccRecord == NULL)
40
          printf("Error: Alloc %u bytes failed\n", bytesPerAccBuffer);
41
42
          success = 5;
43
      }
44 }
45
46 if (success)
47 {
      retCode = AlazarSetRecordSize(boardHandle, preTriggerSamples,
48
     postTriggerSamples);
49
      if (retCode != ApiSuccess)
50
      {
51
          printf("Error: AlazarSetRecordSize failed -- %s\n",
     AlazarErrorToText (retCode));
```

```
success = 6;
53
      }
54 }
55
56 if (success)
57 {
58
      U32 recordsPerAcquisition = recordsPerBuffer * buffersPerAcquisition;
59
      U32 admaFlags = ADMA_EXTERNAL_STARTCAPTURE | ADMA_NPT |
      ADMA_FIFO_ONLY_STREAMING;
60
      retCode = AlazarBeforeAsyncRead(boardHandle, channelMask, -(long)
61
      preTriggerSamples, samplesPerRecord, recordsPerBuffer,
      recordsPerAcquisition, admaFlags);
62
      if (retCode != ApiSuccess)
63
64
          printf("Error: AlazarBeforeAsyncRead failed -- %s\n",
65
      AlazarErrorToText (retCode));
          success = 7;
66
67
68 }
69
70 for (bufferIndex = 0; (bufferIndex < BUFFER_COUNT) && success; bufferIndex
      ++)
71
  {
      Ipp16u* pBuffer = BufferArray[bufferIndex]; //U16* pBuffer =
72
      BufferArray[bufferIndex];
      retCode = AlazarPostAsyncBuffer(boardHandle, pBuffer, bytesPerBuffer);
73
      if (retCode != ApiSuccess)
74
75
          printf("Error: AlazarPostAsyncBuffer %u failed -- %s\n",
76
      bufferIndex, AlazarErrorToText(retCode));
          success = 8;
77
78
      }
79
```

Listing A.2: Prepare before capturing data

A.3.3 Data capture

After adopting all the setting parameters in the digitizer, with C++ we instruct the digitizer to capture the data in "ADMA_NPT" way. The main reason of using C++ instead of python is we could implement multithread coding which enables multiple cores of the PC working on different parts of the program in parallel. When each buffer containing "rPB" number of records is transferred to the PC memory, the records are distributed within the available cores of the PC and after all the cores are done with processing those records, all of them are combined back again. For the PCs in lab with 16 cores, the task now with multithreading takes 1/16 the time of the same task taking time to be processed using single core.

Moreover, the way the digitizer packs records of data is different for different digitizers. For example, in ATS9870, it packs the data in form of B1, B2,...,BN where "BN" denotes Nth buffer and each buffer includes R1A, R2A,...,RNA, R1B, R2B,...,RNB where "R" denotes record, "1" denotes the index of the record and "A/B" denotes the channel. So in this case it is easy to unpack the data in the host PC is very easy based on channel as well as buffer.

But in ATS9371, when using both channels together, the data comes interleaved. It packs the data in the form of B1, B2, B3,..., BN where each of the odd-numbered buffers B1,B3,B5,... contain records from channel A R1A, R2A,...,RNA and the even-numbered buffers B2, B4, B6,...,BN contain records from channel B R1B, R2B,...,RNB. Moreover, ATS9371 captures data with 12-bit resolution, hence each sample it sends to host memory is of 2-bytes (16-bit) long. The example code for ATS9371 is below.

```
2 if (success)
3 {
4
      retCode = AlazarStartCapture(boardHandle);
5
      if (retCode != ApiSuccess)
6
7
          printf("Error: AlazarStartCapture failed -- %s\n",
      AlazarErrorToText (retCode));
          success = 9;
9
10 }
11 if (success)
12 {
      U32 buffersCompleted = 0;
13
14
      INT64 bytesTransferred = 0;
      while (buffersCompleted < buffersPerAcquisition)</pre>
15
16
           U32 timeout_ms = 5000;
17
          bufferIndex = buffersCompleted % BUFFER_COUNT;
18
19
           Ipp16u* pBuffer = BufferArray[bufferIndex];//U16* pBuffer =
      BufferArray[bufferIndex];
          retCode = AlazarWaitAsyncBufferComplete(boardHandle, pBuffer,
20
      timeout_ms);
21
          if (retCode != ApiSuccess)
22
           {
               printf("Error: AlazarWaitAsyncBufferComplete failed -- %s\n",
23
24
                   AlazarErrorToText(retCode));
               success = 14;
25
26
           }
27
           if (success)
28
29
           {
30
               buffersCompleted++;
31
               bytesTransferred += bytesPerBuffer;
32
33
               U32 recordInBuffer = 0;
               U32 recordsRemaining = recordsPerBuffer;
34
               U32 recordsPerThread = recordsPerBuffer / ThreadCount;
35
               for (U32 threadIndex = 0; threadIndex < ThreadCount;</pre>
      threadIndex++)
37
               {
38
                   THREAD_PARAMS* pThreadParams = &ThreadParams[threadIndex];
39
                   pThreadParams->pRecord = pBuffer + samplesPerRecord *
      recordInBuffer * channelCount;
                   pThreadParams->pAccRecord = pAccRecord + threadIndex *
40
      samplesPerRecord * channelCount;
41
                   pThreadParams->samplesPerRecord = samplesPerRecord;
42
                   if (threadIndex == (ThreadCount - 1))
43
44
                       pThreadParams->recordsToProcess = recordsRemaining;
45
```

```
46
                        pThreadParams->recordsToProcess = recordsPerThread;
47
                    if (!SetEvent(pThreadParams->threadEvent))
48
49
                    {
                        printf("Error: SetEvent failed -- %u", GetLastError());
50
51
                        success = 15;
52
                        break;
                    }
53
54
55
                    recordInBuffer += recordsPerThread;
                    recordsRemaining -= recordsPerThread;
56
57
58
               if (success)
59
60
                {
                    // Wait for worker threads to finish summing their rows
61
                    for (U32 threadIndex = 0; threadIndex < ThreadCount;</pre>
62
      threadIndex++)
63
64
                        U32 result = WaitForSingleObject(
                             ThreadParams[threadIndex].threadDoneEvent, INFINITE
65
      );
66
                        if (result != WAIT_OBJECT_0)
67
                             printf("Error: WaitForSingleObject failed -- %u\n",
68
       GetLastError());
                             success = 16;
69
70
71
                    }
               }
72
73
74
                   (success)
75
                    for (U32 sample = 0; sample < samplesPerRecord *</pre>
76
      channelCount; sample++)
77
                    {
                        double sum = 0;
78
                        for (U32 threadIndex = 0; threadIndex < ThreadCount;</pre>
79
      threadIndex++)
80
                        {
                             THREAD_PARAMS* pThreadParams = &ThreadParams[
81
      threadIndex];
82
                             sum += *(pThreadParams->pAccRecord + sample);
83
84
                        *(averageSignal + sample) += sum;
85
                    }
                }
87
           }
88
           if (success)
89
               retCode = AlazarPostAsyncBuffer(boardHandle, pBuffer,
90
      bytesPerBuffer);
               if (retCode != ApiSuccess)
91
92
93
                     printf("Error: AlazarPostAsyncBuffer failed -- %s\n",
                        AlazarErrorToText(retCode));
94
                    success = retCode;
95
96
                }
```

```
if (!success)
99
               break;
       }
100
101
102
103
       for (U32 sample = 0; sample < samplesPerRecord * channelCount; sample</pre>
       ++)
104
       {
            *(averageSignal + sample) /= buffersPerAcquisition *
105
       recordsPerBuffer;
106
107 }
108 retCode = AlazarAbortAsyncRead(boardHandle);
109 if (retCode != ApiSuccess)
110 {
       printf("Error: AlazarAbortAsyncRead failed -- %s\n", AlazarErrorToText(
111
      retCode));
      success = 18;
112
113 }
114 StopWorkerThreads();
115 for (bufferIndex = 0; bufferIndex < BUFFER_COUNT; bufferIndex++)</pre>
116 {
117
       if (BufferArray[bufferIndex] != NULL)
118
       {
           AlazarFreeBufferU16(boardHandle, BufferArray[bufferIndex]);
119
120
121 }
122
123 if (pAccRecord != NULL)
       ippsFree (pAccRecord);
124
125
126 if (success == TRUE) {
       return 1;
127
128 }
129 else {
130 return success;
131 }
```

Listing A.3: Adopt settings in Digitizer

A.4 The necessary C++ files

The main signal processing programs are written in "CATSdriver.cpp" but there are other necessary components for multithreading programming, or digitizer communication or setting the sizes of variables are done in separate ".cpp" files and all of them are combined altogether to make it work effectively.

- **1. ATSCommunication.cpp** In this file, communication between PC and the Alazar driver is programmed.
- **2. CATSdriver.cpp** In this file, all the signal processing segments are written. We built different functions dedicated to smaller signal processing elements to be able to distribute the tasks between thread. Such functions are:
- (i)DDC it contains multiplying the data once with sinusoid and once with cosinusoid of the IF frequency,

- (ii) CONVERT to convert the digitized data in bits to voltage depending on the chosen volt range,
- (iii) WINDOW depending on user's input, either only window filter with cutoff frequency at IF or both window filter and another chebyshev filter with user-defined cut-off frequency are applied,
- (v) DISCARD_ARTIFACTS Generally, before applying filtering, the size of the data on which the filter will be applied is increased by the filter length; because after convolution with filter, there is a delay in filtered signal by exactly the filter length; under this function, discarding the first a few sample points equal to filter length are discarded;
- (vi) FACTOR this function involves multiplying by 1/2,
- (vii) COMPLEX_IQ converting to complex, i.e., if you have I and Q then this function will return I+iQ,
- (viii) CMPLX_MUL it returns the multiplication between two complex numbers,
- (ix) CONJUGATE it conjugates the complex number,
- (x) FFT it performs fourier transform,
- (xi) RE_IM_PART it separates real and imaginary parts of a complex number,
- (xii) ACCUMULATE it accumulates all the processed from all the threads after thread work is finished.
- 3. Bufferhandler.cpp In this file, the size of allocated space for each buffer is initialized.

A.5 Create new signal processing technique using the functions defined in CATSdriver.cpp

Let's create the $G^{(2)}(\tau)$ function in "Scripts_instruction.py".

- Add this new object with the name for example "GAMMA2_TAU" in the dictionary "script_instructions". Then develop the processing as follows:

```
2 "GAMMA2 TAU":
3 {
      "processing": ["CONVERT", # conversion to volts
4
                      "DDC", # multiplication with sin and cosin
5
                      "WINDOW", # window and chebyshev filters are applied
6
7
                      "DISCARD_ARTIFACTS", # the artifacts discarded
                      "FACTOR", # 1/2 multiplied
8
                      "COMPLEX_IQ", \# S_A,B = I_A,B + iQ_A,B
9
                      "CMPLX_MUL", \# Calculate S_A* x S_B
10
                      "CONJUGATE", # complex conjugate of S_A* x S_B
11
12
                      "FFT", \# F(S_A* x S_B) and F(S_B* x S_A) calculated
13
                      "CMPLX_MUL", \# F*(S_A* x S_B) x F(S_B* x S_A)
                      "RE_IM_PART", # Real and Imaginary parts are separated
14
                      "ACCUMULATE", # Ensemble averaging
15
                      "IFFT"] # back to time domain
16
17
```

A.6 Linking C++ and python

Everytime, we change something, be it adding new signal processing or updating digitizer communication in "CATSdriver.cpp", we build a python version of it with the name "CATS-Driver.py" to be added in VIP under Alazar driver folder. We follow the following steps to build the python version :

- in Anaconda Prompt 3, go to the folder where the C++ code is written. For us the address is: "C:\ Users \ useme \ Repository \ c-ats-drivers \ ATS9870". Then write: "swig -c++ python CATSDriver.i" and press enter.
- A file with name having the extension "..._wrap.cxx" will be produced. Replace this new file in C under "Source Files" in the "Solution Explorer"
- Then build the solution and new "CATSDriver.py" a python file will be built.
- Replace this new ".py" file in the VIP in the Alazar driver folder.

Numerical model of Jaynes-cummings model

This whole chapter is based on theoretical and numerical development by Andras Vukics from the Wigner Research Center for Physics

B.1 The full quantum model

The basic Hamiltonian for a multilevel system interacting with a driven mode reads ($\hbar = 1$):

$$H = \sum_{u} \left[h_{u} |u\rangle \langle u| + i \left(g_{u+1} a |u+1\rangle \langle u| - \text{h.c.} \right) \right] + \omega_{R} a^{\dagger} a + i \left(\eta e^{-i\omega t} a^{\dagger} - \text{h.c.} \right).$$
(B.1)

Here, u indexes the transmon levels, and we assume that only transitions between adjacent levels couple to the mode, with coupling coefficient g_{u+1} . The h_u s are the bare transmon energies, ω_R is the bare mode frequency, and η and ω are the drive strength and frequency, respectively.

The Hamiltonian is written in the rotating-wave approximation. This is justified as long as the coupling strength does not reach the Bloch-Siegert regime of ultrastrong coupling, meaning $10\,g_1 \lesssim h, \omega_R$ [FDLR+19], which holds for our system. For the coupling coefficients, we use the standard relation for transmons:

$$g_{u+1} = \sqrt{u+1} \, g_1. \tag{B.2}$$

For a comprehensive theory of the transmon see Refs. [BGGW21, SHK+08].

Transforming to the frame rotating with ω , we obtain a time-independent Hamiltonian with $\Delta \equiv \omega - \omega_R$:

$$H = \sum_{u} \left[(h_{u} - u \omega) |u\rangle \langle u| + i \left(g_{u+1} a |u+1\rangle \langle u| - \text{h.c.} \right) \right] -\Delta a^{\dagger} a + i \left(\eta a^{\dagger} - \text{h.c.} \right).$$
(B.3)

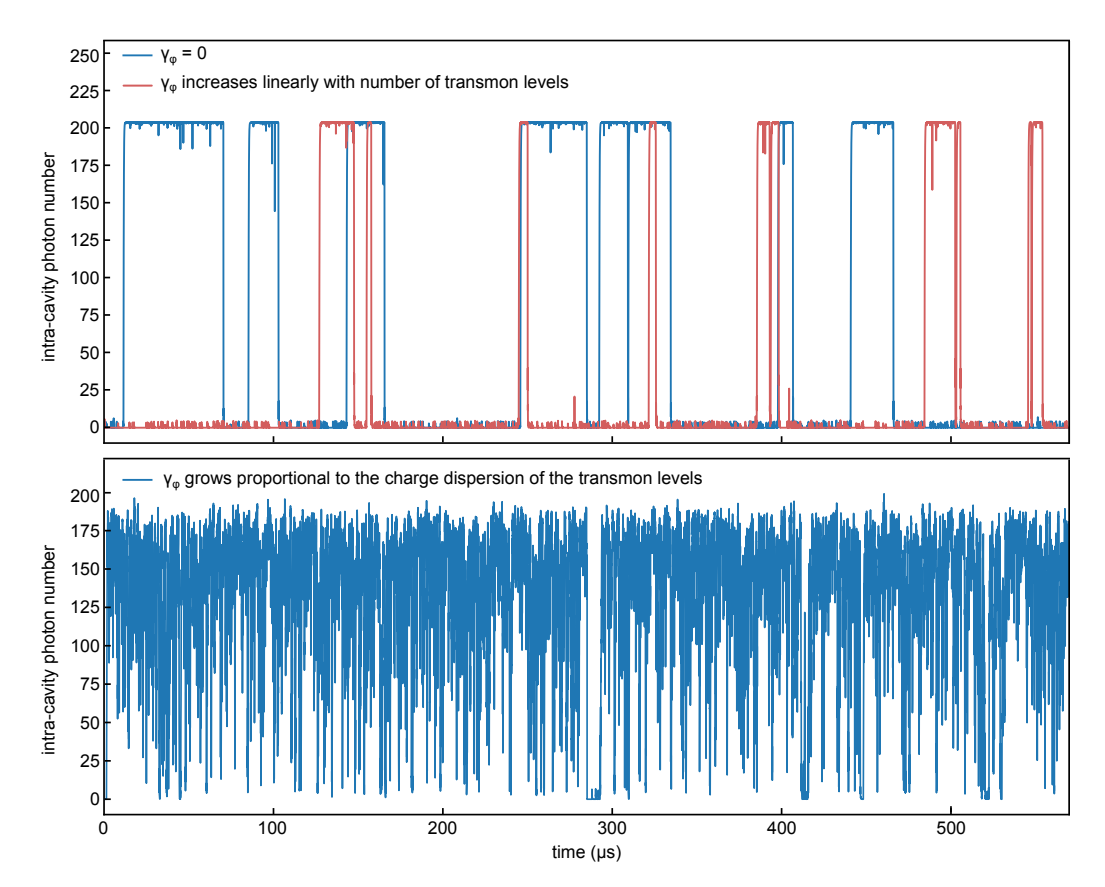


Figure B.1: Simulated example trajectories for the three possibilities of modeling dephasing of higher transmon levels for otherwise identical parameters (five transmon levels, $\gamma_1=0$, $\gamma_{\phi,1}/2\pi=50\,\mathrm{kHz}$, $\eta/2\pi=100\,\mathrm{MHz}$, $\kappa/2\pi=14.3\,\mathrm{MHz}$): no dephasing (top), flux noise model (top, red), and charge dispersion model (bottom, blue). The last case leads to qualitatively incompatible results with very large noise levels and only partially stabilised attractors.

Here, putting $h_0=0$, and assuming the 0-1 transition resonant with the mode ($h_1=\omega_R$), we obtain a simple form for the bare transmon Hamiltonian, which we give for the first three levels:

$$H_{\text{transmon}} = -\Delta |1\rangle \langle 1| - (2\Delta - \Delta_{\text{an}}) |2\rangle \langle 2|$$
+contribution of higher levels, (B.4)

where $\Delta_{an} \equiv h_2 - 2h_1$ is the anharmonicity of the third level, which is related to the charging energy.

We turn now to dissipation, which we describe with the Liouvillian

$$\mathcal{L}\rho = \sum_{i} \left(L_{i} \rho L_{i}^{\dagger} - \frac{1}{2} \left\{ L_{i}^{\dagger} L_{i} \rho \right\} \right) \equiv \left(\mathcal{L}_{\mathsf{mode}} + \mathcal{L}_{\mathsf{relax}} + \mathcal{L}_{\mathsf{dephase}} \right) \rho \tag{B.5}$$

with the following three dissipative channels:

- (1) Resonator decay, $\mathcal{L}_{\text{mode}}$. This is described by the jump operators $L_{-} = \sqrt{2 \left(n_{\text{th}} + 1 \right) \kappa} \, a$ and $L_{+} = \sqrt{2 \, n_{\text{th}} \, \kappa} \, a^{\dagger}$. Here n_{th} is the number of thermal photons, which can be neglected in our system, so the second kind of quantum jumps (absorption of thermal photons) does not exist.
- (2) Energy relaxation of the transmon, \mathcal{L}_{relax} . In analogy with the coupling to the resonator mode, we assume that this occurs only as transitions between adjacent levels. It is described

by the jump operators $L_{u+1\to u}=\sqrt{\gamma_{u+1\to u}}\;|u\rangle\;\langle u+1|$. In the simulation, we take $\gamma_{u+1\to u}$ equal for all levels, and we identify it with γ_1 in circuit QED.

(3) Dephasing of the transmon, $\mathcal{L}_{dephase}$. This is also defined separately for all transmon levels, and its jump operator for level v is

$$L_{\phi,v} = \sqrt{\gamma_{\phi,v}} \left(\sum_{u \neq v} |u\rangle \langle u| - |v\rangle \langle v| \right) = \sqrt{\gamma_{\phi,v}} \left(\mathbf{1} - 2 |v\rangle \langle v| \right), \tag{B.6}$$

so it simply flips the phase of level v by π . Modeling the behavior of the dephasing for different transmon levels is nontrivial. We consider three possibilities:

- 1. $\gamma_{\phi,v}=0$ for all v. This is only to get a theoretical baseline of dephasing-free behavior.
- 2. Linear growth as $\gamma_{\phi,v}=v\,\gamma_{\phi}/8$ following the above convention, as expected for flux noise due to the higher flux gradient of higher levels. Here the dephasing of the first qubit transition $\gamma_{\phi}/2\pi=50\,\mathrm{kHz}$ is taken from the measured vacuum Rabi linewidths and the independently measured cavity linewidth κ .
- 3. Dephasing proportional to the charge dispersion of the transmon levels [BCK+09].

Example trajectories for the three possibilities are displayed in Fig. B.1. It is apparent that the third model leads to very noisy trajectories that do not reproduce qualitatively the experimentally observed behavior of stabilized attractors. Therefore, we omitted this possibility from the quantitative comparison presented in the main text.

In the simulation, for each physical parameter set, several trajectories are run with different random number generator seeds. Relying on the assumption of ergodicity, we concatenated these trajectories for a single long trajectory for each parameter set, which is then used for dwell-time statistics. Since each trajectory is started from the ground state, this method has a bias towards the dim state (breaching of ergodicity), which is the stronger, the longer the dwell time with respect to the simulation time.

The full quantum simulations were implemented within the C++QED simulation framework (http://github.com/vukics/cppqed), and took about 1 year on a 64-core virtual cluster defined within an OpenStack cloud environment (http://science-cloud.hu/).

B.2 An approximate three-level neoclassical theory and its solution for the intensity

From the master equation $\dot{\rho}=[H,\rho]/(i\hbar)+\mathcal{L}\rho$ we can derive equations for the expectation values of the operators a and $\sigma_{uv}=|u\rangle\,\langle v|$, where u and v index atomic levels. In the case of a two-level system, this simply reproduces the Maxwell-Bloch equations, with the added complication of the qubit dephasing. Here, we list the equations for a three-level transmon with states $|g\rangle,\,|e\rangle$ and $|f\rangle$, which still leads to an algebraically tractable scheme. In this case,

six equations are needed for a complete system:

$$\dot{\alpha} = (i\Delta - \kappa)\alpha + \eta - g_1 \, s_{qe} - g_2 \, s_{ef} \tag{B.7a}$$

$$\dot{s}_{qe} = (i\Delta - \gamma_1) \, s_{qe} - g_1 \, (s_{ee} - s_{qq}) \, \alpha - g_2 \, s_{qf} \, \alpha^*$$
 (B.7b)

$$\dot{s}_{gg} = \gamma_1 \, s_{ee} - 2g_1 \, \Re\{\alpha^* \, s_{ge}\} \tag{B.7c}$$

$$\dot{s}_{ef} = (i[\Delta - \Delta_{an}] - [\gamma_1 + 4(\gamma_{\phi,1} + \gamma_{\phi,2})]) s_{ef}$$

$$+ g_2 (s_{ee} - s_{ff}) \alpha + g_1 \alpha^* s_{gf}$$
 (B.7d)

$$\dot{s}_{ee} = 2g_1 \Re\{\alpha^* s_{ge}\} - 2g_2 \Re\{\alpha^* s_{ef}\} - \gamma_1 s_{ee} + \gamma_1 s_{ff}$$
(B.7e)

$$\dot{s}_{gf} = \!\! \left(i[2\Delta - \Delta_{\mathrm{an}}] - \left[\gamma_1 + 4\gamma_{\phi,2}\right]\right) s_{gf}$$

$$-g_1 \alpha s_{ef} + g_2 \alpha s_{ge} \tag{B.7f}$$

Here $\alpha = \langle a \rangle$, and $s_{uv} = \langle \sigma_{uv} \rangle$. The system is completed with the completeness relation $s_{gg} + s_{ee} + s_{ff} = 1$.

In the two-level case, one obtains the neoclassical theory by zeroing all the γ 's, and observing that the resulting set of equations conserves the atomic pseudospin. This conservation law replaces the steady-state equation for the atomic population, which becomes degenerate in the case of vanishing atomic decay. One recovers, therefore, a closed system of equations for the steady-state mode amplitude and atomic polarization.

In the three-level case, the neoclassical condition (conservation of pseudospin) reads

$$s_{gg}^2 + s_{ee}^2 + s_{ff}^2 + 2(|s_{ge}|^2 + |s_{gf}|^2 + |s_{ef}|^2) = 1.$$
 (B.8)

After all the different kinds of γ in Eq. (B.7) have been zeroed, this can replace the degenerate steady-state equation (B.7c). We get rid of the other problematic equation (B.7e) by assuming $s_{ff}=0$. This leaves us with an approximate three-level neoclassical theory of five equations for the five steady-state expectation values: the mode amplitude, the atomic ground-state population, and the three atomic polarizations. We use this theory to demonstrate that the appearance of the third level can yield bistability at resonant driving ($\Delta=0$), in contrast to the two-level case.

Algebraically, this is an inhomogeneous nonlinear set of equations, which we do not need to fully solve, however. Instead, we can obtain a single implicit equation for only the intensity $|\alpha|^2$ as follows. First, we define the complex dispersive shift

$$\Sigma(|\alpha|^2) = -\frac{g_1 \, s_{ge} + g_2 \, s_{ef}}{\alpha},\tag{B.9}$$

Then, from Eq. (B.7a) we express the steady-state α explicitly. As we show below, Σ depends only on powers of $|\alpha|^2$, and not on other combinations of α and α^* . Therefore, the equation for the intensity can be written as

$$|\alpha|^2 = \frac{|\eta|^2}{\left|\Sigma(|\alpha|^2) + (i\Delta - \kappa)\right|^2}$$
(B.10)

What we have to show for the validity of Eq. (B.10) is that the solutions of s_{ge} and s_{ef} have the form of an $|\alpha|^2$ -dependent expression multiplied by α . The polarizations can be expressed as functions of the population s_{gg} multiplied by α from Eqs. (B.7b), (B.7d) and (B.7f) in the steady state. When these solutions are substituted into the neoclassical condition (B.8), the

factor α in the solutions becomes $|\alpha|^2$. Hence, s_{gg} can be expressed from this equation as a function only of the intensity, and when this is substituted back into the solutions of the polarizations, we obtain the necessary form for them.

Equation (B.10) can be solved numerically. Typical solutions exhibiting bistability at resonance and asymmetry with respect to the sign of Δ are displayed in Fig. 3.5(b). The two-level neoclassical theory can be recovered by setting either $g_2=0$ or $\Delta_{\rm an}=0$.

APPENDIX C

QI numerical derivations

C.1 hypothesis H_1 with anihiliation operator

Variance:

$$\begin{split} (\Delta N^{1})^{2} &= \operatorname{Var}(N_{\mathsf{X}}^{1} - N_{\mathsf{Y}}^{1}) \\ &= \langle (N_{\mathsf{X}}^{1} - N_{\mathsf{Y}}^{1})^{2} \rangle - (\langle N_{\mathsf{X}}^{1} \rangle - \langle N_{\mathsf{Y}}^{1} \rangle)^{2} \\ &= \langle (N_{\mathsf{X}}^{1})^{2} + (N_{\mathsf{Y}}^{1})^{2} - 2N_{\mathsf{X}}^{1}N_{\mathsf{Y}}^{1} \rangle - (\langle N_{\mathsf{X}}^{1} \rangle^{2} + \langle N_{\mathsf{Y}}^{1} \rangle^{2} - 2\langle N_{\mathsf{X}}^{1} \rangle \langle N_{\mathsf{Y}}^{1} \rangle) \\ &= \underbrace{\langle (N_{\mathsf{X}}^{1})^{2} \rangle - \langle N_{\mathsf{X}}^{1} \rangle^{2}}_{\operatorname{var}(N_{\mathsf{X}}^{1})} + \underbrace{\langle (N_{\mathsf{Y}}^{1})^{2} \rangle - \langle N_{\mathsf{Y}}^{1} \rangle^{2}}_{\operatorname{var}(N_{\mathsf{Y}}^{1})} - 2(\langle N_{\mathsf{X}}^{1}N_{\mathsf{Y}}^{1} \rangle - \langle N_{\mathsf{X}}^{1} \rangle \langle N_{\mathsf{Y}}^{1} \rangle) \end{split} \tag{C.1}$$

• Var (N_X^1)

$$\begin{aligned} \operatorname{Var}(N_{\mathsf{X}}^{1}) &= \langle (N_{\mathsf{X}}^{1})^{2} \rangle - \langle N_{\mathsf{X}}^{1} \rangle^{2} \\ &= \langle a_{\mathsf{X}}^{\dagger} a_{\mathsf{X}} a_{\mathsf{X}}^{\dagger} a_{\mathsf{X}} \rangle - (N_{\mathsf{X}}^{1})^{2} \\ &= \langle a_{\mathsf{X}}^{\dagger} a_{\mathsf{X}} \rangle \langle a_{\mathsf{X}}^{\dagger} a_{\mathsf{X}} \rangle + \langle a_{\mathsf{X}}^{\dagger} a_{\mathsf{X}}^{\dagger} \rangle \langle a_{\mathsf{X}} a_{\mathsf{X}} \rangle + \langle a_{\mathsf{X}}^{\dagger} a_{\mathsf{X}} \rangle \langle a_{\mathsf{X}} a_{\mathsf{X}}^{\dagger} \rangle \\ &= (N_{\mathsf{X}}^{1})^{2} + \underbrace{\langle (a_{\mathsf{X}}^{\dagger})^{2} \rangle \langle (a_{\mathsf{X}})^{2} \rangle}_{0} + N_{\mathsf{X}}^{1} (1 + N_{\mathsf{X}}^{1}) - (N_{\mathsf{X}}^{1})^{2} \\ &= N_{\mathsf{X}}^{1} (1 + N_{\mathsf{X}}^{1}) \end{aligned} \tag{C.2}$$

Var (N_Y¹)

$$\begin{aligned} \mathsf{Var}(N_{\mathsf{Y}}^{1}) &= \langle (N_{\mathsf{Y}}^{1})^{2} \rangle - \langle N_{\mathsf{Y}}^{1} \rangle^{2} \\ &= \langle a_{\mathsf{Y}}^{\dagger} a_{\mathsf{Y}} a_{\mathsf{Y}}^{\dagger} a_{\mathsf{Y}} \rangle - (N_{\mathsf{Y}}^{1})^{2} \\ &= \langle a_{\mathsf{Y}}^{\dagger} a_{\mathsf{Y}} \rangle \langle a_{\mathsf{Y}}^{\dagger} a_{\mathsf{Y}} \rangle + \langle a_{\mathsf{Y}}^{\dagger} a_{\mathsf{Y}}^{\dagger} \rangle \langle a_{\mathsf{Y}} a_{\mathsf{Y}} \rangle + \langle a_{\mathsf{Y}}^{\dagger} a_{\mathsf{Y}} \rangle \langle a_{\mathsf{Y}} a_{\mathsf{Y}}^{\dagger} \rangle \\ &= (N_{\mathsf{Y}}^{1})^{2} + \underbrace{\langle (a_{\mathsf{Y}}^{\dagger})^{2} \rangle \langle (a_{\mathsf{Y}})^{2} \rangle}_{0} + N_{\mathsf{Y}}^{1} (1 + N_{\mathsf{Y}}^{1}) - (N_{\mathsf{Y}}^{1})^{2} \\ &= N_{\mathsf{Y}}^{1} (1 + N_{\mathsf{Y}}^{1}) \end{aligned} \tag{C.3}$$

$\bullet \quad \langle N_{\mathsf{X}}^1 N_{\mathsf{Y}}^1 \rangle$

$$\begin{split} \langle N_{\mathsf{X}}^{1} N_{\mathsf{Y}}^{1} \rangle &= \langle a_{\mathsf{X}}^{\dagger} a_{\mathsf{X}} a_{\mathsf{Y}}^{\dagger} a_{\mathsf{Y}} \rangle \\ &= \langle (\sqrt{\mathsf{G}}_{\mathsf{X}} a_{1}^{\dagger} + \sqrt{\mathsf{G}_{\mathsf{X}} - 1} \mathsf{h}_{\mathsf{X}}) (\sqrt{\mathsf{G}}_{\mathsf{X}} a_{1} + \sqrt{\mathsf{G}_{\mathsf{X}} - 1} \mathsf{h}_{\mathsf{X}}^{\dagger}) \\ &\quad (\sqrt{\mathsf{G}}_{\mathsf{Y}} a_{2}^{\dagger} + \sqrt{\mathsf{G}_{\mathsf{Y}} - 1} \mathsf{h}_{\mathsf{Y}}) (\sqrt{\mathsf{G}}_{\mathsf{Y}} a_{2} + \sqrt{\mathsf{G}_{\mathsf{Y}} - 1} \mathsf{h}_{\mathsf{Y}}^{\dagger}) \rangle \\ &= \langle (\mathsf{G}_{\mathsf{X}} a_{1}^{\dagger} a_{1} + \sqrt{\mathsf{G}_{\mathsf{X}} (\mathsf{G}_{\mathsf{X}} - 1)} (a_{1}^{\dagger} \mathsf{h}_{\mathsf{X}}^{\dagger} + \mathsf{h}_{\mathsf{X}} a_{1}) + (\mathsf{G}_{\mathsf{X}} - 1) \mathsf{h}_{\mathsf{X}} \mathsf{h}_{\mathsf{X}}^{\dagger}) \\ &\quad (\mathsf{G}_{\mathsf{Y}} a_{2}^{\dagger} a_{2} + \sqrt{\mathsf{G}_{\mathsf{Y}} (\mathsf{G}_{\mathsf{Y}} - 1)} (a_{2}^{\dagger} \mathsf{h}_{\mathsf{Y}}^{\dagger} + \mathsf{h}_{\mathsf{Y}} a_{2}) + (\mathsf{G}_{\mathsf{Y}} - 1) \mathsf{h}_{\mathsf{Y}} \mathsf{h}_{\mathsf{Y}}^{\dagger}) \rangle \\ &= \mathsf{G}_{\mathsf{X}} \mathsf{G}_{\mathsf{Y}} \langle a_{1}^{\dagger} a_{1} a_{2}^{\dagger} a_{2} \rangle + \mathsf{G}_{\mathsf{X}} (\mathsf{G}_{\mathsf{Y}} - 1) \langle a_{1}^{\dagger} a_{1} \mathsf{h}_{\mathsf{Y}} \mathsf{h}_{\mathsf{Y}}^{\dagger} \rangle + \mathsf{G}_{\mathsf{Y}} (\mathsf{G}_{\mathsf{X}} - 1) \langle \mathsf{h}_{\mathsf{X}} \mathsf{h}_{\mathsf{X}}^{\dagger} a_{2}^{\dagger} a_{2} \rangle + \\ &\quad (\mathsf{G}_{\mathsf{X}} - 1) (\mathsf{G}_{\mathsf{Y}} - 1) \langle \mathsf{h}_{\mathsf{X}} \mathsf{h}_{\mathsf{X}}^{\dagger} \mathsf{h}_{\mathsf{Y}} \mathsf{h}_{\mathsf{Y}}^{\dagger} \rangle \end{split}$$

Now we expand each of the terms of Eq. (C.4)

Term 1:
$$\langle a_{\mathbf{1}}^{\dagger} a_{\mathbf{1}} a_{\mathbf{2}}^{\dagger} a_{\mathbf{2}} \rangle = \frac{1}{4} \langle (a_{\mathsf{PC}}^{\dagger} + a_{\mathsf{I}}^{\dagger}) (a_{\mathsf{PC}} + a_{\mathsf{I}}) (a_{\mathsf{PC}}^{\dagger} - a_{\mathsf{I}}^{\dagger}) (a_{\mathsf{PC}} - a_{\mathsf{I}}) \rangle$$

$$= \frac{1}{4} \langle (a_{\mathsf{PC}}^{\dagger} a_{\mathsf{PC}} + a_{\mathsf{PC}}^{\dagger} a_{\mathsf{I}} + a_{\mathsf{I}}^{\dagger} a_{\mathsf{PC}} + a_{\mathsf{I}}^{\dagger} a_{\mathsf{I}}) \qquad (C.5)$$

$$(a_{\mathsf{PC}}^{\dagger} a_{\mathsf{PC}} - a_{\mathsf{PC}}^{\dagger} a_{\mathsf{I}} - a_{\mathsf{I}}^{\dagger} a_{\mathsf{PC}} + a_{\mathsf{I}}^{\dagger} a_{\mathsf{I}}) \rangle$$

with,

$$\langle a_{\mathsf{PC}}^{\dagger} a_{\mathsf{PC}} a_{\mathsf{PC}}^{\dagger} a_{\mathsf{PC}} \rangle = \langle a_{\mathsf{PC}}^{\dagger} a_{\mathsf{PC}} \rangle^{2} + \underbrace{\langle (a_{\mathsf{PC}}^{\dagger})^{2} \rangle \langle (a_{\mathsf{PC}})^{2} \rangle}_{0} + \langle a_{\mathsf{PC}}^{\dagger} a_{\mathsf{PC}} \rangle \langle a_{\mathsf{PC}} a_{\mathsf{PC}}^{\dagger} \rangle$$

$$= N_{\mathsf{PC}}^{2} + N_{\mathsf{PC}} (N_{\mathsf{PC}} + 1)$$

$$= 2N_{\mathsf{PC}}^{2} + N_{\mathsf{PC}}$$
(C.6)

$$-\langle a_{\mathsf{PC}}^{\dagger} a_{\mathsf{PC}} a_{\mathsf{PC}}^{\dagger} a_{\mathsf{I}} \rangle = -\langle a_{\mathsf{PC}}^{\dagger} a_{\mathsf{PC}} \rangle \langle a_{\mathsf{PC}}^{\dagger} a_{\mathsf{I}} \rangle - \underbrace{\langle (a_{\mathsf{PC}}^{\dagger})^{2} \rangle \langle a_{\mathsf{PC}} a_{\mathsf{I}} \rangle}_{0} - \langle a_{\mathsf{PC}}^{\dagger} a_{\mathsf{I}} \rangle \langle a_{\mathsf{PC}} a_{\mathsf{PC}}^{\dagger} \rangle$$

$$= -C_{\mathsf{q}} N_{\mathsf{PC}} - C_{\mathsf{q}} (N_{\mathsf{PC}} + 1)$$

$$= -2C_{\mathsf{q}} N_{\mathsf{PC}} - C_{\mathsf{q}}$$
(C.7)

$$-\langle a_{\mathsf{PC}}^{\dagger} a_{\mathsf{PC}} a_{\mathsf{I}}^{\dagger} a_{\mathsf{PC}} \rangle = -\langle a_{\mathsf{PC}}^{\dagger} a_{\mathsf{PC}} \rangle \langle a_{\mathsf{I}}^{\dagger} a_{\mathsf{PC}} \rangle - \underbrace{\langle a_{\mathsf{PC}}^{\dagger} a_{\mathsf{I}}^{\dagger} \rangle \langle a_{\mathsf{PC}}^{2}}_{0} - \langle a_{\mathsf{PC}}^{\dagger} a_{\mathsf{PC}} \rangle \langle a_{\mathsf{PC}} a_{\mathsf{I}}^{\dagger} \rangle$$

$$= -C_{\mathsf{q}} N_{\mathsf{PC}} - C_{\mathsf{q}} N_{\mathsf{PC}}$$

$$= -2C_{\mathsf{q}} N_{\mathsf{PC}}$$
(C.8)

$$\langle a_{\mathsf{PC}}^{\dagger} a_{\mathsf{PC}} a_{\mathsf{I}}^{\dagger} a_{\mathsf{I}} \rangle = \langle a_{\mathsf{PC}}^{\dagger} a_{\mathsf{PC}} \rangle \langle a_{\mathsf{I}}^{\dagger} a_{\mathsf{I}} \rangle + \underbrace{\langle a_{\mathsf{PC}}^{\dagger} a_{\mathsf{I}}^{\dagger} \rangle \langle a_{\mathsf{PC}} a_{\mathsf{I}} \rangle}_{0} + \langle a_{\mathsf{PC}}^{\dagger} a_{\mathsf{I}} \rangle \langle a_{\mathsf{PC}} a_{\mathsf{I}}^{\dagger} \rangle$$

$$= N_{\mathsf{PC}} N_{\mathsf{I}} + C_{\mathsf{a}}^{2} \tag{C.9}$$

$$\langle a_{\mathsf{PC}}^{\dagger} a_{\mathsf{I}} a_{\mathsf{PC}}^{\dagger} a_{\mathsf{PC}} \rangle = \langle a_{\mathsf{PC}}^{\dagger} a_{\mathsf{I}} \rangle \langle a_{\mathsf{PC}}^{\dagger} a_{\mathsf{PC}} \rangle + \underbrace{\langle (a_{\mathsf{PC}}^{\dagger})^2 \rangle \langle a_{\mathsf{I}} a_{\mathsf{PC}} \rangle}_{0} + \langle a_{\mathsf{PC}}^{\dagger} a_{\mathsf{PC}} \rangle \langle a_{\mathsf{I}} a_{\mathsf{PC}}^{\dagger} \rangle$$

$$= C_{\mathsf{q}} N_{\mathsf{PC}} + C_{\mathsf{q}} N_{\mathsf{PC}}$$

$$= 2C_{\mathsf{q}} N_{\mathsf{PC}}$$

$$= 2C_{\mathsf{q}} N_{\mathsf{PC}}$$
(C.10)

$$-\langle a_{\mathsf{PC}}^{\dagger} a_{\mathsf{I}} a_{\mathsf{PC}}^{\dagger} a_{\mathsf{I}} \rangle = -\langle a_{\mathsf{PC}}^{\dagger} a_{\mathsf{I}} \rangle \langle a_{\mathsf{PC}}^{\dagger} a_{\mathsf{I}} \rangle - \underbrace{\langle (a_{\mathsf{PC}}^{\dagger})^2 \rangle \langle a_{\mathsf{I}}^2 \rangle}_{0} - \langle a_{\mathsf{PC}}^{\dagger} a_{\mathsf{I}} \rangle \langle a_{\mathsf{I}} a_{\mathsf{PC}}^{\dagger} \rangle$$

$$= -C_{\mathsf{q}}^2 - C_{\mathsf{q}}^2$$

$$= -2C_{\mathsf{q}}^2$$
(C.11)

$$-\langle a_{\mathsf{PC}}^{\dagger} a_{\mathsf{I}} a_{\mathsf{I}}^{\dagger} a_{\mathsf{PC}} \rangle = -\langle a_{\mathsf{PC}}^{\dagger} a_{\mathsf{I}} \rangle \langle a_{\mathsf{I}}^{\dagger} a_{\mathsf{PC}} \rangle - \underbrace{\langle a_{\mathsf{PC}}^{\dagger} a_{\mathsf{I}}^{\dagger} \rangle \langle a_{\mathsf{I}} a_{\mathsf{PC}} \rangle}_{0} - \langle a_{\mathsf{PC}}^{\dagger} a_{\mathsf{PC}} \rangle \langle a_{\mathsf{I}} a_{\mathsf{I}}^{\dagger} \rangle$$

$$= -C_{\mathsf{q}}^{2} - N_{\mathsf{PC}} (N_{\mathsf{I}} + 1)$$

$$= -C_{\mathsf{q}}^{2} - N_{\mathsf{PC}} N_{\mathsf{I}} - N_{\mathsf{PC}}$$
(C.12)

$$\langle a_{\mathsf{PC}}^{\dagger} a_{\mathsf{I}} a_{\mathsf{I}}^{\dagger} a_{\mathsf{I}} \rangle = \langle a_{\mathsf{PC}}^{\dagger} a_{\mathsf{I}} \rangle \langle a_{\mathsf{I}}^{\dagger} a_{\mathsf{I}} \rangle + \underbrace{\langle a_{\mathsf{PC}}^{\dagger} a_{\mathsf{I}}^{\dagger} \rangle \langle a_{\mathsf{I}}^{2} \rangle}_{0} + \langle a_{\mathsf{PC}}^{\dagger} a_{\mathsf{I}} \rangle \langle a_{\mathsf{I}} a_{\mathsf{I}}^{\dagger} \rangle$$

$$= C_{\mathsf{q}} N_{\mathsf{I}} + C_{\mathsf{q}} (N_{\mathsf{I}} + 1)$$

$$= 2C_{\mathsf{q}} N_{\mathsf{I}} + C_{\mathsf{q}}$$
(C.13)

$$\langle a_{\mathsf{I}}^{\dagger} a_{\mathsf{PC}} a_{\mathsf{PC}}^{\dagger} a_{\mathsf{PC}} \rangle = \langle a_{\mathsf{I}}^{\dagger} a_{\mathsf{PC}} \rangle \langle a_{\mathsf{PC}}^{\dagger} a_{\mathsf{PC}} \rangle + \underbrace{\langle a_{\mathsf{I}}^{\dagger} a_{\mathsf{PC}}^{\dagger} \rangle \langle a_{\mathsf{PC}}^{2} \rangle}_{0} + \langle a_{\mathsf{I}}^{\dagger} a_{\mathsf{PC}} \rangle \langle a_{\mathsf{PC}} a_{\mathsf{PC}}^{\dagger} \rangle$$

$$= C_{\mathsf{q}} N_{\mathsf{PC}} + C_{\mathsf{q}} (N_{\mathsf{PC}} + 1)$$

$$= 2C_{\mathsf{q}} N_{\mathsf{PC}} + C_{\mathsf{q}}$$
(C.14)

$$-\langle a_{\mathsf{I}}^{\dagger} a_{\mathsf{PC}} a_{\mathsf{PC}}^{\dagger} a_{\mathsf{I}} \rangle = -\langle a_{\mathsf{I}}^{\dagger} a_{\mathsf{PC}} \rangle \langle a_{\mathsf{PC}}^{\dagger} a_{\mathsf{I}} \rangle - \underbrace{\langle a_{\mathsf{I}}^{\dagger} a_{\mathsf{PC}}^{\dagger} \rangle \langle a_{\mathsf{PC}} a_{\mathsf{I}} \rangle}_{0} - \langle a_{\mathsf{I}}^{\dagger} a_{\mathsf{I}} \rangle \langle a_{\mathsf{PC}} a_{\mathsf{PC}}^{\dagger} \rangle$$

$$= -C_{\mathsf{q}}^{2} - N_{\mathsf{I}} (N_{\mathsf{PC}} + 1)$$

$$= -C_{\mathsf{q}}^{2} - N_{\mathsf{I}} N_{\mathsf{PC}} - N_{\mathsf{I}}$$
(C.15)

$$-\langle a_{\mathsf{I}}^{\dagger} a_{\mathsf{PC}} a_{\mathsf{I}}^{\dagger} a_{\mathsf{PC}} \rangle = -\langle a_{\mathsf{I}}^{\dagger} a_{\mathsf{PC}} \rangle \langle a_{\mathsf{I}}^{\dagger} a_{\mathsf{PC}} \rangle - \underbrace{\langle (a_{\mathsf{I}}^{\dagger})^2 \rangle \langle (a_{\mathsf{PC}})^2 \rangle}_{\mathbf{0}} - \langle a_{\mathsf{I}}^{\dagger} a_{\mathsf{PC}} \rangle \langle a_{\mathsf{PC}} a_{\mathsf{I}}^{\dagger} \rangle$$

$$= -C_{\mathsf{q}}^2 - C_{\mathsf{q}}^2$$

$$= -2C_{\mathsf{q}}^2$$
(C.16)

$$\langle a_{\mathsf{I}}^{\dagger} a_{\mathsf{PC}} a_{\mathsf{I}}^{\dagger} a_{\mathsf{I}} \rangle = \langle a_{\mathsf{I}}^{\dagger} a_{\mathsf{PC}} \rangle \langle a_{\mathsf{I}}^{\dagger} a_{\mathsf{I}} \rangle + \underbrace{\langle (a_{\mathsf{I}}^{\dagger})^{2} \rangle \langle a_{\mathsf{PC}} a_{\mathsf{I}} \rangle}_{0} + \langle a_{\mathsf{I}}^{\dagger} a_{\mathsf{I}} \rangle \langle a_{\mathsf{PC}} a_{\mathsf{I}}^{\dagger} \rangle$$

$$= C_{\mathsf{q}} N_{\mathsf{I}} + C_{\mathsf{q}} N_{\mathsf{I}}$$

$$= 2C_{\mathsf{q}} N_{\mathsf{I}}$$

$$= 2C_{\mathsf{q}} N_{\mathsf{I}}$$
(C.17)

$$\langle a_{\mathsf{I}}^{\dagger} a_{\mathsf{I}} a_{\mathsf{PC}}^{\dagger} a_{\mathsf{PC}} \rangle = \langle a_{\mathsf{I}}^{\dagger} a_{\mathsf{I}} \rangle \langle a_{\mathsf{PC}}^{\dagger} a_{\mathsf{PC}} \rangle + \underbrace{\langle a_{\mathsf{I}}^{\dagger} a_{\mathsf{PC}}^{\dagger} \rangle \langle a_{\mathsf{I}} a_{\mathsf{PC}} \rangle}_{0} + \langle a_{\mathsf{I}}^{\dagger} a_{\mathsf{PC}} \rangle \langle a_{\mathsf{I}} a_{\mathsf{PC}}^{\dagger} \rangle$$

$$= N_{\mathsf{I}} N_{\mathsf{PC}} + C_{\mathsf{g}}^{2}$$
(C.18)

$$-\langle a_{\mathsf{I}}^{\dagger} a_{\mathsf{I}} a_{\mathsf{PC}}^{\dagger} a_{\mathsf{I}} \rangle = -\langle a_{\mathsf{I}}^{\dagger} a_{\mathsf{I}} \rangle \langle a_{\mathsf{PC}}^{\dagger} a_{\mathsf{I}} \rangle - \underbrace{\langle a_{\mathsf{I}}^{\dagger} a_{\mathsf{PC}}^{\dagger} \rangle \langle a_{\mathsf{I}}^{2} \rangle}_{0} - \langle a_{\mathsf{I}}^{\dagger} a_{\mathsf{I}} \rangle \langle a_{\mathsf{I}} a_{\mathsf{PC}}^{\dagger} \rangle$$

$$= -C_{\mathsf{q}} N_{\mathsf{I}} - C_{\mathsf{q}} N_{\mathsf{I}}$$

$$= -2C_{\mathsf{q}} N_{\mathsf{I}}$$
(C.19)

$$-\langle a_{\mathsf{I}}^{\dagger} a_{\mathsf{I}} a_{\mathsf{I}}^{\dagger} a_{\mathsf{PC}} \rangle = -\langle a_{\mathsf{I}}^{\dagger} a_{\mathsf{I}} \rangle \langle a_{\mathsf{I}}^{\dagger} a_{\mathsf{PC}} \rangle - \underbrace{\langle (a_{\mathsf{I}}^{\dagger})^{2} \rangle \langle a_{\mathsf{I}} a_{\mathsf{PC}} \rangle}_{\mathbf{0}} - \langle a_{\mathsf{I}}^{\dagger} a_{\mathsf{PC}} \rangle \langle a_{\mathsf{I}} a_{\mathsf{I}}^{\dagger} \rangle$$

$$= -C_{\mathsf{q}} \bar{N}_{\mathsf{I}} - C_{\mathsf{q}} (\bar{N}_{\mathsf{I}} + 1)$$

$$= -2C_{\mathsf{q}} \bar{N}_{\mathsf{I}} - C_{\mathsf{q}}$$
(C.20)

$$\langle a_{\mathbf{I}}^{\dagger} a_{\mathbf{I}} a_{\mathbf{I}}^{\dagger} a_{\mathbf{I}} \rangle = \langle a_{\mathbf{I}}^{\dagger} a_{\mathbf{I}} \rangle \langle a_{\mathbf{I}}^{\dagger} a_{\mathbf{I}} \rangle + \underbrace{\langle (a_{\mathbf{I}}^{\dagger})^{2} \rangle \langle a_{\mathbf{I}}^{2} \rangle}_{\mathbf{0}} + \langle a_{\mathbf{I}}^{\dagger} a_{\mathbf{I}} \rangle \langle a_{\mathbf{I}} a_{\mathbf{I}}^{\dagger} \rangle$$

$$= N_{\mathbf{I}}^{2} + N_{\mathbf{I}}(N_{\mathbf{I}} + 1)$$

$$= 2N_{\mathbf{I}}^{2} + N_{\mathbf{I}}$$
(C.21)

Hence,

Term 1:
$$\langle a_1^{\dagger} a_1 a_2^{\dagger} a_2 \rangle = \frac{1}{4} (2N_{\text{PC}}^2 + N_{\text{PC}} - 2C_{\text{q}} N_{\text{PC}} - C_{\text{q}} - 2C_{\text{q}} N_{\text{PC}} + N_{\text{PC}} N_{\text{I}} + C_{\text{q}}^2$$

$$= \frac{1}{2} (N_{\text{PC}}^2 + N_{\text{I}}^2 - 2C_{\text{q}}^2)$$
 (C.22)

$$\begin{aligned} \textbf{Term 2}: &\langle a_{\mathbf{1}}^{\dagger}a_{\mathbf{1}}\mathsf{h}_{\mathbf{Y}}\mathsf{h}_{\mathbf{Y}}^{\dagger} \rangle = \frac{1}{2} \langle (a_{\mathsf{PC}}^{\dagger} + a_{\mathsf{I}}^{\dagger})(a_{\mathsf{PC}} + a_{\mathsf{I}})\mathsf{h}_{\mathbf{Y}}\mathsf{h}_{\mathbf{Y}}^{\dagger} \rangle \\ &= \frac{1}{2} \langle (a_{\mathsf{PC}}^{\dagger}a_{\mathsf{PC}} + a_{\mathsf{PC}}^{\dagger}a_{\mathsf{I}} + a_{\mathsf{I}}^{\dagger}a_{\mathsf{PC}} + a_{\mathsf{I}}^{\dagger}a_{\mathsf{I}})\mathsf{h}_{\mathbf{Y}}\mathsf{h}_{\mathbf{Y}}^{\dagger} \rangle \\ &= \frac{1}{2} \langle a_{\mathsf{PC}}^{\dagger}a_{\mathsf{PC}}\mathsf{h}_{\mathbf{Y}}\mathsf{h}_{\mathbf{Y}}^{\dagger} + a_{\mathsf{PC}}^{\dagger}a_{\mathsf{I}}\mathsf{h}_{\mathbf{Y}}\mathsf{h}_{\mathbf{Y}}^{\dagger} + a_{\mathsf{I}}^{\dagger}a_{\mathsf{PC}}\mathsf{h}_{\mathbf{Y}}\mathsf{h}_{\mathbf{Y}}^{\dagger} + a_{\mathsf{I}}^{\dagger}a_{\mathsf{I}}\mathsf{h}_{\mathbf{Y}}\mathsf{h}_{\mathbf{Y}}^{\dagger} \rangle \\ &= \frac{1}{2} N_{\mathsf{PC}}(n_{\mathsf{add}}^{\mathsf{Y}} + 1) + C_{\mathsf{q}}(n_{\mathsf{add}}^{\mathsf{Y}} + 1) + C_{\mathsf{q}}(n_{\mathsf{add}}^{\mathsf{Y}} + 1) + N_{\mathsf{I}}(n_{\mathsf{add}}^{\mathsf{Y}} + 1) \\ &= \frac{1}{2} (N_{\mathsf{PC}} + N_{\mathsf{I}} + 2C_{\mathsf{q}})(n_{\mathsf{add}}^{\mathsf{Y}} + 1) \end{aligned}$$

$$\begin{aligned} \textbf{Term 3}: &\langle \mathsf{h}_\mathsf{X} \mathsf{h}_\mathsf{X}^\dagger a_2^\dagger a_2 \rangle = \frac{1}{2} \langle \mathsf{h}_\mathsf{X} \mathsf{h}_\mathsf{X}^\dagger (a_\mathsf{PC}^\dagger - a_\mathsf{I}^\dagger) (a_\mathsf{PC} - a_\mathsf{I}) \rangle \\ &= \frac{1}{2} \langle \mathsf{h}_\mathsf{X} \mathsf{h}_\mathsf{X}^\dagger (a_\mathsf{PC}^\dagger a_\mathsf{PC} - a_\mathsf{PC}^\dagger a_\mathsf{I} - a_\mathsf{I}^\dagger a_\mathsf{PC} + a_\mathsf{I}^\dagger a_\mathsf{I}) \rangle \\ &= \frac{1}{2} \langle \mathsf{h}_\mathsf{X} \mathsf{h}_\mathsf{X}^\dagger a_\mathsf{PC}^\dagger a_\mathsf{PC} - \mathsf{h}_\mathsf{X} \mathsf{h}_\mathsf{X}^\dagger a_\mathsf{PC}^\dagger a_\mathsf{I} - \mathsf{h}_\mathsf{X} \mathsf{h}_\mathsf{X}^\dagger a_\mathsf{I}^\dagger a_\mathsf{PC} + \mathsf{h}_\mathsf{X} \mathsf{h}_\mathsf{X}^\dagger a_\mathsf{I}^\dagger a_\mathsf{I} \rangle \\ &= \frac{1}{2} N_\mathsf{PC} (n_\mathsf{add}^\mathsf{X} + 1) - C_\mathsf{q} (n_\mathsf{add}^\mathsf{X} + 1) - C_\mathsf{q} (n_\mathsf{add}^\mathsf{X} + 1) + N_\mathsf{I} (n_\mathsf{add}^\mathsf{X} + 1) \\ &= \frac{1}{2} (N_\mathsf{PC} + N_\mathsf{I} - 2C_\mathsf{q}) (n_\mathsf{add}^\mathsf{X} + 1) \end{aligned}$$

Term 4:
$$\langle h_X h_X^{\dagger} h_Y h_Y^{\dagger} \rangle = (n_{\text{add}}^X + 1)(n_{\text{add}}^Y + 1)$$
 (C.25)

Finally,

$$\langle N_{\mathsf{X}}^{1} N_{\mathsf{Y}}^{1} \rangle = \frac{\mathsf{G}_{\mathsf{X}} \mathsf{G}_{\mathsf{Y}}}{2} (N_{\mathsf{PC}}^{2} + N_{\mathsf{I}}^{2} - 2C_{\mathsf{q}}^{2}) + \frac{\mathsf{G}_{\mathsf{X}} (\mathsf{G}_{\mathsf{Y}} - 1)}{2} (N_{\mathsf{PC}} + N_{\mathsf{I}} + 2C_{\mathsf{q}}) (n_{\mathsf{add}}^{\mathsf{Y}} + 1)$$

$$+ \frac{\mathsf{G}_{\mathsf{Y}} (\mathsf{G}_{\mathsf{X}} - 1)}{2} (N_{\mathsf{PC}} + N_{\mathsf{I}} - 2C_{\mathsf{q}}) (n_{\mathsf{add}}^{\mathsf{X}} + 1)$$

$$+ (\mathsf{G}_{\mathsf{X}} - 1) (\mathsf{G}_{\mathsf{Y}} - 1) (n_{\mathsf{add}}^{\mathsf{X}} + 1) (n_{\mathsf{add}}^{\mathsf{Y}} + 1)$$

$$(\mathsf{C}.26)$$

$\qquad \langle N_{\mathsf{X}}^{1} \rangle \langle N_{\mathsf{Y}}^{1} \rangle$

$$\langle N_{\mathsf{X}}^{1} \rangle \langle N_{\mathsf{Y}}^{1} \rangle = \langle (\sqrt{\mathsf{G}}_{\mathsf{X}} a_{1}^{\dagger} + \sqrt{\mathsf{G}_{\mathsf{X}} - 1} \mathsf{h}_{\mathsf{X}}) (\sqrt{\mathsf{G}}_{\mathsf{X}} a_{1} + \sqrt{\mathsf{G}_{\mathsf{X}} - 1} \mathsf{h}_{\mathsf{X}}^{\dagger}) \rangle$$

$$\langle (\sqrt{\mathsf{G}}_{\mathsf{Y}} a_{2}^{\dagger} + \sqrt{\mathsf{G}_{\mathsf{Y}} - 1} \mathsf{h}_{\mathsf{Y}}) (\sqrt{\mathsf{G}}_{\mathsf{Y}} a_{2} + \sqrt{\mathsf{G}_{\mathsf{Y}} - 1} \mathsf{h}_{\mathsf{Y}}^{\dagger}) \rangle$$

$$= \langle (\mathsf{G}_{\mathsf{X}} a_{1}^{\dagger} a_{1} + \sqrt{\mathsf{G}_{\mathsf{X}} (\mathsf{G}_{\mathsf{X}} - 1)} \underbrace{(a_{1}^{\dagger} \mathsf{h}_{\mathsf{X}}^{\dagger} + \mathsf{h}_{\mathsf{X}} a_{1})}_{0} + (\mathsf{G}_{\mathsf{X}} - 1) \mathsf{h}_{\mathsf{X}} \mathsf{h}_{\mathsf{X}}^{\dagger}) \rangle$$

$$\langle (\mathsf{G}_{\mathsf{Y}} a_{2}^{\dagger} a_{2} + \sqrt{\mathsf{G}_{\mathsf{Y}} (\mathsf{G}_{\mathsf{Y}} - 1)} \underbrace{(a_{2}^{\dagger} h_{\mathsf{Y}}^{\dagger} + h_{\mathsf{Y}} a_{2})}_{0} + (\mathsf{G}_{\mathsf{Y}} - 1) \mathsf{h}_{\mathsf{Y}} \mathsf{h}_{\mathsf{Y}}^{\dagger}) \rangle$$

$$= \mathsf{G}_{\mathsf{X}} \mathsf{G}_{\mathsf{Y}} \langle a_{1}^{\dagger} a_{1} \rangle \langle a_{2}^{\dagger} a_{2} \rangle + \mathsf{G}_{\mathsf{X}} (\mathsf{G}_{\mathsf{Y}} - 1) \langle a_{1}^{\dagger} a_{1} \rangle \langle \mathsf{h}_{\mathsf{Y}} \mathsf{h}_{\mathsf{Y}}^{\dagger} \rangle$$

$$+ \mathsf{G}_{\mathsf{Y}} (\mathsf{G}_{\mathsf{X}} - 1) \langle \mathsf{h}_{\mathsf{X}} \mathsf{h}_{\mathsf{Y}}^{\dagger} \rangle \langle a_{2}^{\dagger} a_{2} \rangle + (\mathsf{G}_{\mathsf{X}} - 1) (\mathsf{G}_{\mathsf{Y}} - 1) \langle \mathsf{h}_{\mathsf{X}} \mathsf{h}_{\mathsf{Y}}^{\dagger} \rangle \langle \mathsf{h}_{\mathsf{Y}} \mathsf{h}_{\mathsf{Y}}^{\dagger} \rangle$$

with,

$$\langle a_{1}^{\dagger} a_{1} \rangle = \frac{1}{2} \langle (a_{PC}^{\dagger} + a_{I}^{\dagger})(a_{PC} + a_{I}) \rangle$$

$$= \frac{1}{2} \langle a_{PC}^{\dagger} a_{PC} + a_{PC}^{\dagger} a_{I} + a_{I}^{\dagger} a_{PC} + a_{I}^{\dagger} a_{I} \rangle$$

$$= \frac{1}{2} (N_{PC} + 2C_{q} + N_{I})$$
(C.28)

and,

$$\langle a_{2}^{\dagger} a_{2} \rangle = \frac{1}{2} \langle (a_{PC}^{\dagger} - a_{I}^{\dagger}) (a_{PC} - a_{I}) \rangle$$

$$= \frac{1}{2} \langle a_{PC}^{\dagger} a_{PC} - a_{PC}^{\dagger} a_{I} - a_{I}^{\dagger} a_{PC} + a_{I}^{\dagger} a_{I} \rangle$$

$$= \frac{1}{2} (N_{PC} - 2C_{q} + N_{I})$$
(C.29)

Hence,

$$\langle N_{\rm X}^{\rm 1} \rangle \langle N_{\rm Y}^{\rm 1} \rangle = \frac{{\sf G}_{\sf X} {\sf G}_{\sf Y}}{4} ((N_{\sf PC} + N_{\sf I})^2 - 4C_{\sf q}^2) + \frac{{\sf G}_{\sf X} ({\sf G}_{\sf Y} - 1)}{2} (N_{\sf PC} + 2C_{\sf q} + N_{\sf I}) (n_{\sf add}^{\sf Y} + 1) + \frac{{\sf G}_{\sf Y} ({\sf G}_{\sf X} - 1)}{2} (N_{\sf PC} - 2C_{\sf q} + N_{\sf I}) (n_{\sf add}^{\sf X} + 1) + ({\sf G}_{\sf X} - 1) ({\sf G}_{\sf Y} - 1) (n_{\sf add}^{\sf X} + 1) (n_{\sf add}^{\sf Y} + 1)$$
(C.30)

Therefore,

$$\begin{split} \langle N_{\mathsf{X}}^1 N_{\mathsf{Y}}^1 \rangle - \langle N_{\mathsf{X}}^1 \rangle \langle N_{\mathsf{X}}^1 \rangle &= \frac{\mathsf{G}_{\mathsf{X}} \mathsf{G}_{\mathsf{Y}}}{2} (N_{\mathsf{PC}}^2 + N_{\mathsf{I}}^2 - 2C_{\mathsf{q}}^2) + \frac{\mathsf{G}_{\mathsf{X}} (\mathsf{G}_{\mathsf{Y}} - 1)}{2} (N_{\mathsf{PC}} + N_{\mathsf{I}} + 2C_{\mathsf{q}}) (n_{\mathsf{add}}^{\mathsf{Y}} + 1) \\ &+ \frac{\mathsf{G}_{\mathsf{Y}} (\mathsf{G}_{\mathsf{X}} - 1)}{2} (N_{\mathsf{PC}} + N_{\mathsf{I}} - 2C_{\mathsf{q}}) (n_{\mathsf{add}}^{\mathsf{X}} + 1) \\ &+ (\mathsf{G}_{\mathsf{X}} - 1) (\mathsf{G}_{\mathsf{Y}} - 1) (n_{\mathsf{add}}^{\mathsf{X}} + 1) (n_{\mathsf{add}}^{\mathsf{Y}} + 1) \\ &- \frac{\mathsf{G}_{\mathsf{X}} \mathsf{G}_{\mathsf{Y}}}{4} ((N_{\mathsf{PC}} + N_{\mathsf{I}})^2 - 4C_{\mathsf{q}}^2) - \frac{\mathsf{G}_{\mathsf{X}} (\mathsf{G}_{\mathsf{Y}} - 1)}{2} (N_{\mathsf{PC}} - 2C_{\mathsf{q}} + N_{\mathsf{I}}) (n_{\mathsf{add}}^{\mathsf{Y}} + 1) \\ &- \frac{\mathsf{G}_{\mathsf{Y}} (\mathsf{G}_{\mathsf{X}} - 1)}{2} (N_{\mathsf{PC}} - 2C_{\mathsf{q}} + N_{\mathsf{I}}) (n_{\mathsf{add}}^{\mathsf{X}} + 1) \\ &- (\mathsf{G}_{\mathsf{X}} - 1) (\mathsf{G}_{\mathsf{Y}} - 1) (n_{\mathsf{add}}^{\mathsf{X}} + 1) (n_{\mathsf{add}}^{\mathsf{Y}} + 1) \\ &= \frac{\mathsf{G}_{\mathsf{X}} \mathsf{G}_{\mathsf{Y}}}{4} (2N_{\mathsf{PC}}^2 + 2N_{\mathsf{I}}^2 - 4C_{\mathsf{q}}^2 - N_{\mathsf{PC}}^2 - N_{\mathsf{I}}^2 - 2N_{\mathsf{PC}} N_{\mathsf{I}} + 4C_{\mathsf{q}}^2) \\ &= \frac{\mathsf{G}_{\mathsf{X}} \mathsf{G}_{\mathsf{Y}}}{4} (N_{\mathsf{PC}}^2 + N_{\mathsf{I}}^2 - 2N_{\mathsf{PC}} N_{\mathsf{I}}) \\ &= \frac{\mathsf{G}_{\mathsf{X}} \mathsf{G}_{\mathsf{Y}}}{4} (N_{\mathsf{PC}} - N_{\mathsf{I}})^2 \end{split}$$

Finally,

$$Var(N^{1}) = N_{X}^{1}(N_{X}^{1} + 1) + N_{Y}^{1}(N_{Y}^{1} + 1) - \frac{G_{X}G_{Y}}{2}(N_{PC} - N_{I})^{2}$$
 (C.32)

C.2 Quadrature covariance matrix in hypotheses H_1 and H_0

$$a_{1} = \sqrt{\mathsf{t}} a_{\mathsf{PC}} e^{i\phi_{\mathsf{PC}}} + \sqrt{1 - \mathsf{t}} a_{\mathsf{I}}$$

$$a_{2} = \sqrt{1 - \mathsf{t}} a_{\mathsf{PC}} e^{i\phi_{\mathsf{PC}}} - \sqrt{\mathsf{t}} a_{\mathsf{I}}$$

$$\hat{a}_{\mathsf{PC}} = \begin{cases} \sqrt{G}_{\mathsf{PC}} a_{\mathsf{v}} + \sqrt{G}_{\mathsf{PC}} - 1 a_{\mathsf{B}}^{\dagger} & \text{under } H_{0} \\ \sqrt{G}_{\mathsf{PC}} a_{\mathsf{v}} + \sqrt{G}_{\mathsf{PC}} - 1 (\sqrt{\eta} a_{S}^{\dagger} + \sqrt{1 - \eta} a_{\mathsf{B}}^{\dagger}) & \text{under } H_{1} \end{cases}$$
(C.33)

At the two outputs of the Beam-splitter, the recorded quadratures will be:

$$X_{1} = \frac{a_{1} + a_{1}^{\dagger}}{\sqrt{2}}$$

$$= \frac{\sqrt{t}a_{PC}e^{i\phi_{PC}} + \sqrt{1 - t}a_{I} + \sqrt{t}a_{PC}^{\dagger}e^{-i\phi_{PC}} + \sqrt{1 - t}a_{I}^{\dagger}}{\sqrt{2}}$$

$$P_{1} = \frac{-i(a_{1} - a_{1}^{\dagger})}{\sqrt{2}}$$

$$= \frac{-i(\sqrt{t}a_{PC}e^{i\phi_{PC}} + \sqrt{1 - t}a_{I} - \sqrt{t}a_{PC}^{\dagger}e^{-i\phi_{PC}} - \sqrt{1 - t}a_{I}^{\dagger})}{\sqrt{2}}$$

$$X_{2} = \frac{a_{2} + a_{2}^{\dagger}}{\sqrt{2}}$$

$$= \frac{\sqrt{1 - t}a_{PC}e^{i\phi_{PC}} - \sqrt{t}a_{I} + \sqrt{1 - t}a_{PC}^{\dagger}e^{-i\phi_{PC}} - \sqrt{t}a_{I}^{\dagger}}{\sqrt{2}}$$

$$P_{2} = \frac{-i(a_{2} - a_{2}^{\dagger})}{2}$$

$$= \frac{-i(\sqrt{1 - t}a_{PC}e^{i\phi_{PC}} - \sqrt{t}a_{I} - \sqrt{1 - t}a_{PC}^{\dagger}e^{-i\phi_{PC}} + \sqrt{t}a_{I}^{\dagger})}{\sqrt{2}}$$

and the covariance matrix would be:

$$V_{ij} = \frac{1}{2} \langle u_i u_j + u_j u_i \rangle \tag{C.35}$$

with
$$\mathbf{u} = [X_1 P_1 X_2 P_2]^T$$

C.2.1 Hypothesis H1

The correlation term:

$$\langle \hat{a}_{\mathsf{PC}}^{\dagger} a_{\mathsf{I}} \rangle = \langle a_{\mathsf{I}}^{\dagger} a_{\mathsf{PC}} \rangle = \sqrt{\eta (G_{\mathsf{PC}} - 1) N_S (N_S + 1)} = \sqrt{\eta (G_{\mathsf{PC}} - 1)} C_{\mathsf{q}} \tag{C.36}$$

The covariance matrix elements are as follows:

$$\begin{split} V_{11} &= \langle X_1^2 \rangle \\ &= \frac{1}{2} \langle \left(\sqrt{\mathsf{t}} a_{\mathsf{PC}} e^{i\phi_{\mathsf{PC}}} + \sqrt{1 - \mathsf{t}} a_{\mathsf{I}} + \sqrt{\mathsf{t}} a_{\mathsf{PC}}^\dagger e^{-i\phi_{\mathsf{PC}}} + \sqrt{1 - \mathsf{t}} a_{\mathsf{I}}^\dagger \right) \\ &\quad \left(\sqrt{\mathsf{t}} a_{\mathsf{PC}} e^{i\phi_{\mathsf{PC}}} + \sqrt{1 - \mathsf{t}} a_{\mathsf{I}} + \sqrt{\mathsf{t}} a_{\mathsf{PC}}^\dagger e^{-i\phi_{\mathsf{PC}}} + \sqrt{1 - \mathsf{t}} a_{\mathsf{I}}^\dagger \right) \rangle \\ &= \mathsf{t} N_{\mathsf{PC}} + (1 - \mathsf{t}) N_{\mathsf{I}} + 2 \sqrt{\mathsf{t}(1 - \mathsf{t})} \sqrt{\eta (G_{\mathsf{PC}} - 1)} C_{\mathsf{q}} \mathsf{cos} \phi_{\mathsf{PC}} + 1/2 \end{split} \tag{C.37}$$

$$\begin{split} V_{12} &= \frac{1}{2} \langle X_1 P_1 + P_1 X_1 \rangle \\ &= \frac{-i}{4} \langle (\sqrt{t} a_{\text{PC}} e^{i\phi_{\text{PC}}} + \sqrt{1-t} a_{\text{I}} + \sqrt{t} a_{\text{PC}}^{\dagger} e^{-i\phi_{\text{PC}}} + \sqrt{1-t} a_{\text{I}}^{\dagger}) \\ &(\sqrt{t} a_{\text{PC}} e^{i\phi_{\text{PC}}} + \sqrt{1-t} a_{\text{I}} - \sqrt{t} a_{\text{PC}}^{\dagger} e^{-i\phi_{\text{PC}}} - \sqrt{1-t} a_{\text{I}}^{\dagger}) \\ &+ (\sqrt{t} a_{\text{PC}} e^{i\phi_{\text{PC}}} + \sqrt{1-t} a_{\text{I}} - \sqrt{t} a_{\text{PC}}^{\dagger} e^{-i\phi_{\text{PC}}} - \sqrt{1-t} a_{\text{I}}^{\dagger}) \\ &(\sqrt{t} a_{\text{PC}} e^{i\phi_{\text{PC}}} + \sqrt{1-t} a_{\text{I}} + \sqrt{t} a_{\text{PC}}^{\dagger} e^{-i\phi_{\text{PC}}} - \sqrt{1-t} a_{\text{I}}^{\dagger}) \rangle \\ &= \frac{-i}{4} \langle -t a_{\text{PC}} a_{\text{PC}}^{\dagger} - \sqrt{t(1-t)} a_{\text{PC}} a_{\text{I}}^{\dagger} e^{i\phi_{\text{PC}}} - \sqrt{t(1-t)} a_{\text{I}} a_{\text{PC}}^{\dagger} e^{-i\phi_{\text{PC}}} \\ &- (1-t) a_{\text{I}} a_{\text{I}}^{\dagger} + t a_{\text{PC}}^{\dagger} a_{\text{PC}} + \sqrt{t(1-t)} a_{\text{PC}} a_{\text{I}}^{\dagger} e^{i\phi_{\text{PC}}} + \sqrt{t(1-t)} a_{\text{I}}^{\dagger} a_{\text{PC}} e^{i\phi_{\text{PC}}} \\ &+ (1-t) a_{\text{I}}^{\dagger} a_{\text{I}} + t a_{\text{PC}} a_{\text{PC}}^{\dagger} - \sqrt{t(1-t)} a_{\text{PC}} a_{\text{I}}^{\dagger} e^{i\phi_{\text{PC}}} + \sqrt{t(1-t)} a_{\text{I}} a_{\text{PC}}^{\dagger} e^{i\phi_{\text{PC}}} \\ &+ (1-t) a_{\text{I}} a_{\text{I}}^{\dagger} - t a_{\text{PC}}^{\dagger} a_{\text{PC}} - \sqrt{t(1-t)} a_{\text{PC}}^{\dagger} a_{\text{I}} e^{-i\phi_{\text{PC}}} - \sqrt{t(1-t)} a_{\text{I}}^{\dagger} a_{\text{PC}} e^{i\phi_{\text{PC}}} - (1-t) a_{\text{I}}^{\dagger} a_{\text{I}} \rangle \\ &= 0 \end{split}$$

$$V_{13} = \frac{1}{2} \langle X_1 X_2 + X_2 X_1 \rangle$$

$$= \frac{1}{4} \langle (\sqrt{t} a_{PC} e^{i\phi_{PC}} + \sqrt{1 - t} a_{I} + \sqrt{t} a_{PC}^{\dagger} e^{-i\phi_{PC}} + \sqrt{1 - t} a_{I}^{\dagger})$$

$$(\sqrt{1 - t} a_{PC} e^{i\phi_{PC}} - \sqrt{t} a_{I} + \sqrt{1 - t} a_{PC}^{\dagger} e^{-i\phi_{PC}} - \sqrt{t} a_{I}^{\dagger})$$

$$+ (\sqrt{1 - t} a_{PC} e^{i\phi_{PC}} - \sqrt{t} a_{I} + \sqrt{1 - t} a_{PC}^{\dagger} e^{-i\phi_{PC}} - \sqrt{t} a_{I}^{\dagger})$$

$$(\sqrt{t} a_{PC} e^{i\phi_{PC}} + \sqrt{1 - t} a_{I} + \sqrt{t} a_{PC}^{\dagger} e^{-i\phi_{PC}} + \sqrt{1 - t} a_{I}^{\dagger}) \rangle$$

$$= \sqrt{t(1 - t)} (N_{PC} - N_{I}) + (1 - 2t) \sqrt{\eta (G_{PC} - 1)} C_{q} \cos\phi_{PC}$$
(C.39)

$$\begin{split} V_{14} &= \frac{1}{2} \langle X_1 P_2 + P_2 X_1 \rangle \\ &= \frac{-i}{4} \langle (\sqrt{\mathsf{t}} a_{\mathsf{PC}} e^{i\phi_{\mathsf{PC}}} + \sqrt{1 - \mathsf{t}} a_{\mathsf{I}} + \sqrt{\mathsf{t}} a_{\mathsf{PC}}^{\dagger} e^{-i\phi_{\mathsf{PC}}} + \sqrt{1 - \mathsf{t}} a_{\mathsf{I}}^{\dagger}) \\ &\quad (\sqrt{1 - \mathsf{t}} a_{\mathsf{PC}} e^{i\phi_{\mathsf{PC}}} - \sqrt{\mathsf{t}} a_{\mathsf{I}} - \sqrt{1 - \mathsf{t}} a_{\mathsf{PC}}^{\dagger} e^{-i\phi_{\mathsf{PC}}} + \sqrt{\mathsf{t}} a_{\mathsf{I}}^{\dagger}) \\ &\quad + (\sqrt{1 - \mathsf{t}} a_{\mathsf{PC}} e^{i\phi_{\mathsf{PC}}} - \sqrt{\mathsf{t}} a_{\mathsf{I}} - \sqrt{1 - \mathsf{t}} a_{\mathsf{PC}}^{\dagger} e^{-i\phi_{\mathsf{PC}}} + \sqrt{\mathsf{t}} a_{\mathsf{I}}^{\dagger}) \\ &\quad (\sqrt{\mathsf{t}} a_{\mathsf{PC}} e^{i\phi_{\mathsf{PC}}} + \sqrt{1 - \mathsf{t}} a_{\mathsf{I}} + \sqrt{\mathsf{t}} a_{\mathsf{PC}}^{\dagger} e^{-i\phi_{\mathsf{PC}}} + \sqrt{1 - \mathsf{t}} a_{\mathsf{I}}^{\dagger}) \rangle \\ &= C_{\mathsf{q}} \sin \phi_{\mathsf{PC}} \end{split}$$

$$V_{21} = \frac{1}{2} \langle P_1 X_1 + X_1 P_1 \rangle = V_{12} = 0$$
 (C.41)

$$V_{22} = \langle P_{1}^{2} \rangle$$

$$= \langle \frac{1}{2} (-i(\sqrt{t}a_{PC}e^{i\phi_{PC}} + \sqrt{1-t}a_{I} - \sqrt{t}a_{PC}^{\dagger}e^{-i\phi_{PC}} - \sqrt{1-t}a_{I}^{\dagger}))$$

$$(-i(\sqrt{t}a_{PC}e^{i\phi_{PC}} + \sqrt{1-t}a_{I} - \sqrt{t}a_{PC}^{\dagger}e^{-i\phi_{PC}} - \sqrt{1-t}a_{I}^{\dagger}))\rangle$$

$$= -\frac{1}{2} \langle (\sqrt{t}a_{PC}e^{i\phi_{PC}} + \sqrt{1-t}a_{I} - \sqrt{t}a_{PC}^{\dagger}e^{-i\phi_{PC}} - \sqrt{1-t}a_{I}^{\dagger})$$

$$(\sqrt{t}a_{PC}e^{i\phi_{PC}} + \sqrt{1-t}a_{I} - \sqrt{t}a_{PC}^{\dagger}e^{-i\phi_{PC}} - \sqrt{1-t}a_{I}^{\dagger})\rangle$$

$$= tN_{PC} + (1-t)N_{I} + 2\sqrt{t(1-t)}\sqrt{\eta(G_{PC} - 1)}C_{Q}\cos\phi_{PC} + 1/2$$

$$(C.42)$$

$$\begin{split} V_{23} &= \frac{1}{2} \langle P_1 X_2 + X_2 P_1 \rangle \\ &= \frac{1}{4} \langle (-i(\sqrt{\mathsf{t}} a_{\mathsf{PC}} e^{i\phi_{\mathsf{PC}}} + \sqrt{1 - \mathsf{t}} a_{\mathsf{I}} - \sqrt{\mathsf{t}} a_{\mathsf{PC}}^{\dagger} e^{-i\phi_{\mathsf{PC}}} - \sqrt{1 - \mathsf{t}} a_{\mathsf{I}}^{\dagger})) \\ &\quad (\sqrt{1 - \mathsf{t}} a_{\mathsf{PC}} e^{i\phi_{\mathsf{PC}}} - \sqrt{\mathsf{t}} a_{\mathsf{I}} + \sqrt{1 - \mathsf{t}} a_{\mathsf{PC}}^{\dagger} e^{-i\phi_{\mathsf{PC}}} - \sqrt{\mathsf{t}} a_{\mathsf{I}}^{\dagger}) \\ &\quad + (\sqrt{1 - \mathsf{t}} a_{\mathsf{PC}} e^{i\phi_{\mathsf{PC}}} - \sqrt{\mathsf{t}} a_{\mathsf{I}} + \sqrt{1 - \mathsf{t}} a_{\mathsf{PC}}^{\dagger} e^{-i\phi_{\mathsf{PC}}} - \sqrt{\mathsf{t}} a_{\mathsf{I}}^{\dagger}) \\ &\quad + (\sqrt{1 - \mathsf{t}} a_{\mathsf{PC}} e^{i\phi_{\mathsf{PC}}} - \sqrt{\mathsf{t}} a_{\mathsf{I}} + \sqrt{1 - \mathsf{t}} a_{\mathsf{PC}}^{\dagger} e^{-i\phi_{\mathsf{PC}}} - \sqrt{\mathsf{t}} a_{\mathsf{I}}^{\dagger}) \\ &\quad + (\sqrt{1 - \mathsf{t}} a_{\mathsf{PC}} e^{i\phi_{\mathsf{PC}}} - \sqrt{\mathsf{t}} a_{\mathsf{I}} - \sqrt{\mathsf{t}} a_{\mathsf{PC}}^{\dagger} e^{-i\phi_{\mathsf{PC}}} - \sqrt{1 - \mathsf{t}} a_{\mathsf{I}}^{\dagger})) \rangle \\ &\quad = -C_{\mathsf{q}} \sin \phi_{\mathsf{PC}} \end{split}$$

$$V_{24} = \frac{1}{2} \langle P_{1} P_{2} + P_{2} P_{1} \rangle$$

$$= \frac{1}{4} \langle (-i(\sqrt{t}a_{PC}e^{i\phi_{PC}} + \sqrt{1 - t}a_{I} - \sqrt{t}a_{PC}^{\dagger}e^{-i\phi_{PC}} - \sqrt{1 - t}a_{I}^{\dagger}))$$

$$(-i(\sqrt{1 - t}a_{PC}e^{i\phi_{PC}} - \sqrt{t}a_{I} - \sqrt{1 - t}a_{PC}^{\dagger}e^{-i\phi_{PC}} + \sqrt{t}a_{I}^{\dagger}))$$

$$+ (-i(\sqrt{1 - t}a_{PC}e^{i\phi_{PC}} - \sqrt{t}a_{I} - \sqrt{1 - t}a_{PC}^{\dagger}e^{-i\phi_{PC}} + \sqrt{t}a_{I}^{\dagger}))$$

$$(-i(\sqrt{t}a_{PC}e^{i\phi_{PC}} + \sqrt{1 - t}a_{I} - \sqrt{t}a_{PC}^{\dagger}e^{-i\phi_{PC}} - \sqrt{1 - t}a_{I}^{\dagger}))\rangle$$

$$= \sqrt{t(1 - t)}(N_{PC} - N_{I}) + (1 - 2t)\sqrt{\eta(G_{PC} - 1)}C_{q}\cos\phi_{PC}$$
(C.44)

$$V_{31} = \frac{1}{2} \langle X_2 X_1 + X_1 X_2 \rangle = V_{13} \tag{C.45}$$

$$V_{32} = \frac{1}{2} \langle X_2 P_1 + P_1 X_2 \rangle = V_{23} \tag{C.46}$$

$$V_{33} = \langle X_2^2 \rangle$$

$$= \frac{1}{2} \langle (\sqrt{1 - t} a_{PC} e^{i\phi_{PC}} - \sqrt{t} a_{I} + \sqrt{1 - t} a_{PC}^{\dagger} e^{-i\phi_{PC}} - \sqrt{t} a_{I}^{\dagger})$$

$$(\sqrt{1 - t} a_{PC} e^{i\phi_{PC}} - \sqrt{t} a_{I} + \sqrt{1 - t} a_{PC}^{\dagger} e^{-i\phi_{PC}} - \sqrt{t} a_{I}^{\dagger}) \rangle$$

$$= (1 - t) N_{PC} + t N_{I} - 2 \sqrt{t(1 - t)} \sqrt{\eta (G_{PC} - 1)} C_{q} \cos \phi_{PC} + 1/2$$
(C.47)

$$V_{34} = \frac{1}{2} \langle X_2 P_2 + P_2 X_2 \rangle$$

$$= \frac{1}{4} \langle (\sqrt{1 - t} a_{PC} e^{i\phi_{PC}} - \sqrt{t} a_I + \sqrt{1 - t} a_{PC}^{\dagger} e^{-i\phi_{PC}} - \sqrt{t} a_I^{\dagger})$$

$$(-i(\sqrt{1 - t} a_{PC} e^{i\phi_{PC}} - \sqrt{t} a_I - \sqrt{1 - t} a_{PC}^{\dagger} e^{-i\phi_{PC}} + \sqrt{t} a_I^{\dagger}))$$

$$+ (-i(\sqrt{1 - t} a_{PC} e^{i\phi_{PC}} - \sqrt{t} a_I - \sqrt{1 - t} a_{PC}^{\dagger} e^{-i\phi_{PC}} + \sqrt{t} a_I^{\dagger}))$$

$$(\sqrt{1 - t} a_{PC} e^{i\phi_{PC}} - \sqrt{t} a_I + \sqrt{1 - t} a_{PC}^{\dagger} e^{-i\phi_{PC}} - \sqrt{t} a_I^{\dagger}))$$

$$= \frac{-i}{4} \langle (\hat{a}_{PC} e^{i\phi_{PC}} - \hat{a}_I + \hat{a}_{PC}^{\dagger} e^{-i\phi_{PC}} - \hat{a}_I^{\dagger}) (\hat{a}_{PC} e^{i\phi_{PC}} - \hat{a}_I - \hat{a}_{PC}^{\dagger} e^{-i\phi_{PC}} + \hat{a}_I^{\dagger})$$

$$+ (\hat{a}_{PC} e^{i\phi_{PC}} - \hat{a}_I - \hat{a}_{PC}^{\dagger} e^{-i\phi_{PC}} + \hat{a}_I^{\dagger}) (\hat{a}_{PC} e^{i\phi_{PC}} - \hat{a}_I + \hat{a}_{PC}^{\dagger} e^{-i\phi_{PC}} - \hat{a}_I^{\dagger})$$

$$= 0$$

$$(C.48)$$

$$V_{41} = \frac{1}{2} \langle P_2 X_1 + X_1 P_2 \rangle = V_{14}$$
 (C.49)

$$V_{42} = \frac{1}{2} \langle P_2 P_1 + P_1 P_2 \rangle = V_{24}$$
 (C.50)

$$V_{43} = \frac{1}{2} \langle P_2 X_2 + X_2 P_2 \rangle = V_{34} = 0 \tag{C.51}$$

$$V_{44} = \langle P_{2}^{2} \rangle$$

$$= \frac{1}{2} \langle (-i(\sqrt{1 - t}a_{PC}e^{i\phi_{PC}} - \sqrt{t}a_{I} - \sqrt{1 - t}a_{PC}^{\dagger}e^{-i\phi_{PC}} + \sqrt{t}a_{I}^{\dagger}))$$

$$(-i(\sqrt{1 - t}a_{PC}e^{i\phi_{PC}} - \sqrt{t}a_{I} - \sqrt{1 - t}a_{PC}^{\dagger}e^{-i\phi_{PC}} + \sqrt{t}a_{I}^{\dagger}))\rangle$$

$$= (1 - t)N_{PC} + tN_{I} - 2\sqrt{t(1 - t)}\sqrt{\eta(G_{PC} - 1)}C_{q}cos\phi_{PC} + 1/2$$
(C.52)

Hence, the expected covariance matrix would be,

$$V_{\rm BS}^{1} = \begin{bmatrix} t^{N_{\rm PC}+(1-t)N_{\rm I}+1/2} & 0 & \sqrt{{\rm t}(1-{\rm t})}(N_{\rm PC}-N_{\rm I}) & C_{\rm q}{\rm sin}\phi_{\rm PC} \\ 0 & t^{N_{\rm PC}+(1-{\rm t})N_{\rm I}+1/2} & -C_{\rm q}{\rm sin}\phi_{\rm PC} & \sqrt{{\rm t}(1-{\rm t})}(N_{\rm PC}-N_{\rm I}) \\ +2C_{\rm q}'{\rm cos}\phi_{\rm PC} & -C_{\rm q}{\rm sin}\phi_{\rm PC} & \sqrt{{\rm t}(1-{\rm t})}(N_{\rm PC}-N_{\rm I}) \\ +2C_{\rm q}'{\rm cos}\phi_{\rm PC} & -C_{\rm q}{\rm sin}\phi_{\rm PC} & \sqrt{{\rm t}(1-{\rm t})}(N_{\rm PC}-N_{\rm I}) \\ +(1-2{\rm t})C_{\rm q}^{"}{\rm cos}\phi_{\rm PC} & -C_{\rm q}{\rm sin}\phi_{\rm PC} & 0 \\ C_{\rm q}{\rm sin}\phi_{\rm PC} & \sqrt{{\rm t}(1-{\rm t})}(N_{\rm PC}-N_{\rm I}) \\ +(1-2{\rm t})C_{\rm q}^{"}{\rm cos}\phi_{\rm PC} & 0 & (1-{\rm t})N_{\rm PC}+{\rm t}N_{\rm I}+1/2 \\ -2C_{\rm q}'{\rm cos}\phi_{\rm PC} & 0 & -2C_{\rm q}'{\rm cos}\phi_{\rm PC} \end{bmatrix} \\ {\rm with} \ C_{\rm q}' = \sqrt{{\rm t}(1-{\rm t})\eta(G_{\rm PC}-1)}C_{\rm q} \ {\rm and} \ C_{\rm q}'' = \sqrt{\eta(G_{\rm PC}-1)}C_{\rm q} \\ \end{array} \right.$$

C.2.2 Hypothesis H0

at H_0 hypothesis, the phase-conjugated signal is purely background noise and there is no correlation, $C_{\mathbf{q}}=0$.

Hence, the expected covariance matrix would be,

$$V_{\text{BS}}^{0} = \begin{bmatrix} tN_{\text{B}} + (1-t)N_{\text{I}} + 1/2 & 0 & \sqrt{t(1-t)}(N_{\text{B}} - N_{\text{I}}) & 0 \\ 0 & tN_{\text{B}} + (1-t)N_{\text{I}} + 1/2 & 0 & \sqrt{t(1-t)}(N_{\text{B}} - N_{\text{I}}) \\ \sqrt{t(1-t)}(N_{\text{B}} - N_{\text{I}}) & 0 & (1-t)N_{\text{B}} + tN_{\text{I}} + 1/2 & 0 \\ 0 & \sqrt{t(1-t)}(N_{\text{B}} - N_{\text{I}}) & 0 & (1-t)N_{\text{B}} + tN_{\text{I}} + 1/2 \end{bmatrix}$$
(C.54)